

USE OF OXYGEN ISOTOPIC EXCHANGE TO EXPLORE CATALYTIC ACTIVITY AND
THE MECHANISM OF OXYGEN REDUCTION ON OXIDES

By

CYNTHIA C. KAN

A DISSERTATION PRESENTED TO THE GRADUATE SCHOOL
OF THE UNIVERSITY OF FLORIDA IN PARTIAL FULFILLMENT
OF THE REQUIREMENTS FOR THE DEGREE OF
DOCTOR OF PHILOSOPHY

UNIVERSITY OF FLORIDA

2009

© 2009 Cynthia C. Kan

To Heywood

ACKNOWLEDGMENTS

First, I thank my parents for their guidance and for raising me in an environment which nurtured my ambitions. My family has been a great source of happiness for me and I am very lucky to have such loving relatives. My second acknowledgement goes to Heywood for helping me adapt to graduate school and form a strong work ethic. He went to great lengths to ensure my happiness and seeing him was the best part of the day. During days when I just wanted to defenestrate my entire project, I am grateful for my friends, especially Ken and Christine, who were willing to listen to me rant. Without my strong support system, I would not have the confidence nor drive to pursue great challenges (like getting a PhD).

Being surrounded by people who were intellectually curious and motivated was an inspiration to me. I owe a great deal of gratitude to the wonderful staff of the Particle Science and Engineering Center and the Major Analytical Instrumentation Center for their patience and for teaching me how to use various instruments. I also thank my group members, for providing thoughtful discussion, assistance, their friendship and hours of entertainment! It was a joy working with them all. In particular, I want to acknowledge Bryan, Eric and Martin for their considerable contribution to my laboratory knowledge. Another member who made my life much easier during the past four years is Jennifer Tucker, who has done a tremendous job helping our group secure resources. I also thank Dr. Wachsman for providing this opportunity for me to learn and contribute to the collective knowledge of mankind.

TABLE OF CONTENTS

	<u>page</u>
ACKNOWLEDGMENTS	4
LIST OF TABLES	7
LIST OF FIGURES	8
CHAPTER	
1 INTRODUCTION	13
2 BACKGROUND	18
2.1 Solid Oxide Fuel Cell Overview	18
2.2 The Cathode Reaction	19
2.3 Perovskite structured cathode materials	20
2.3.1 Lanthanum Strontium Manganite	21
2.3.2 Lanthanum Strontium Cobalt Ferrite	22
2.4 Oxygen transport parameters D and k	24
2.5 Gas phase isotopic oxygen exchange	25
2.6 Proposed Mechanism of Oxygen Exchange	29
3 TEMPERATURE PROGRAMMED EVALUATION OF CATALYTIC PROPERTIES	32
3.1 Introduction	32
3.2 Experimental	33
3.2.1 Powder Materials	33
3.2.2 Catalysis System	33
3.2.3 Temperature Programmed Reaction, Desorption and Exchange	35
3.3 Results and Discussion	35
3.3.1 Oxygen Non-Stoichiometry from TPR	35
3.3.2 Temperature Programmed Isotopic Exchange	37
3.3.3 Temperature Programmed Desorption after Isotopic Exchange	38
3.4 Conclusion	39
4 ISOTHERMAL ISOTOPIC SWITCHING	41
4.1 Introduction	41
4.2 Theory	42
4.3 Experimental	45
4.3.1 Isothermal Isotopic Switching	45
4.4 Results and Discussion	47
4.4.1 $(La_{0.8}Sr_{0.2})_{0.98}MnO_{3\pm\delta}$	47
4.4.2 $La_{0.6}Sr_{0.4}Co_{0.2}Fe_{0.8}O_{3-\delta}$	53
4.4.3 Trends in LSM and LSCF	56
4.4.3.1 Degradation of LSCF	63

4.4.4	Gas Phase Behavior Simulation	64
4.5	Conclusion	74
5	IDENTIFYING TRENDS IN CATALYTIC ACTIVITY WITH SYSTEMATIC SURFACE MODIFICATION	77
5.1	Introduction	77
5.2	Experimental	78
5.2.1	Materials	78
5.2.2	Powder Characterization	78
5.2.3	Catalysis System Configuration	79
5.2.4	Temperature Programmed Isotopic Exchange	79
5.3	Results and Discussion	80
4.3.1	X-Ray Photoelectron Spectroscopy	82
4.3.2	Temperature Programmed Isotopic Exchange	87
4.4	Conclusion	99
6	CONCLUSION	101
APPENDIX		
A	DERIVATION OF MODEL	104
B	PARAMETER FITTING SCRIPT	106
LIST OF REFERENCES		108
BIOGRAPHICAL SKETCH		115

LIST OF TABLES

<u>Table</u>		<u>page</u>
3-1	Temperature programmed conditions	35
4-1	Exchange parameters obtained from simulation for LSM at 700 °C	68
4-2	Exchange parameters obtained from simulation for LSM at 2% O ₂	69
4-3	Exchange parameters for LSCF at 700 °C, at various pO ₂	72
4-4	Exchange parameters for LSCF at 1% O ₂ 40 sccm at 400-500 °C	72
4-5	Exchange parameters for varying sample sizes of LSCF	72
5-1	Specific surface areas of infiltrated powders	80

LIST OF FIGURES

<u>Figure</u>	<u>page</u>
1-1 Cell voltage and polarization losses (ΔU) as a function of operating temperature.....	14
2-1 Schematic of the triple phase boundary	19
2-2 Oxygen reduction pathways for pure electronic, composite (electronic + ionic conducting phases) and mixed ionic electronic conducting cathodes	20
2-3 Unit cell of cubic perovskite structure	21
2-4 Oxygen exchange showing possible species formed	28
2-5 Schematic showing reactor feed and products.....	30
3-1 Catalytic testing system comprised of two separate feed streams, a microreactor within a furnace and quadrupole mass spectromete	33
3-2 Quartz micro-reactor schematic	34
3-3 $\text{La}_{0.6}\text{Sr}_{0.4}\text{Co}_{0.2}\text{Fe}_{0.8}\text{O}_{3-\delta}$ Oxygen non-stoichiometry ($3-\delta$) vs. temperature	36
3-4 Temperature programmed exchange profile for A) LSM and B) LSCF	37
3-5 Temperature programmed desorption after TPX for A) LSM B) LSCF	39
4-1 Oxygen isotopic switch profile through a room temperature reactor	46
4-2 $(\text{La}_{0.8}\text{Sr}_{0.2})_{0.98}\text{MnO}_{3\pm\delta}$ isothermal isotopic exchange under 1% O_2	48
4-3 Argon Tracer Step-Profile.....	49
4-4 Initial rates of exchange vs. oxygen partial pressure for LSM at 600 and 800°C.....	51
4-5 Arrhenius-like plot showing activation energy of oxygen exchange on LSM	52
4-6 Isothermal exchange of LSCF at 650°C and 10,000 ppm O_2	53
4-7 Initial rates of exchange vs. oxygen partial pressure for LSCF at 600°C	54
4-8 Arrhenius plot showing activation energy of oxygen exchange on LSCF	55
4-9 Isothermal isotopic switch profile at 800 °C for A) LSM and B) LSCF	56
4-10 Integration of amount of ^{16}O from the gas stream	57
4-11 Fraction of oxygen in solid converted from ^{16}O to ^{18}O vs. time.....	58

4-12	Reaction rate versus square root of free stream velocity divided by pellet size	59
4-13	Conversion of LSCF in 1% O ₂	60
4-14	Switching profiles for LSCF A) 300 °C B) 400 °C and C) 500 °C	63
4-15	Conversion of LSCF vs. time at 500 °C as a function of sample size	63
4-16	Exchange with fresh LSCF and LSCF after many cycles.....	64
4-17	Numerical solution for A) Dissociative adsorption limited case B) Incorporation limited case	65
4-18	Value of parameters A and B as a function of iteration number for LSM.....	66
4-19	Profile of ¹⁶ f _{ads} and ¹⁶ f _{bulk} obtained from LSM with model superimposed	67
4-20	Normalized ¹⁶ O ₂ , ¹⁸ O ₂ and ¹⁶ O ¹⁸ O signals and predicted profile for LSM.....	68
4-21	Value of parameters A and C as a function of iteration number for LSCF	70
4-22	Profile of ¹⁶ f _{ads} and ¹⁶ f _{bulk} obtained from LSCF with model superimposed.....	70
4-23	Normalized ¹⁶ O ₂ , ¹⁸ O ₂ and ¹⁶ O ¹⁸ O data and predicted profile for LSCF	71
4-24	Normalized data and predicted profile for LSCF, calculated by fitting the ¹⁸ f _{ads} data instead of the ¹⁶ f _{ads} data.....	71
5-1	Powder morphology captured with SEM, taken at 20,000x	81
5-2	Diffraction patterns of LSM, LSM + 20 wt% Co, Co ₃ O ₄	81
5-3	Survey spectra (XPS) for LSM and LSCF taken at 45° angle.....	82
5-4	(La _{0.8} Sr _{0.2}) _{0.98} MnO _{3±δ} O1s peaks A) before heating B) after heating	83
5-5	O1s spectra for LSM infiltrated with 5 wt% A) La, Sr B) Fe, Co	83
5-6	O1s spectra for LSCF and LSCF + 5 wt% Mn	84
5-7	La 3d _{5/2} peaks for LSM and LSM + 5 wt% La	85
5-8	Sr 3d peaks for LSM and LSM + 5 wt% Sr.....	85
5-9	Co 2p _{3/2} profile of LSM + 5wt% Co and LSCF.....	86
5-10	Fe 2p _{3/2} profile of LSM + 5wt% Fe and LSCF.....	87
5-11	Temperature programmed exchange profile of infiltrated samples.....	89

5-12	Temperature programmed exchange profile of LSM + 5 wt% Co plotted with statistical equilibrium model.....	91
5-13	Net oxygen desorption from temperature programmed reaction (TPR) profile for LSM and LSCF.....	92
5-14	Temperature programmed exchange profile for LSCF + 5 wt% Mn.....	95
5-15	Temperature programmed exchange profile for 40 mg Co ₃ O ₄	96
5-16	Conversion (1-normalized ¹⁸ O ₂) vs. temperature.....	98
5-17	Formation of ¹⁶ O ¹⁸ O (normalized by total oxygen) as a function of temperature.....	99

Abstract of Dissertation Presented to the Graduate School
of the University of Florida in Partial Fulfillment of the
Requirements for the Degree of Doctor of Philosophy

USE OF OXYGEN ISOTOPIC EXCHANGE TO EXPLORE CATALYTIC ACTIVITY AND
THE MECHANISM OF OXYGEN REDUCTION ON OXIDES

By

Cynthia Kan

May 2009

Chair: Eric D. Wachsman

Major: Materials Science and Engineering

The electrochemical performance of intermediate temperature solid oxide fuel cells is limited by high polarization losses incurred from the oxygen reduction reaction at the cathode. The mechanism of oxygen reduction as well as the key characteristics responsible for high oxygen reactivity are currently not well understood and represent a hurdle in the targeted development of electro-catalytically active cathode materials. These properties were studied using heterogeneous catalysis techniques coupled with labeled oxygen. The primary materials studied were $(\text{La}_{0.8}\text{Sr}_{0.2})_{0.98}\text{MnO}_{3\pm\delta}$ (LSM) and $\text{La}_{0.6}\text{Sr}_{0.4}\text{Co}_{0.2}\text{Fe}_{0.8}\text{O}_{3-\delta}$ (LSCF).

Temperature programmed isotopic exchange indicated that LSM was less active for surface exchange than LSCF, in agreement with previous results from the literature. This confirms the validity of isotopic exchange as a means to gauge the activity for oxygen reduction. Samples of LSM and LSCF were infiltrated with metal oxides to modify the surface properties and tested with this technique to identify trends in catalytic activity. Of the samples examined, LSCF was the most active. Addition of cobalt to LSM improved the activity while iron infiltration was detrimental. According to XPS, the iron on the surface of LSCF and LSM were of different oxidation states, which could explain why it caused a negative effect in LSM. These

results indicate that optimization of catalytic activity is possible through surface modification; however, it is not only the surface composition, but also the electronic properties of the surface which determine activity.

A two-step mechanism consisting of dissociative adsorption of molecular oxygen followed by incorporation into the lattice was proposed and used to model the behavior obtained from isothermal isotopic switching. Effective rate constants for each step were obtained by fitting the model to the gas phase isotopologue distribution. These parameter values indicate which step is rate-limiting. LSCF was shown to be limited by dissociative adsorption. The reaction for LSM was slower than predicted by the model, suggesting that the diffusion of oxygen from the particle core to the surface is the actual rate limiting step. Based off these results, LSCF would be a good candidate for surface modification to improve dissociative adsorption and LSM could be improved by increasing the oxygen diffusivity.

CHAPTER 1 INTRODUCTION

The relatively high standard of living enjoyed in industrialized countries today is afforded by the immense consumption of energy and resources [1]. With developing countries eager to catch up and benefit from the amenities of a first world lifestyle, their energy needs will increase and put an additional strain on the limited supply of fossil fuels. The growing demand for energy must continue to be met or else depressed economic growth and societal instability will ensue [1]. This presents a great technological challenge as fossil fuels such as coal, petroleum and natural gas provided over 80% of the world's energy in 2004 [2]. This heavy dependence on non-renewable energy sources cannot be sustained indefinitely. Therefore, a comprehensive portfolio of renewable energy solutions must be developed to meet present and future energy needs.

Some of the energy technologies in development today are solar cells, wind turbines, and biofuels. These sources are great for electricity production but are not convenient for energy storage, with the exception of biofuels. One issue concerning biofuels is that they are subject to many of the same problems facing other carbon based fuels. Harnessing energy through combustion, while economical, is inefficient and a major contributor to environmental pollution. Incomplete hydrocarbon combustion produces harmful compounds such as soot, carbon monoxide, and nitrogen oxides. A cleaner and more efficient method of releasing the energy stored in chemical fuel is through electrochemical conversion by fuel cells. As long as a continuous supply of air and fuel are introduced into the fuel cell, electricity is produced.

In particular, the solid oxide fuel cell (SOFC) is especially attractive due to its high energy efficiency and fuel flexibility. The worldwide average efficiency for electricity produced from combustion of fossil fuels is a mere 36% [3] whereas SOFCs can reach 60% stand-alone

efficiency and up to 85% in a combined heat and power system [4]. All fuel cells are able to run off of hydrogen, but SOFCs operate at high temperature (1000 °C), which allows various hydrocarbon fuels to be reformed internally. Given the remarkable benefits of this technology, developers are excited about commercializing SOFCs for widespread use. However, there are currently several significant barriers to bringing SOFCs to market.

One consequence of operating at such high temperatures is that it requires the use of expensive and specialized materials in the cell and in the balance of plant [5]. Decreasing the operating temperature to the intermediate range of 600-800 °C would allow more economic materials, such as stainless steel, to be used for interconnects and would decrease insulation requirements. It would also reduce the start-up time as well as degradation rates. All these benefits, however, come at the cost of performance [6,7]. It is shown in Figure 1-1 that as the

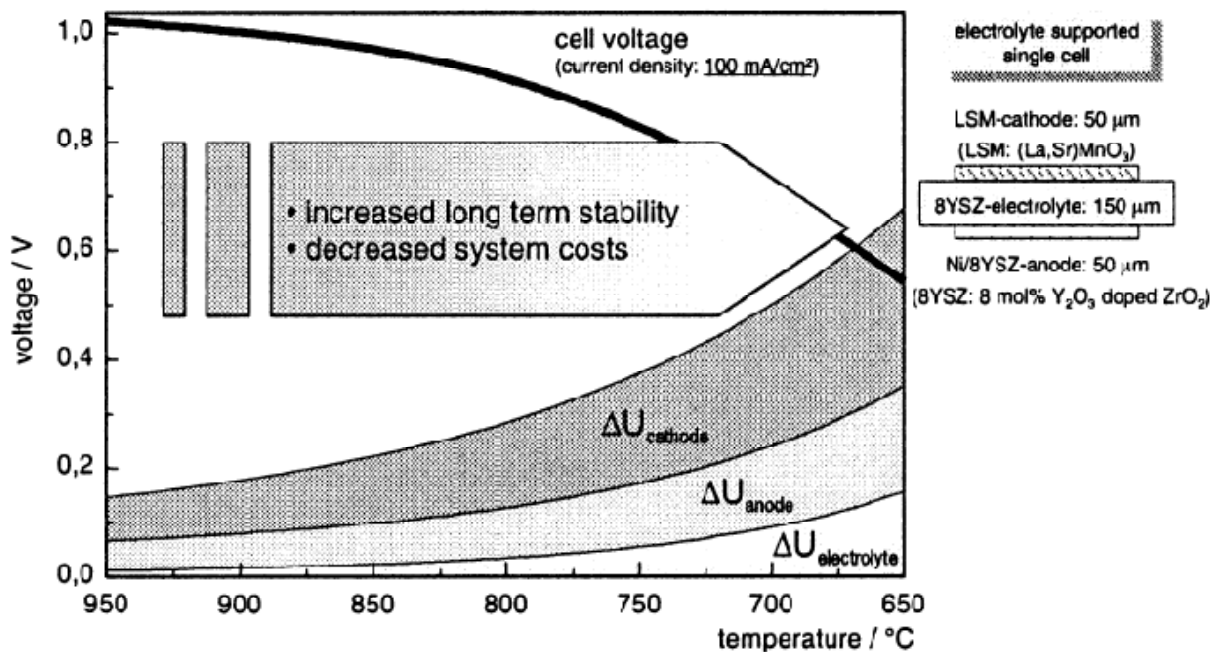


Figure 1-1. Cell voltage and polarization losses (ΔU) at constant current density of 100mA/cm² as a function of operating temperature [6]. Reprinted from Journal of the European Ceramic Society 21, E. Ivers-Tiffée, A. Weber, D. Herbrist, Materials and technologies for SOFC-components, 1805-1811, Copyright (2001), with permission from Elsevier

temperature decreases, losses from the cathode become the largest component. In order to preserve adequate performance while extending the operating temperature into the intermediate range, the kinetics of the heterogeneous electrode reaction must be improved by designing better catalysts. Before targeted development can occur, however, a fundamental understanding of the oxygen reduction processes occurring on the cathode surface must be obtained.

Currently, the mechanism and rate laws governing surface reactions on cathode materials are not well established [8-11]. Advancements in the state of knowledge of oxygen surface exchange have been made using methods such as conductivity-relaxation [12-16], temperature programmed reaction [17-20], isotopic exchange depth profiling [21,22], and impedance spectroscopy [8,23,24]. However, it is difficult to get mechanistic information from these approaches. Heterogeneous catalysis techniques such as temperature programmed and steady state isothermal isotopic exchange hold much promise in shedding light on the cathode reaction kinetics, and are explored in depth in this dissertation. The use of isotopically labeled oxygen gas is critical due to the large normal oxygen background in the oxide materials examined.

Interpretation of results throughout this dissertation is through the framework introduced in Chapter 2, where a two-step mechanism of dissociative adsorption followed by incorporation is proposed. The gas phase molecular oxygen isotopologue distribution is determined statistically by the isotopic composition of surface oxygen adatoms. This key concept is used in Chapters 4 and 5 to demonstrate the validity of the model.

The organization of the dissertation is as follows. Chapter 2 is a literature overview of the cathode reaction, material properties and theory of oxygen transport and surface exchange. The purpose of Chapter 3 is to introduce the experimental system and show that the results obtained from our experimental system are comparable with those from the literature. Additionally, the

temperature programmed isotopic exchange behavior of the two main cathode materials is discussed in detail and serves as a reference point for analysis in later chapters. The use of isothermal isotopic exchange, where the feed stream oxygen isotopic labeling is switched abruptly, and the ensuing analysis is presented in Chapter 4. This method is used to identify trends in the time dependent behavior of the different cathode materials. An extensive section on extracting the effective rate constants from parameter fitting is included at the end. These rate constants, coupled with the observed behavior, are used to determine the rate limiting step of oxygen exchange. Chapter 5 covers trends in catalytic activity from isotopic exchange of cathode materials infiltrated with various metal oxides.

Before this work, the surface exchange reaction was characterized mainly through mass transport coefficients [25] which were not mechanistic in nature. The application of isotopic exchange to determine oxide reactivity was interpreted, as recently as 2005 [26], using the same one-step “mechanisms” used in the 1960’s [27] which took into account the exchange of zero, one or two atoms between the gas and solid phases. These reactions do not constitute a mechanism and therefore cannot be used to determine the rate limiting process. Instead of merely applying the technique of isotopic exchange to cathode materials, and then using the deeply rooted and stale analysis from the literature, the better approach was to start from scratch and develop my own framework for interpreting results from isothermal isotopic exchange. As a result, the following contributions have been made:

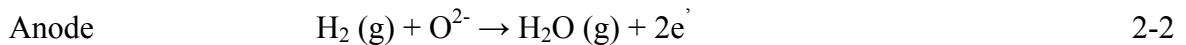
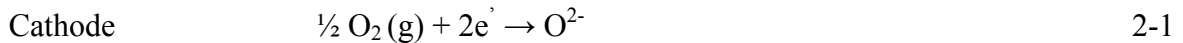
- Developed a comprehensive framework for oxygen isotopic exchange analysis based off of a two-step mechanism of dissociative adsorption followed by incorporation

- Modeled the gas phase and sample surface/bulk oxygen compositions as a function of time for two SOFC cathode materials
- Created a custom program to extract mechanistic rate constants from parameter fitting isothermal isotopic exchange profiles.
- Determined that the catalytic activity of an oxide material can be affected through surface modification without altering the apparent mechanism of oxygen exchange

CHAPTER 2
BACKGROUND

2.1 Solid Oxide Fuel Cell Overview

A fuel cell is an electrochemical device which transforms chemical energy stored in gasified fuel into electricity through a redox reaction. Like batteries, fuel cells have three main components: the anode, electrolyte and cathode. Interconnects are used to join the devices in series to produce the required electrical output. The electrolyte, which is the component used to classify the various types of fuel cells, ideally has zero electronic conductivity, which forces the electrons liberated by the electrode reactions into the external circuit to perform useful work. For solid oxide fuel cells (SOFCs), a thin dense layer of oxygen ion conducting ceramic, such as doped ZrO_2 or CeO_2 , functions as the electrolyte. Sandwiching the electrolyte on either side are the electrodes where the half cell reactions occur. On the cathode, oxygen is reduced to O^{2-} and incorporated into the electrolyte (Eqn. 2-1). After passing through the electrolyte, the oxygen ion combines with hydrogen on the anode side to form water and electrons (Eqn. 2-2).



As long as fuel and oxidant are supplied, the reaction will continue to produce power.

Characteristics of a good electrode are (1) high electrical conductivity (2) long term stability (3) fast gas transport and (4) high catalytic activity for redox reactions. The state-of-the-art anode material is currently accepted to be nickel/yttria-stabilized zirconia (YSZ) cermet for its affordability, good electro-mechanical properties and catalytic activity [28]. In the case of the cathode, however, there is no material which adequately satisfies all the above criteria in the intermediate temperature range.

2.2 The Cathode Reaction

The cathode half cell reaction, written in Kröger-Vink notation, appears to be quite simple:



However, this reaction actually encompasses a series of several elementary processes ranging from diffusion to dissociative adsorption and charge transfer, finally resulting in incorporation into the solid [11,25,29-32]. For multi-step chemical reactions, it is common for one elementary reaction to be significantly slower than the others. It is this step which determines the overall rate of the reaction and is known as the rate determining step [30,33]. Once it is understood what step is limiting the overall reaction, catalysts can then be engineered with the proper functionality.

The reduction reaction pathway is expected to vary depending on the cathode material. For a purely electronically conducting cathode, such as platinum, the oxygen reduction reaction is thought to be restricted to the triple phase boundary (TPB) where the electronically conducting, oxygen ion conducting and gas phases converge (Figure 2-1). This is because the reactants

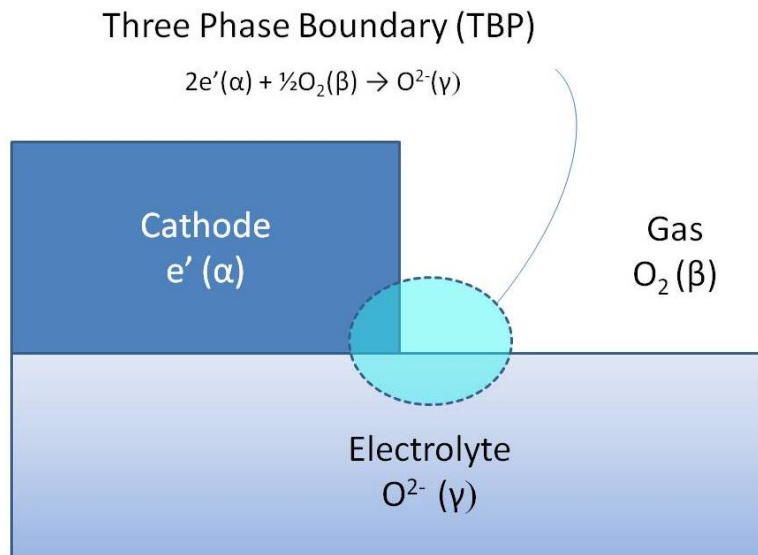


Figure 2-1. Schematic of the triple phase boundary showing the electronically conducting phase (α), gas phase (β), and ionically conducting phase (γ) and their roles in oxygen reduction

(electrons, vacancies and oxygen) are unique to a particular component, and can only participate in oxygen reduction when all three are available. To increase the reaction area from a 2D line to a 3D surface, researchers turned to mixed ionic/electronic conductors (MIECs) so that oxygen could be exchanged throughout the entire cathode/electrolyte interface (Figure 2-2). Because of this difference in pathway between the electronic and mixed conductors, it is expected that the mechanism of oxygen exchange will also be different. Thus, one material of each type has been chosen for examination using isotopic exchange.

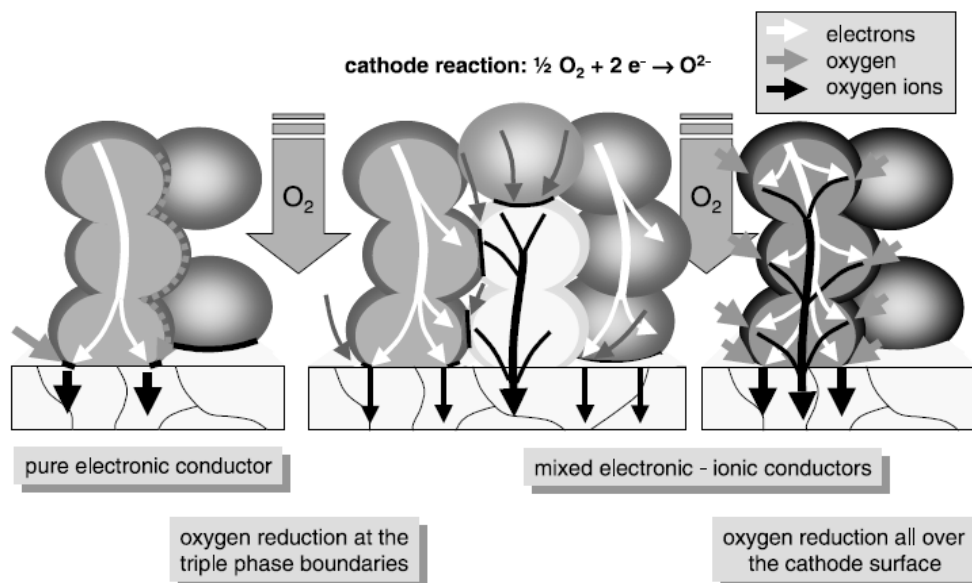


Figure 2-2. Oxygen reduction pathways for pure electronic, composite (electronic + ionic conducting phases) and mixed ionic electronic conducting cathodes [34] Reprinted from Journal of Power Sources 127, A. Weber, E. Ivers-Tiffée, Materials and concepts for solid oxide fuel cells (SOFCs) in stationary and mobile applications, 273–283, Copyright (2004), with permission from Elsevier

2.3 Perovskite structured cathode materials

As mentioned previously, cathode materials must fulfill numerous requirements [35], not the least of which is affordability. Inexpensive replacements for porous platinum cathodes used in the past are oxides which crystallize in the ABO_3 perovskite structure (Figure 2-3). This material system, commonly with a rare earth metal in the A site and a transition metal in the B site, is

very accommodating and allows for the introduction of various defects through doping on the A or B site. Through controlled defect engineering, various properties, such as electronic conductivity or thermal expansion, can be optimized. The specific materials chosen for study in this work are perovskites which have shown good performance and are well studied [10,14,36-39]. Both are available commercially.

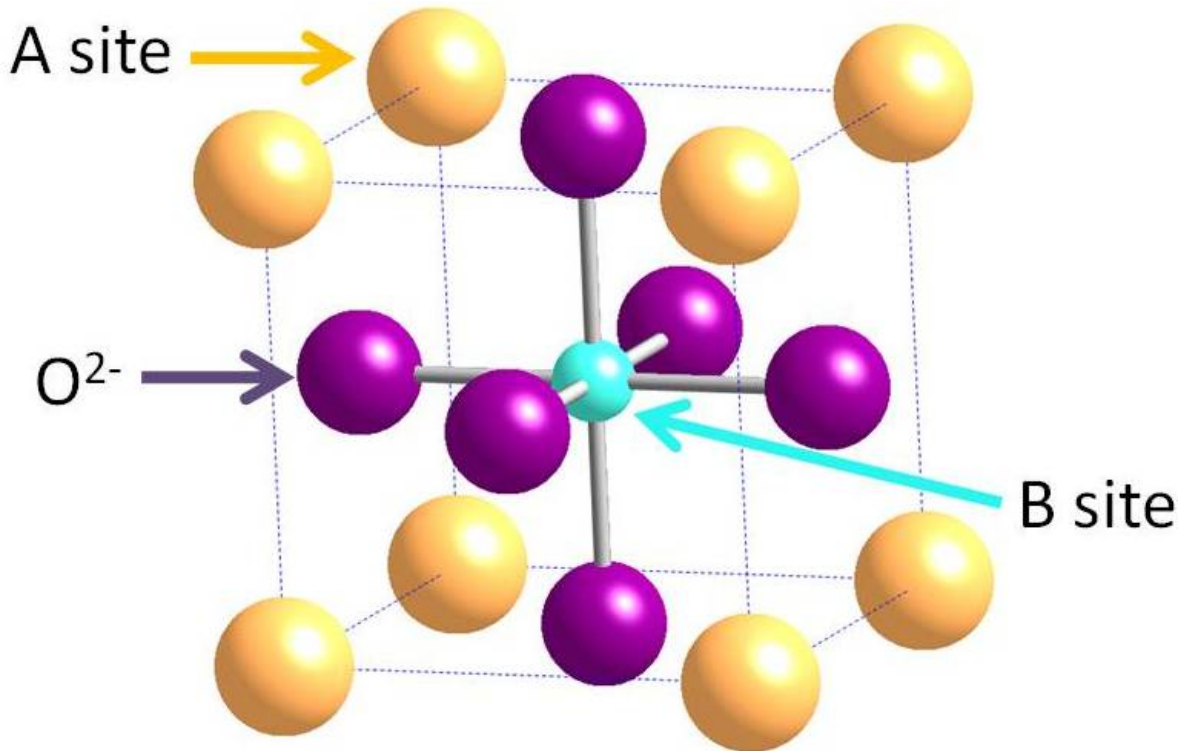


Figure 2-3. Unit cell of cubic perovskite structure

2.3.1 Lanthanum Strontium Manganite

Strontium doped lanthanum manganite (LSM) is the most studied and prevalent SOFC cathode material [22,29,30,32,37,40] due to its long term stability and the fact that its thermal expansion coefficient is very similar to that of the electrolyte material YSZ. Although LSM performs well at high temperatures, cathodic polarization becomes significant at intermediate temperatures, limiting its usefulness as an intermediate temperature SOFC cathode material.

Therefore, it is of great interest to understand the oxygen reduction process on LSM so that the catalytic activity may be improved.

The undoped base material, lanthanum manganite, is p-type with a conductivity of approximately 75 S/cm at 1000 °C [41]. Strontium substitution of the A site lanthanum enhances the electrical conductivity and reaches a maximum at around 15-20% (150 S/cm [41,42]). The addition of a divalent ion results in the Sr²⁺ on a La³⁺ site being charge compensated through the formation of Mn⁴⁺ (Eqn. 2-5). This enhances the small polaron conduction mechanism where charges hop between Mn³⁺ and an adjacent Mn⁴⁺ [42,43].



In addition to the electrical conductivity, the oxygen non-stoichiometry is also of interest. Defects, such as oxygen vacancies, in ionic solids are in equilibrium with the external environment at sufficiently high temperatures and doped lanthanum manganite is no exception. This work focuses on the specific composition (La_{0.8}Sr_{0.2})_{0.98}MnO_{3±δ} (LSM), and as the ±δ indicates, the material can be super- and sub-stoichiometric [38,42]. At 1000 °C, the material does not begin to become sub-stoichiometric through loss of oxygen until the oxygen partial pressure (pO₂) drops below 10⁻¹⁰ atm. The lack of oxygen vacancies translates to a low ionic conductivity for LSM, with values between 10⁻⁷ and 10⁻⁶ S/cm being calculated from diffusivity data at 900-1000 °C [37,44]. Given that the difference between the electronic and ionic conductivity is over 8 orders of magnitude, it is appropriate to classify LSM as a purely electronic conductor.

2.3.2 Lanthanum Strontium Cobalt Ferrite

More recently, interest in developing MIEC cathodes has directed research efforts toward the La_{1-x}Sr_xCo_{1-y}Fe_yO_{3-δ} system [45,46]. These materials are double substituted perovskites with elements of similar ionic radii occupying the same site (La and Sr on A site, Co and Fe on B site)

[30]. The substitution of Sr^{2+} on the La^{3+} sublattice requires that electroneutrality (Eqn. 2-6) be maintained by either oxidizing the B site element from +3 to +4 or through formation of oxygen vacancies [47].



At low temperatures, significant electronic compensation occurs, thought to be from preferential formation of Fe^{4+} [39]. At high temperature, unlike its effect in LSM, strontium substitution on the lanthanum site results in ionic compensation via formation of oxygen vacancies [47]. This leads to a reduction in the concentration of B_B^\cdot .



This explains the material's decrease in electronic conductivity and increase in ionic conductivity at high temperatures corresponding to reaction 2-7. In addition, the electrical conductivity is also affected by the B site element. For a given A site composition, the electrical conductivity can be increased by simply increasing the B site cobalt content [47,48]. However, the addition of cobalt also has the unintended effect of increasing the thermal expansion coefficient (TEC); therefore a careful balance between conductivity and TEC matching with the electrolyte must be achieved. The addition of iron to the B site decreases electronic conductivity but also restricts thermal expansion. Due to insulating zirconate phase formation at the interface [49], cobalt containing cathodes are not compatible with YSZ, and must be interfaced with ceria based electrolytes for which there are no known reactions [46,48].

It is generally accepted that the composition $\text{La}_{0.6}\text{Sr}_{0.4}\text{Co}_{0.2}\text{Fe}_{0.8}\text{O}_{3-\delta}$ (LSCF) is well optimized and mechanically compatible ($17.5 \times 10^{-6} \text{ K}^{-1} \text{ TEC}$ [50,51]) with gadolinium doped ceria (GDC), which has a TEC around $12.5 \times 10^{-6} \text{ K}^{-1}$ [51]. At 900 °C, LSCF has an ionic conductivity of 0.23 S/cm and an electronic conductivity of 252 S/cm [47]; the corresponding

ionic transport number is 9×10^{-4} , which indicates the majority of the conductivity is electronic. Compared to the ionic conductivity of a material like LSM, however, LSCF is orders of magnitude more conductive, and it is even more ionically conductive than GDC electrolyte material at the same temperature [52].

According to the Nernst-Einstein relationship, the ionic conductivity is proportional to the concentration [37,47] and diffusivity of oxygen vacancies. At room temperature, LSCF is stoichiometric with respect to oxygen in air [47] and becomes non-stoichiometric at temperatures above 600°C and at a pO_2 below 1.3×10^{-3} atm [53,54].

2.4 Oxygen transport parameters D and k

Oxygen transport through MIECs via defects is generally well understood [9], but surface processes remain unclear due to experimental limitations and variations. In the literature, transport between the gas/solid interface is commonly described by two parameters, the bulk diffusivity (D) and surface exchange coefficient [14,16,55] (k_{se}). D and k_{se} values are usually found experimentally by applying one of the following driving forces to the material under study: electrical potential gradient, isotopic tracer concentration gradient [40,56] or chemical potential gradient [14,57]. However, k_{se} values found from different techniques are usually not comparable for reasons given by Maier [58]. Attempts have been made to correlate the k_{se} values to the mechanism of oxygen reduction using chemical kinetics [25,58-60], but a consistent expression for a given mechanism has yet to emerge.

One technique used to get D and k_{se} is called conductivity relaxation, which utilizes an abrupt change in the pO_2 to generate a change in the conductivity of the sample. Additionally, another difficulty of studying oxygen reduction on oxides is that the large oxygen background from the lattice makes it difficult to study the reacting oxygen on the surface, therefore the use of isotopically labeled oxygen, $^{18}O_2$, is necessary. More recently, D and k_{se} values have been

obtained from isotope exchange depth profiles (IEDP), which are generated from secondary ion mass spectrometry on samples that have been annealed in isotopically enriched oxygen [21,22,55]. k_{se} and D values obtained using an isotopic tracer are designated k^* and D^* . At 800 °C in 1 atm of O_2 , k^* for LSM and LSCF is 6.3×10^{-9} and 1.0×10^{-5} cm/s, respectively [36,40]. D^* is 4.0×10^{-15} cm²/s for LSM [40] and 2×10^{-8} cm²/s for LSCF [36]. These values show that oxygen transport through LSCF is clearly more facile than in LSM.

There is evidence that, in general, IEDP is much more sensitive to D than k_{se} . A couple of studies [56,61] show excellent agreement between the fitted and measured depth profile for the bulk of the material, but not within the first 10-20 nm, which is where k_{se} is most significant. The work by De Souza [25] shows large error bars for k_{se} but not for D . Lane [36] finds good agreement between D values from IEDP and conductivity relaxation but finds no apparent relationship between the measured k_{se} values.

An important sample property is the characteristic length, L_c , which is defined by the quantity D/k_{se} [62]. For sample geometries much larger than L_c , oxygen transport is limited by diffusion through the bulk while samples much smaller than L_c are kinetically limited by reactions occurring on the surface. This concept was explored in Lane's conductivity relaxation study [14] on bars (1.5×10^3 μm thick) of LSCF, which were found to have a characteristic length of 10^3 μm at 800 °C; the characteristic length for LSM is much smaller and, from IEDP studies, appears to be 8×10^{-3} μm at 900 °C (2×10^3 μm thick disk) [22]. Sample dimensions in these experiments are typically similar to or much larger than L_c , which means that the measurements are significantly affected by bulk transport kinetics.

2.5 Gas phase isotopic oxygen exchange

One way to ensure that surface kinetics is the dominating process is to use powder samples. Isotopic exchange techniques have been used since the 1940's to study the surface

oxygen exchange rate of various oxides [27,63-67]. In these experiments, the powder sample was confined in a closed system, sometimes with a gas recirculating design, and allowed to equilibrate with normal oxygen at a chosen temperature and oxygen partial pressure. Then, isotopically labeled oxygen gas was introduced and the gas phase composition was monitored for the three oxygen isotopologues (molecules that differ only in isotopic composition) using a mass spectrometer. The analysis in these early studies was overly simplistic and often neglected key steps such as adsorption, which may in fact dominate these surface processes. It was found [68] that these earlier models were quite limited and a more rigorous approach to find the mechanism and rate limiting step of surface exchange is preferred.

The main focus of this body of work is using the more modern technique of steady state isotopic transient kinetic analysis (SSITKA) [69] to determine kinetic information for cathode materials and using temperature programmed isotopic exchange to measure catalytic activity. With SSITKA, a plug flow reactor is used in place of the recirculating system, resulting in more sensitive and rapid gas composition detection, and a constant feed stream composition that makes data analysis more straightforward. A mass spectrometer located immediately downstream from the reactor continuously monitors the gas phase composition. The experiment is based on the rapid switching of the reactor feed line between streams containing different isotopes of oxygen. Ideally the only change induced by the switch is a step in oxygen labeling. Temperature, pressure, flow rate and oxygen partial pressure should remain undisturbed. The following analysis is then honed for reversible reactions such as gas phase oxygen exchange with the solid. In contrast to previously mentioned techniques (IEDP, conductivity relaxation) which yield overall mass transport information (such as surface exchange coefficient and diffusion

constants), this method has the potential to reveal not only the mechanism of oxygen exchange, but also the kinetic rate constants which determine the overall reaction rate.

Another technique used in this dissertation is called temperature programmed reaction, which quickly surveys a material's behavior at different temperatures. These experiments involve flowing gas of a known composition into the reactor while increasing the temperature at a constant rate and monitoring the reactor effluent in real time. The relative catalytic activity of two different materials can be compared by determining the onset temperature for reaction, desorption or isotopic exchange.

Because of the apparent similarity between the IEDP technique [22,37,44,55,56] and this work, it is important to first establish the conceptual similarities and differences between these two methods. Both techniques assume that the interaction of $^{18}\text{O}_2$ with the sample material is identical to that of $^{16}\text{O}_2$, and that the flux of oxygen entering the material is equal to that leaving. It is not possible to study any charge transfer step(s) from either technique. The main difference is the SSITKA based method is a more catalysis based approach and aims to determine the mechanism of oxygen incorporation into the solid using chemical kinetics and the concept of rate coefficients whereas the IEDP method extracts the D and k_{se} values *ex situ* by fitting the isotopic penetration depth profile in the solid to the Crank solution to the diffusion equation. As mentioned before, it is difficult to conclude what the kinetic mechanism is from k_{se} .

Using oxygen isotope $^{18}\text{O}_2$ as a tracer to differentiate from the ^{16}O found in the solid, it is possible to follow the oxygen exchange process in real time and elucidate the kinetic dependence on temperature and $p\text{O}_2$ for these materials through temperature programmed and isothermal exchange methods. By tracking the rise and fall of different oxygen species (seen as masses 32, 34 and 36 from the mass spectrometer), the uptake and release of oxygen can be better

understood (Figure 2-4). Mass 32 represents $^{16}\text{O}_2$ coming from the bulk of the material while mass 36 is the labeled oxygen $^{18}\text{O}_2$ from the gas stream. Mass 34 represents the scrambled product $^{16}\text{O}^{18}\text{O}$ that results from heteroexchange [70] between the gas and solid phases.

Because oxygen is a relatively stable molecule, exchange between oxygen molecules in the gas phase (homoexchange) without interaction with those from the solid is not significant at temperatures below 1000°C and will not be considered in the analysis [70]. Furthermore, verification that homoexchange did not occur in a blank reactor was done by flowing a mixture of $^{18}\text{O}_2$ and $^{16}\text{O}_2$ and monitoring for any changes while increasing the temperature from $50\text{-}800^\circ\text{C}$.

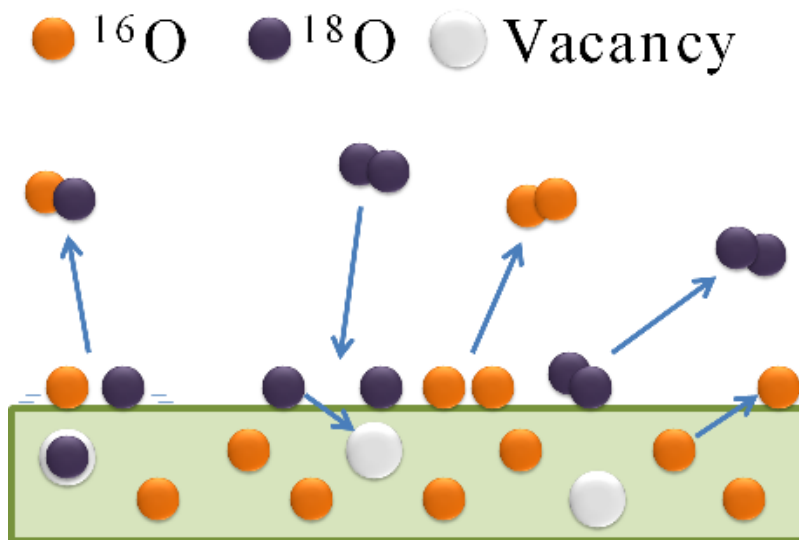


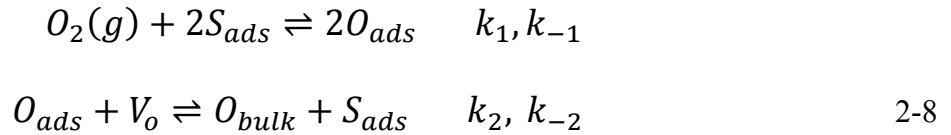
Figure 2-4. Oxygen exchange showing possible species formed [71]

Each material's active temperature range is first identified from temperature programmed experiments, and then isothermal isotopic exchange is used to obtain kinetic parameters that can be compared to a theoretical model, discussed in the next section. From a simple two step mechanism of dissociative adsorption followed by incorporation, oxygen partial pressure dependencies, which are determined by the rate limiting step, are extracted. The extracted

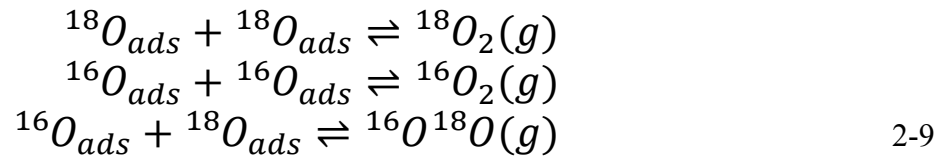
parameter values are used to reconstruct the time dependent gas behavior and the extent of exchange.

2.6 Proposed Mechanism of Oxygen Exchange

The actual mechanism for oxygen exchange may be quite complex, involving a multitude of possible steps [72]. However, as a starting point, a simple 2-step model (equation 2-8) is proposed [71]. Charge transfer is not considered a separate step in this analysis because no electrical measurements were made. The first step is the dissociative adsorption of a molecule of oxygen on the surface. This is followed by the incorporation of the adsorbed oxygen atom into the solid. The (g) indicates the gas phase, S indicates a surface site and V_o is a vacancy at the surface of the material. The “ads” or “bulk” subscripts indicate an adsorbed or bulk species.



The k's are the forward and backward reaction rate constants for each step. In this work, the measured quantity is the concentration of $O_2(g)$ from the first step. Introducing an isotopic tracer into the system allows for the formation of three different oxygen species $^{16}O_2$, $^{18}O^{16}O$, and $^{18}O_2$, which are produced on the surface according to the equations in 2-9. These equations represent the backward reaction of the first step in the model (equation 2-8).



From the assumptions that the surface and gas are in equilibrium with each other, the composition of the gas phase oxygen species can be used to back derive the statistical distribution of oxygen isotope ^{16}O or ^{18}O adsorbed at the surface. This serves as the starting point

for much of the isotopic exchange (both temperature programmed and isothermal) analysis to follow. Overall, the gas interacts with the oxygen adsorbed at the surface, which then interacts with the oxygen in the sample lattice. All three phases (gas, surface and bulk) can be modeled using this relatively simple two step process.

All that remains is to link the measured quantities to the rates of production. Illustrated next is a schematic of the reactor (figure 2-5) with the flow of feed and reaction products. The reaction is assumed to occur at feed conditions as the reactants are quickly swept away. There is also no accumulation within the reactor since the residence time of the gas is fairly small. A constant flux, F , of $^{18}\text{O}_2$ enters the reactor and reacts with the oxide sample to form $^{18}\text{O}_2$, $^{16}\text{O}_2$ and $^{16}\text{O}^{18}\text{O}$. The fluxes of the products, F'' , are monitored by the mass spectrometer.

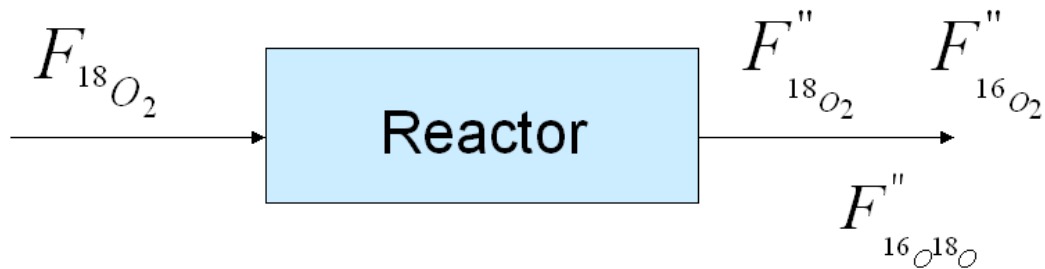


Figure 2-5. Schematic showing reactor feed and products [71]

From mass balance (equation 2-10), the following expressions for the production of the various oxygen species are derived. SA is the sample surface area. For the last two equations

$$\text{Accumulation} = 0 = F_{\text{in}} - F_{\text{out}} + \text{rate produced} - \text{rate consumed} \quad 2-10$$

$$SA \frac{d[^{18}\text{O}_2]}{dt} = F_{^{18}\text{O}_2} - F''_{^{18}\text{O}_2} + k_{-1} [^{18}\text{O}_{\text{ads}}]^2 - k_1 P_{\text{O}_2}^{18} \quad 2-11$$

$$SA \frac{d[^{16}\text{O}^{18}\text{O}]}{dt} = -F''_{^{16}\text{O}^{18}\text{O}} + k_{-1} [^{18}\text{O}_{\text{ads}}] [^{16}\text{O}_{\text{ads}}] \quad 2-12$$

$$SA \frac{d[{}^{16}O_2]}{dt} = -F_{{}^{16}O_2} + k_{-1}[{}^{16}O_{ads}]^2 \quad 2-13$$

(2-12 and 2-13), it is apparent that the quantity measured by the mass spectrometer is directly proportional to the rate of production. Using this link between the measured and theoretical rate of production, a simulation of the exchange reaction is possible and used to deduce the most likely mechanism of isotopic exchange.

CHAPTER 3
TEMPERATURE PROGRAMMED EVALUATION OF CATALYTIC PROPERTIES

3.1 Introduction

Temperature programmed reaction (TPR) is a characterization technique used in the field of heterogeneous catalysis. The process involves flowing reactant gases through a bed of catalyst and measuring the composition of the effluent as the temperature is increased. Using TPR, the oxygen non-stoichiometry of $(\text{La}_{0.8}\text{Sr}_{0.2})_{0.98}\text{MnO}_{3\pm\delta}$ (LSM) and $\text{La}_{0.6}\text{Sr}_{0.4}\text{Co}_{0.2}\text{Fe}_{0.8}\text{O}_{3-\delta}$ (LSCF) can be measured under different temperature and $p\text{O}_2$ conditions, and compared to that in the literature as a means to validate this technique.

A variation of TPR, temperature programmed desorption (TPD), is used for investigating the desorption of oxygen from the surface. First, adsorbates are adsorbed onto the catalyst by flowing the gas of interest through a cooling catalyst bed. Once the starting temperature is reached, an inert gas such as nitrogen or helium is used for the feed stream to carry off any excess reactant gas [73]. Then the temperature is linearly ramped and the desorbing species is detected with a mass spectrometer. TPD can yield information on the surface coverage and differentiate between different binding sites.

Another variation is temperature programmed isotopic exchange (TPX), which sheds light on the interaction between the oxygen in the gas and solid phase. First the oxide catalyst is annealed in a stream containing normal $^{16}\text{O}_2$ and cooled back down to room temperature to ensure that the oxygen in the solid is of normal isotopic labeling. Then the oxygen in the feed stream is replaced with labeled oxygen ($^{18}\text{O}_2$). The different oxygen species ($^{18}\text{O}_2$, $^{18}\text{O}^{16}\text{O}$, and $^{16}\text{O}_2$) in the gas are then monitored as the reactor is heated [18]. The temperature of exchange onset is then an indicator of the catalytic activity. Depending on the evolution of the oxygen species relative to each other, differences in mechanism can be detected.

3.2 Experimental

3.2.1 Powder Materials

$(\text{La}_{0.8}\text{Sr}_{0.2})_{0.98}\text{MnO}_{3-\delta}$ powder from Nextech ($5.73 \text{ m}^2/\text{g}$) and $\text{La}_{0.6}\text{Sr}_{0.4}\text{Co}_{0.2}\text{Fe}_{0.8}\text{O}_{3-\delta}$ powder from Praxair ($6.53 \text{ m}^2/\text{g}$) were used without additional modification. By testing each cathode material individually, interaction between dissimilar materials (such as secondary phase formation between electrolyte and cathode) can be avoided.

3.2.2 Catalysis System

The continuous flow system (Figure 3-1) consists of two separate gas lines connected to a switching valve with one line exiting to vent and the other leading to a small quartz micro-reactor. Inside the reactor, gas flows through a bed containing a small quantity of powder sample supported by quartz frit (Figure 3-2). The reactor effluents flow to a quadrupole mass spectrometer (Extrel QMS), where the composition is analyzed and recorded. A temperature controller (Eurotherm) connected to a type-K thermocouple in the reactor controls furnace temperature.

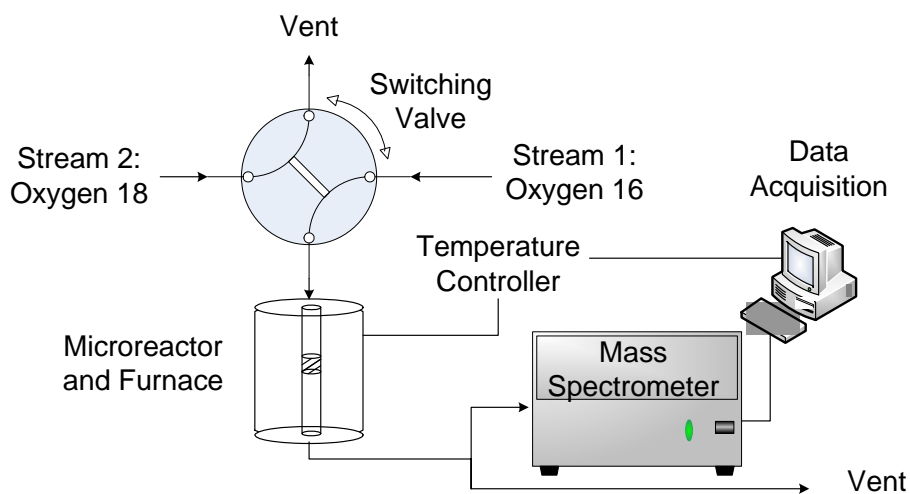


Figure 3-1. Catalytic testing system comprised of two separate feed streams, a microreactor within a furnace and quadrupole mass spectrometer [71]

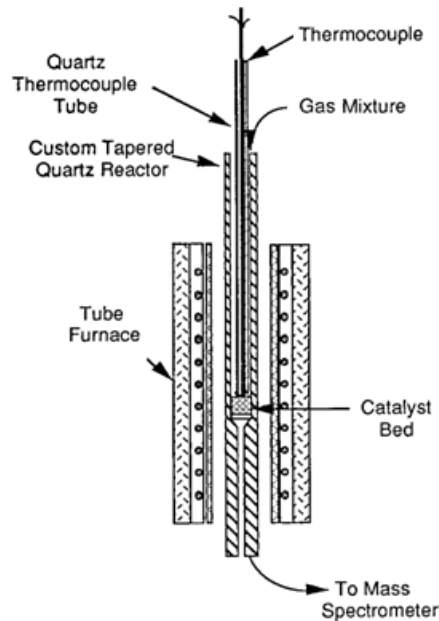


Figure 3-2. Quartz micro-reactor schematic [74]

Each gas line contains multiple mass flow controllers connected to oxygen gas and research grade helium tanks (Airgas). All gas mixtures were balanced in helium. Stream 1 contained oxygen isotope $^{16}\text{O}_2$ while stream 2 contained oxygen isotope $^{18}\text{O}_2$ (Cambridge Isotope, 95% pure) and a small amount of argon (Airgas, 0.1%) used as an inert tracer. Mass flow controllers (MKS & Alicat) and exhaust valves were adjusted so that the two lines were flow and pressure matched. After each experiment, the mass spectrometer was calibrated by flowing gases of a known composition through a room temperature reactor. Flow rates were verified using a bubble-meter connected to one of the exhausts. Masses 16, 18, 28, 32, 34, 36 and 40 were monitored during every run. Mass 28 corresponds to either N_2 or CO and mass 40 represents the inert argon tracer. Because the uptake and release of oxygen is repeatable in LSCF [19], this fact was used to calculate relative sensitivity factors (RSF) for mass 32, 34 and 36 from a series of TPR experiments.

3.2.3 Temperature Programmed Reaction, Desorption and Exchange

The sample was loaded into the quartz reactor and pretreated for 10 minutes at 650°C. After pretreatment, the reactor was cooled to room temperature in the pretreatment gases and then the reacting gases were flowed through the reactor (Table 3-1). Once steady state conditions were reached (approximately 30 minutes), the temperature was ramped up to between 650°C and 800°C at a rate of 30°C/minute while the composition of the reactor effluent was recorded. For TPD, the sample was cooled in an oxygen atmosphere and heated in an inert helium stream. The TPR involved heating the sample in an oxygen containing feed stream, while the TPX is nearly identical to the TPR except the oxygen in the feed stream was isotopically labeled.

Table 3-1. Temperature programmed conditions [71]

Temperature Programmed Experiment	Sample Size (mg)	Flow Rate (ml/min)	Pretreatment Gas	Reaction Gas	Feed Stream O ₂ Content (ppm)
Reaction (TPR)	15-LSCF 17-LSM	20	1% ¹⁶ O ₂	¹⁶ O ₂ , He	2,500; 5,000; 10,000
Exchange (TPX)	40	25	1% ¹⁶ O ₂	¹⁸ O ₂ , He	2,500
Desorption (TPD)	40	25	1% ¹⁶ O ₂ , 2,500ppm ¹⁸ O ₂	He	<10

3.3 Results and Discussion

3.3.1 Oxygen Non-Stoichiometry from TPR

In order to determine the validity of this technique, the oxygen non-stoichiometry of LSM and LSCF was found using our quantitative mass spectrometry method and compared to published results.

LSM was heated in 2,500 and 5,000 ppm oxygen. At no time did the oxygen signal increase noticeably beyond the baseline, indicating that the LSM oxygen stoichiometry is constant throughout the temperature range 50-700°C. This is in agreement with results obtained by Kuo [38], which indicate that LSM has few vacancies under these conditions.

The oxygen vacancy concentration of $\text{La}_{0.6}\text{Sr}_{0.4}\text{Co}_{0.2}\text{Fe}_{0.8}\text{O}_{3-\delta}$ calculated from a series of TPRs under various oxygen partial pressures is shown in Figure 3-3. As expected, the oxide deviates from stoichiometry ($\delta=0$) as the temperature was increased or the oxygen partial pressure was decreased. ($3-\delta$) values at 800°C are similar to those interpolated from Hartley's study on oxygen non-stoichiometry [54], although the data from this study indicates that LSCF is more sensitive to the oxygen partial pressure. Interpolated data from Hartley appear as dots. Due to the smaller sample size in our study (15 mg), calibration errors and differences in detection method could have contributed to the discrepancy. The sample size was weighed out to yield a total surface area of approximately 0.1m^2 for each material: 17 mg of LSM powder and 15 mg of LSCF powder.

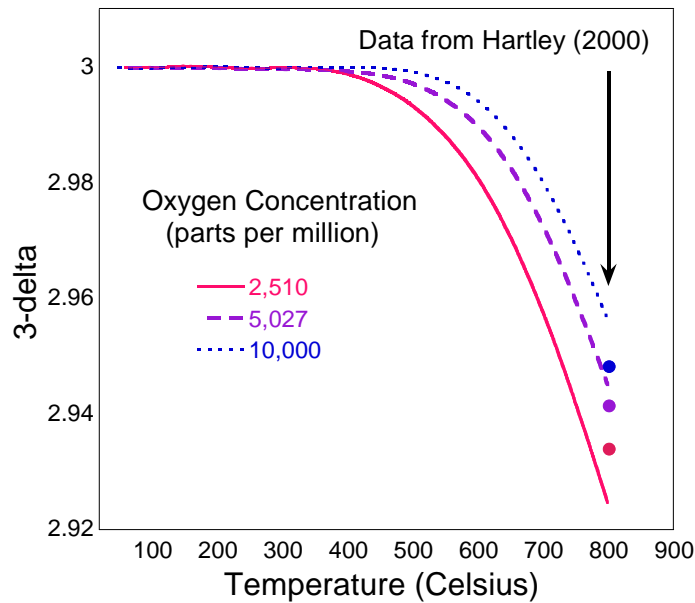


Figure 3-3. $\text{La}_{0.6}\text{Sr}_{0.4}\text{Co}_{0.2}\text{Fe}_{0.8}\text{O}_{3-\delta}$ Oxygen non-stoichiometry ($3-\delta$) vs. temperature for various oxygen partial pressures. The circles at 800°C represent points interpolated from Hartly's work [54,71].

3.3.2 Temperature Programmed Isotopic Exchange

Heating the sample at a constant rate in isotopically enriched oxygen gas revealed the formation of $^{16}\text{O}^{18}\text{O}$, as well as the exchange of gas phase oxygen ($^{18}\text{O}_2$) with that in the bulk ($^{16}\text{O}_2$). Figure 3-4 shows the exchange behavior of LSM and LSCF. Onset of oxygen exchange in LSCF began around 200°C, while it did not begin until 350°C for LSM, indicating LSCF is more catalytically active. The isotopic exchange sample size is larger than the TPR sample size to maximize detection of isotopic exchange.

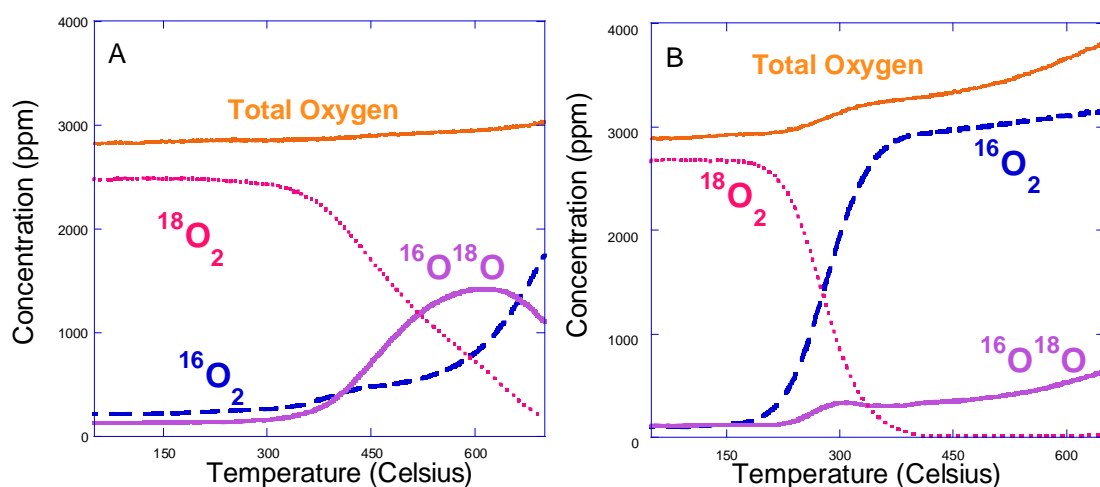


Figure 3-4. Temperature programmed exchange profile for A) LSM and B) LSCF [71]

LSM shows extensive $^{16}\text{O}^{18}\text{O}$ formation and little bulk oxygen desorption up to 600 °C, which suggests a more rapid dissociative adsorption step relative to the incorporation step. Much of the ^{18}O from the gas phase $^{18}\text{O}_2$ dissociates on the LSM surface and, rather than becoming incorporated into the lattice, desorbs back into the gas phase as $^{16}\text{O}^{18}\text{O}$. This is consistent with LSM's behavior as an electronic conductor with few vacancies and low oxygen diffusivity. The decrease in $^{16}\text{O}^{18}\text{O}$ starting at 620°C suggests either a change in the reduction mechanism or the exhaustion of $^{16}\text{O}_{\text{ads}}$ species at that point. The total oxygen does increase slightly around 500°C, which was not observed in earlier TPR experiments performed with regular $^{16}\text{O}_2$. This may be

due to calibration error or it could also indicate that the material is slightly sub-stoichiometric under testing conditions at higher temperature.

Although some surface scrambling (formation of $^{16}\text{O}^{18}\text{O}$) takes place on LSCF (Figure 2-4b), the majority of the gas phase oxygen ($^{18}\text{O}_2$) exchanges by switching places with the original bulk oxygen. Overall, more oxygen was released than absorbed by the oxide, and the oxygen ejected was primarily from the bulk. Because there was relatively little surface mixing, this indicates that step 2 is overall very fast compared to step 1. These results are consistent with those obtained from Boukamp's study [75] on $\text{La}_{1-x}\text{Sr}_x\text{CoO}_3$ based perovskites. Boukamp and co-workers also observed relatively little cross product formation in their sample while observing that the labeled oxygen exchanged with the solid by replacing the bulk oxygen ^{16}O .

3.3.3 Temperature Programmed Desorption after Isotopic Exchange

Running a TPD after the TPX on both materials revealed that the oxygen lattice was of mixed isotope. TPD spectra obtained after adsorption in regular $^{16}\text{O}_2$ follow the same shape and magnitude of total oxygen desorbed.

The TPD for LSM (Figure 3-5a) shows two noteworthy characteristics. First, the presence of $^{16}\text{O}^{18}\text{O}$ indicates that some exchange did occur in LSM, and second, the amount of oxygen given off by the sample is very small compared to LSCF. This profile is similar to those presented in previous works [20,76], which also show the base of a desorption peak starting near 500°C . Although the peaks at 175°C and 350°C were not seen in the earlier studies [20,76], they are very small and can arise from differences in catalyst pretreatment.

The profile for LSCF is shown in Figure 3-5b, with one view zoomed in to show contributions to the low temperature "peak" near 230°C . This peak was also seen at the same temperature in another study [19]. Overall, the majority of the desorbed oxygen consisted of the non-exchanged species ^{16}O from the lattice. Upon closer inspection of the low temperature peak,

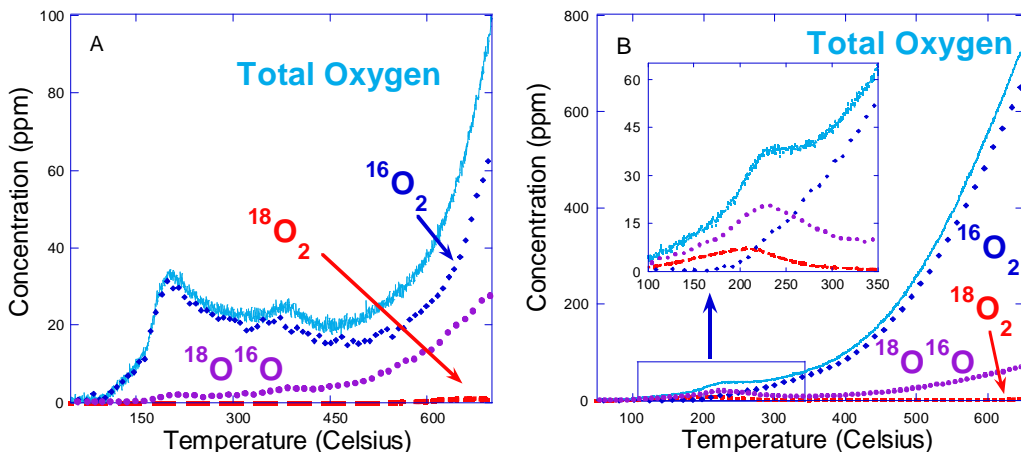


Figure 3-5. Temperature programmed desorption after TPX for A) LSM B) LSCF, broken down by isotopic labeling [71]

called the α -peak [17,73], it is apparent that there may be an oxygen surface state at room temperature. It is likely that the labeled species originates as oxygen either in the surface layer or as an adsorbate and as the temperature increases, more bulk oxygen is expelled from the lattice as the material equilibrates with the environment [73]. Because the $^{16}\text{O}^{18}\text{O}$ is twice the value of the $^{18}\text{O}_2$, it is evidence that the “low temperature” surface state of oxygen is atomic. During pretreatment in the labeled gas, the isotopically labeled oxygen accumulates near the surface due to slow diffusion as the sample cools; this explains the corresponding low temperature peak in $^{18}\text{O}_2$. It should be mentioned that the total oxygen TPD profile is reproducible regardless if it is performed with regular or labeled oxygen adsorbate.

3.4 Conclusion

The oxygen non-stoichiometry of LSM and LSCF obtained by temperature programmed reaction is comparable to values reported in the literature. Using an isotopic tracer, it was shown that oxygen surface exchange occurs in LSCF above 200°C and in the electronic conductor LSM above 350°C. At all temperatures tested, LSCF is more catalytically active than LSM with regard to exchange. The amount of scrambled surface species formation is indicative of the nature of the

oxygen exchange reaction; LSM shows difficulties with incorporation while LSCF appears to be limited by the dissociative adsorption step.

Desorption studies performed after the isotopic exchange experiment shows that there is a low temperature (100-300°C) peak for both LSM and LSCF. The release of mixed product is further proof that the exchange between the gas and solid oxygen species does occur. The magnitude of desorption is much smaller for LSM than with LSCF. It is thought that the high temperature desorption “peak” originates from the oxide bulk rather than from the desorption of oxygen adsorbates.

CHAPTER 4 ISOTHERMAL ISOTOPIC SWITCHING

4.1 Introduction

Once the active temperature range for $(\text{La}_{0.8}\text{Sr}_{0.2})_{0.98}\text{MnO}_{3\pm\delta}$ (LSM) and $\text{La}_{0.6}\text{Sr}_{0.4}\text{Co}_{0.2}\text{Fe}_{0.8}\text{O}_{3-\delta}$ (LSCF) are identified from temperature programmed experiments, isothermal isotopic exchange can then be performed to obtain an exchange profile, which is compared to the theoretical model. This method is also called the steady state isotopic transient kinetic analysis technique, described in detail by Shannon and Goodwin [69].

This technique involves feeding a gas mixture of $^{16}\text{O}_2$ of a known concentration into a reactor containing the cathode powder at constant temperature and abruptly switching the gas feed stream to one containing the same concentration of $^{18}\text{O}_2$. The oxygen isotope distribution in the reactor effluent versus time is then monitored by mass spectrometry to generate exchange profiles. Ideally the only change induced by the switch is a step in oxygen labeling. Temperature, pressure, flow rate and oxygen partial pressure should remain undisturbed.

It is generally believed that the surface reaction process can be broken down into several steps: first gas diffuses to the surface, then it adsorbs and reacts on the surface, and finally is followed by desorption away from the surface. The mechanism of oxygen reduction on $(\text{La}_{0.8}\text{Sr}_{0.2})_{0.98}\text{MnO}_{3\pm\delta}$ (LSM) and $\text{La}_{0.6}\text{Sr}_{0.4}\text{Co}_{0.2}\text{Fe}_{0.8}\text{O}_{3-\delta}$ (LSCF) are thought to be different. Since LSM is an electronic conductor with poor ionic conductivity, it is thought that the oxygen reduction reaction is limited to the triple phase boundary where gas, electrode and electrolyte meet. With LSCF, which is a mixed ionic electronic conductor, diffusion through the bulk oxide is thought to be facile and as a result, the whole surface is active for oxygen reduction.

From a simple two step mechanism, the oxygen partial pressure dependencies can be extracted, which are determined by the rate limiting step. Also, the kinetic parameters are

extracted and used to reconstruct the time dependent gas behavior and the extent of exchange. Many parallels can be made between this study's modeling approach and an earlier Monte Carlo simulation [77] of the gas phase composition applied to fluorite structured oxides. In addition to simulating the evolution of the gas phase oxygen composition with time, this work also models the exchange behavior of the bulk from the measured gas phase reaction.

4.2 Theory

Starting with the 2 step mechanism mentioned in Chapter 2, equation 2-8, the overall rate is defined by the extent of oxygen incorporation into the solid (second step). Although the total oxygen concentration is nearly constant during an isotopic switch experiment, there is an isotopic driving force and eventually labeled oxygen ^{18}O from the gas phase replaces lattice ^{16}O . Therefore it is possible to track the overall reaction rate as $d[^{18}\text{O}_o]/dt$ using isotope mass balance. Because the relative differences in mass and bonding energy are small amongst diatomic oxygen species, isotopic effects are ignored for the sake of simplicity [69].

In the limit that one of the two steps is rate determining, two different behaviors can be predicted. If one step is assumed to be in quasi-equilibrium with respect to the labeled oxygen concentration, a simplified expression can be written using the equilibrium constants $K_1=k_1/k_{-1}$ and $K_2=k_2/k_{-2}$ to yield the initial oxygen dependence of the overall rate of ^{18}O incorporation.

In the case of step 2 being in quasi-equilibrium, at time $t \approx 0$, $[^{18}\text{O}_{\text{ads}}]=[^{18}\text{O}_o] \approx 0$.

$$\text{rate} = \frac{d[^{18}\text{O}_o]}{dt} = K_2 \frac{[V_o]}{[S]} \frac{d[^{18}\text{O}_{\text{ads}}]}{dt} \stackrel{t \approx 0}{\Rightarrow} 2K_2 k_1 [V_o][S] P_{^{18}\text{O}_2} \quad 4-1$$

However this is not the case when step 1 is in quasi-isotopic equilibrium.

$$\text{rate} = \frac{d[^{18}\text{O}_o]}{dt} = k_2 [V_o][S] K_1^{0.5} P_{^{18}\text{O}_2}^{0.5} \quad 4-2$$

The initial reaction order with respect to O₂ is then predicted to be either 1 or 0.5 depending on whether dissociative adsorption or incorporation, respectively, is rate limiting.

In this study, the measured quantity is the concentration of O₂ (g) from the first step. Introducing an isotopic tracer into the system allows for the formation of three different oxygen species ¹⁶O₂, ¹⁸O¹⁶O, and ¹⁸O₂, which are produced on the surface according to equations 4-3 through 4-5 (the extra “2” in equation 4-4 arises from the reaction multiplicity). These equations represent the backward reaction of the first step in the model (equation 2-8). Equation 4-6 shows the normalization relationship for oxygen adatoms of a particular isotopic labeling, assuming that the total oxygen adsorbate concentration is constant during the switch due to steady state conditions.

$$\frac{d[{}^{16}\text{O}_2]}{dt} = k_{-1}[{}^{16}\text{O}_{\text{ads}}]^2 = k_{-1}[\text{O}_{\text{ads}}]^2({}^{16}f_{\text{ads}})^2 \quad 4-3$$

$$\frac{d[{}^{18}\text{O}{}^{16}\text{O}]}{dt} = 2k_{-1}[{}^{16}\text{O}_{\text{ads}}][{}^{18}\text{O}_{\text{ads}}] = 2k_{-1}[\text{O}_{\text{ads}}]^2({}^{16}f_{\text{ads}})(1 - {}^{16}f_{\text{ads}}) \quad 4-4$$

$$\frac{d[{}^{18}\text{O}_2]}{dt} = k_{-1}[{}^{18}\text{O}_{\text{ads}}]^2 = k_{-1}[\text{O}_{\text{ads}}]^2(1 - {}^{16}f_{\text{ads}})^2 \quad 4-5$$

$$\frac{{}^{18}\text{O}_{\text{ads}} + {}^{16}\text{O}_{\text{ads}}}{\text{O}_{\text{ads}}^{\text{total}}} = 1 = {}^{18}f_{\text{ads}} + {}^{16}f_{\text{ads}} \quad 4-6$$

If the oxygen on the surface and in the bulk is considered to be thoroughly mixed, and assuming that the total adsorbed and bulk oxygen concentration remains constant throughout the exchange, then the oxygen isotope distribution on the surface and in the solid can be represented in terms of fractions of one isotope (either 16 or 18). This simplification is also discussed in previous work [71]. The convention used here will focus on the fraction of adsorbed oxygen species on the material surface (¹⁶f_{ads}) and in the lattice (¹⁶f_{bulk}) which are of normal isotopic labeling (¹⁶O) because this is the isotope used for calibrating the mass spectrometer signal. Using equation 4-3, the ¹⁶f_{ads} at a given time is obtained from the instantaneous ¹⁶O₂ gas phase signal,

and serves as the starting point for much of the analysis. This allows us to use the measured gas phase composition during the exchange to predict the real time isotope distribution on and in the sample. $^{16}f_{\text{bulk}}$ can be obtained by integrating the amount of ^{16}O exchanged (from $^{16}\text{O}_2$ and $^{16}\text{O}^{18}\text{O}$) versus time and then normalizing to the sample size.

The time dependence of the system can be modeled with a system of nonlinear differential equations describing the isotopic composition of the surface and bulk (Figure 2-4), which depend on kinetic parameters and a correction to account for the purity of the isotopically labeled feed stream. The gas purity is taken into account by the following:

$$\alpha^{18}\text{O}_2 + \beta^{16}\text{O}_2 + \gamma^{16}\text{O}^{18}\text{O} = \text{Total O}_2 \quad 4-7$$

Where α is the fraction of $^{18}\text{O}_2$, β is the fraction of $^{16}\text{O}_2$ and γ is the fraction of $^{16}\text{O}^{18}\text{O}$ in the gas phase. Inserting these corrections into the derivation (see Appendix A) [71], the following system of equations is obtained.

$$\frac{d[^{16}f_{\text{ads}}]}{dt} = k_{-1}[\text{O}_{\text{ads}}](2\beta + \gamma - [^{16}f_{\text{ads}}]^2 - [^{16}f_{\text{ads}}]) + k_2[V_o]([^{16}f_{\text{bulk}}] - [^{16}f_{\text{ads}}]) \quad 4-8$$

$$\frac{d[^{16}f_{\text{bulk}}]}{dt} = k_2[V_o] \frac{[\text{O}_{\text{ads}}]}{[\text{O}_{\text{bulk}}]} ([^{16}f_{\text{ads}}] - [^{16}f_{\text{bulk}}]) \quad 4-9$$

From here, the following parameters are defined: $A = k_{-1}[\text{O}_{\text{ads}}]$; $B = k_2[V_o]$; $C = [\text{O}_{\text{ads}}]/[\text{O}_{\text{bulk}}]$. The parameters A and B are representative of the kinetics that describe the oxygen exchange reaction and are the effective rate constants; the smaller of the two rate constant will indicate if the reaction is dissociative adsorption limited (smaller A) or incorporation limited (smaller B). C is the ratio of adsorbed oxygen to oxygen in the bulk. Note that extracting the parameters A, B and C from the experimental data will require solving the system of nonlinear equations 4-8 and 4-9 using numerical methods.

This method of evaluating the isotopic composition of the surface and bulk, as predicted by the measured gas composition, will allow the validity of this model, along with its assumptions, to be thoroughly tested.

4.3 Experimental

The materials (LSM and LSCF) and experimental setup are the same as described in sections 3.2.1 and 3.2.2. Previously, the sample was heated at a constant rate while the feed gas was held constant. In this chapter, the temperature is held constant and the gas stream is varied.

4.3.1 Isothermal Isotopic Switching

Switching experiments consist of isothermally and isobarically (with respect to total oxygen pressure) switching the gas feed stream into the reactor from a line containing a mix of normal $^{16}\text{O}_2$ and helium to a secondary line containing $^{18}\text{O}_2$ (Cambridge Isotope, 97% enriched) and helium mixed to the same concentration. A small amount of argon (1,000 ppm) is included in this second line as an inert tracer. The change in isotope concentration is recorded using mass spectrometry (Extrel). The common gases are metered with MKS mass flow controllers while an Alicat Scientific mass flow controller is used with the isotopically labeled oxygen. Flow rates [20 standard cubic centimeters per minute (sccm) total unless stated otherwise] were calibrated using a bubblemeter and mass spectrometer signals were calibrated by flowing known concentrations of oxygen balanced in helium through the reactor. A typical room temperature gas switch profile, without reaction, is shown in Figure 4-1. Within 20 seconds, switch has reached new equilibrium with the $^{18}\text{O}_2$ enriched oxygen feed stream, in terms of both $^{18}\text{O}_2$ and the inert Argon tracer.

After the sample was loaded into the reactor, the temperature and $^{16}\text{O}_2$ partial pressure was adjusted to the desired values in feed stream 1. In feed stream 2, the $^{18}\text{O}_2$ partial pressure, flow rate (20ml/min) and pressure (15-18 PSIA) were adjusted to match the conditions in the $^{16}\text{O}_2$

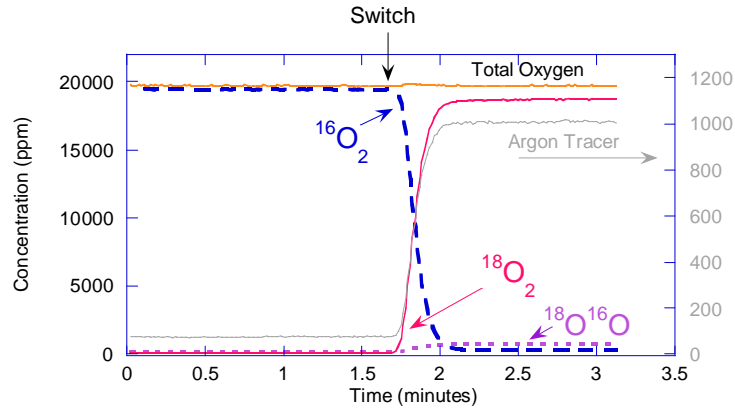


Figure 4-1. Oxygen isotopic switch profile through a room temperature reactor

line. Once steady state was reached, a rapid switching of the feed lines quickly changed the isotopic labeling of the reacting gases and the reaction was allowed to proceed for up to 5 minutes or whenever steady state was reached, whichever came first. Different combinations of temperature and oxygen concentration were systematically tested for each material. In order to extract the pO_2 reaction order at 600°C and 800°C, the temperature was held constant while the oxygen concentration was changed from run to run. To obtain the activation energies, the $^{18}O_2$ concentration was held at 20,000 parts per million (ppm) as the temperature changed from run to run. Because the reaction was assumed to be limited by surface kinetics, the sample size was normalized by surface area, which was approximately 0.1 m² for each material (17 mg of LSM powder and 15 mg of LSCF powder). A full exchange spectrum was taken at 650°C in 10,000ppm $^{18}O_2$ because the TPX spectrum shows extensive activity at this temperature for both materials. A full exchange spectrum entailed waiting until the mass spectrometer signals for masses 32, 34 and 36 have reached steady state and no more reaction was observed.

Additional isotopic switching experiments involved varying the temperature or oxygen concentration conditions of the test for the full duration of the exchange. Before switching tests, fresh powder was heated to 800 °C in approximately 20% $^{16}O_2$ for an hour to remove

contaminants. After testing, the sample is again heated to 800 °C in 20% $^{16}\text{O}_2$ for an hour to “reset” the lattice with ^{16}O . Tests on both materials were performed at 700 °C while varying the partial pressure of oxygen ($p\text{O}_2$) from run to run (0.5%, 1% and 2%). Then the $p\text{O}_2$ was kept at 2% while the temperature was held at 600, 700 and 800 °C. The oxygen partial pressures were chosen to avoid saturating the mass spectrometer detector. Also, the mass flow controller metering the isotopic oxygen has a maximum flow rate of 0.5 sccm, allowing for precise control but limiting the range of $p\text{O}_2$ achievable.

Upon finishing the set of switching experiments, it was noted that LSCF appeared to be gas diffusion limited due to its sample temperature insensitivity. In other words, the surface reaction is occurring more rapidly than the gas phase diffusion of reactants to the LSCF surface. This effect is not observed with LSM because its surface reaction occurs more slowly than diffusion and is thus rate limiting.

Because it is the surface kinetics which are of interest, it is necessary to either slow down the reaction on LSCF or decrease the boundary layer thickness such that gas phase diffusion is no longer limiting. The first approach taken was to double the flow rate to 40 sccm and then tests on LSCF were conducted at 600, 700 and 800 °C in 1% O_2 . Then the temperature was decreased to 300, 400 and 500 °C while holding the flow rate at 40 sccm and 1% O_2 . Some degradation was noticed so a new sample was used for the 40 sccm tests. Also, the sample size of LSCF was varied from between 5, 10 and 15 mg and tested under 40 sccm 1% O_2 at 500 °C.

4.4 Results and Discussion

4.4.1 $(\text{La}_{0.8}\text{Sr}_{0.2})_{0.98}\text{MnO}_{3\pm\delta}$

Figure 4-2 shows the evolution of various oxygen species with time immediately after the switch in feed stream oxygen labeling ($^{16}\text{O} \rightarrow ^{18}\text{O}$) for LSM at 650 and 800 °C under 10,000 ppm

of labeled oxygen. Time=0 was taken to be the time at which the inert argon signal was first detected and any data before that point was disregarded (Figure 4-3).

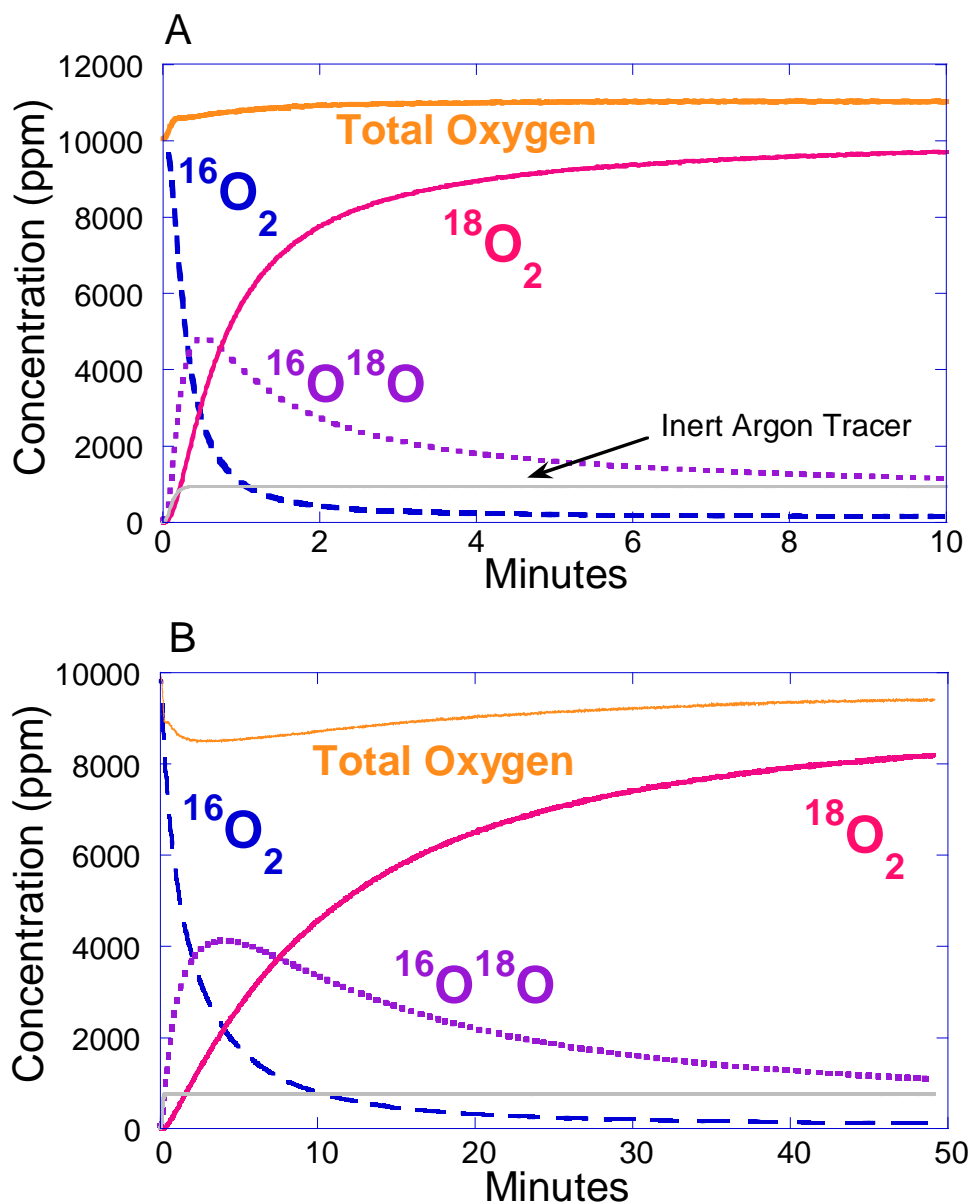


Figure 4-2. $(\text{La}_{0.8}\text{Sr}_{0.2})_{0.98}\text{MnO}_{3+\delta}$ isothermal isotopic exchange under 1% O_2 at A) 650°C and B) 800°C [71]

Comparing the time scale of the reaction in the profile from the switch in 1% O_2 (shown in Figure 4-2 for LSM) to that in Figure 4-1, the decay in the $^{16}\text{O}_2$ signal cannot be due to the switch itself and is attributed to the heterogeneous exchange with the ^{16}O containing sample.

These profiles show that the total oxygen concentration during the experiment is very stable, with the exception of the discontinuity near the switch (due to pressure imbalance between the two lines).

Total oxygen was reasonably constant throughout the experiment; the switch does introduce an initial discontinuity because the lines were closely, but not perfectly, flow, pressure and concentration balanced. $^{16}\text{O}_2$ falls off monotonically while $^{18}\text{O}_2$ increases with time as expected in both Figure 4-2a and b. $^{16}\text{O}^{18}\text{O}$ increases and reaches a maximum before gradually

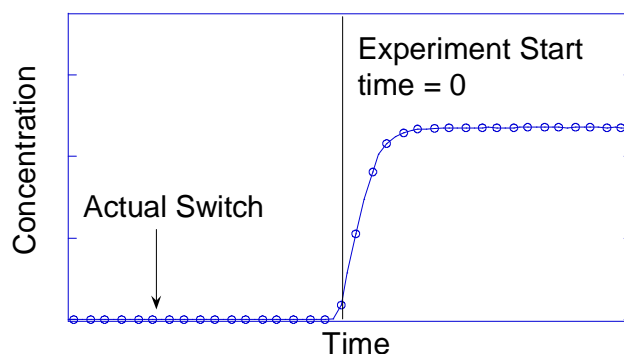


Figure 4-3. Argon Tracer Step-Profile [71]

dropping off. If exchange of any type had not occurred, there would be no formation of $^{16}\text{O}^{18}\text{O}$ and the time to switch isotopic labeling from $^{16}\text{O}_2$ to $^{18}\text{O}_2$ would be comparable to the argon switch time.

Although the y-axis of the figure is labeled concentration, it can also be considered the instantaneous rate of production of the three oxygen isotopologues. It is possible to know if exchange with the solid is actually occurring or not by comparing the amount of oxygen “exchanged” with the amount of oxygen present in the original sample. If exchange with the bulk occurs, the conversion will approach 100% as the experiment proceeds. If only the adsorbed oxygen species were exchanged, then this reaction will occur very quickly and the amount of oxygen exchanged will fall short of the amount needed to convert the oxygen in the lattice to

100% labeled oxygen. Therefore, to get the amount of oxygen exchanged, it is necessary to integrate the area under the $^{16}\text{O}_2$ curve plus half of the area under the $^{16}\text{O}^{18}\text{O}$ curve. To put into perspective the amount of time it takes for a full exchange to occur, under typical experimental conditions for our sample mass, it takes at least 20 minutes to flow enough labeled oxygen through the system to replace each oxygen in the sample lattice. The probability of replacing a ^{16}O in the lattice with an ^{18}O from the gas phase decreases with time which leads to long exchange times if 100% conversion is desired. Also, close to 100% conversion is not possible since our gas is enriched to only 97% ^{18}O (95% $^{18}\text{O}_2$).

Although the TPX (Figure 3-4a) would suggest that LSM is reactive at 350°C, that is merely the lower temperature limit for this material's reactivity. The sample size is larger and the oxygen partial pressure is lower in the TPX specifically so that the reactivity limit can be studied. Significant exchange from isothermal switching was not observed until the temperature increased past 600°C. At first glance at the time scales in Figure 4-2, it may appear that LSM reacts much faster at 650°C than at 800°C, however this is not really the case. The rapid production of the asymmetric molecule is primarily due to mixing with surface species. There is much more oxygen in the lattice that has not come out yet and it would take an extremely long time for the material to fully exchange. After increasing the temperature to 800°C, LSM shows characteristics of both surface and bulk exchange (Figure 4-2b) and subsequently takes much longer to approach steady state.

If the initial oxygen partial pressure dependence of the overall reaction is assumed to follow a power law ($\text{rate} \propto p_{\text{O}_2}^m$), it can be written in a linearized form (equation 4-10). Slopes

$$\ln\left(\frac{d[^{18}\text{O}_o]}{dt}\right) = \ln k_{\text{effective}} + m \ln P_{^{18}\text{O}_2} \quad 4-10$$

were calculated from the data at $t = 15$ seconds. The slope taken any earlier would incorporate switching nonidealities and any later would invalidate the assumption that the ^{18}O content in the surface and solid is zero. The $p\text{O}_2$ dependence for LSM at 600 and 800°C is shown in Figure 4-4. The switching nonideality is expected to cause greater error in the lower temperature LSM runs due to the more rapid attainment of steady state. The initial reaction order with respect to oxygen partial pressure for LSM is 0.67 at 600°C and 0.82 at 800°C, indicating that the rate determining step in LSM changes with temperature.

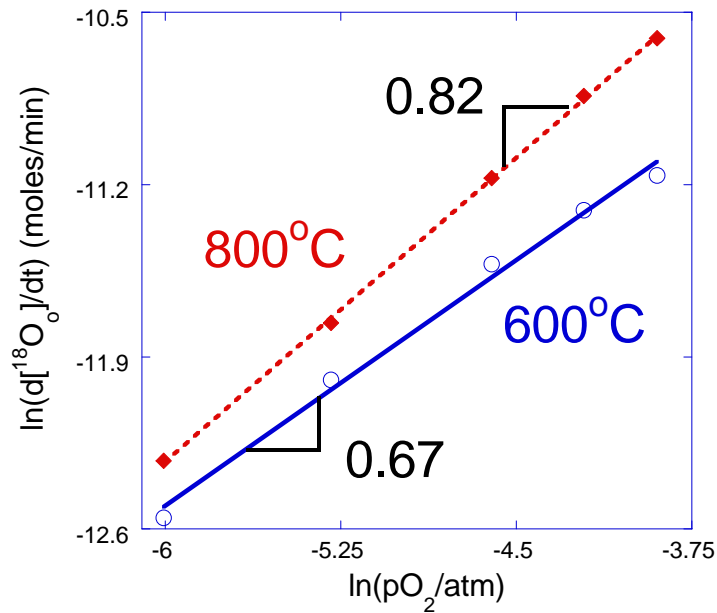


Figure 4-4. Initial rates of exchange vs. oxygen partial pressure for LSM at 600 and 800°C [71]

The change in $p\text{O}_2$ dependence between 600 and 800°C signifies that a change in the mechanism occurs somewhere between those two temperatures. To investigate further, a series of isothermal exchange experiments was conducted under 20,000 ppm oxygen at various temperatures. The first series of experiments investigated the behavior of LSM over the temperature range 600-800°C. By plotting the overall rate and temperature (Figure 4-5) on an

Arrhenius-like plot, the apparent activation energy was extracted from the different slopes. There was a transition region between 650°C and 700°C and a second series was conducted spaced 15°C apart between 650°C and 710°C (Figure 4-5 inset). The higher temperature slope corresponded to an activation energy of 0.90 eV while the lower temperature slope indicated a much lower activation energy of 0.41 eV. This reinforces the hypothesis that only adsorbed surface species were exchanging at temperatures lower than 650°C, since exchanging surface

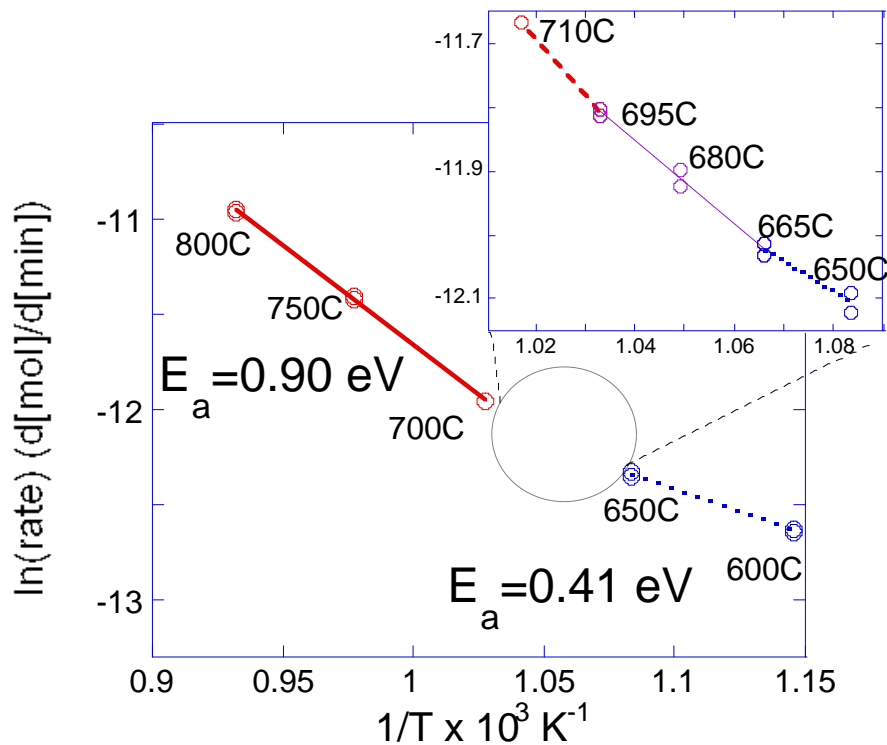


Figure 4-5. Arrhenius-like plot showing activation energy of oxygen exchange on LSM under 20,000 ppm $^{18}\text{O}_2$ [71]

species is a lower energy process. In order for surface adsorbate exchange to occur (step 1), oxygen only needs to adsorb and dissociate onto the surface; for actual exchange with the oxygen in the lattice to occur, additional energy needs to be spent on processes such as vacancy diffusion and creation. The cause of this change in mechanism may be a phase transition [78]. Previously reported values for the activation energy (from IEDP surface exchange coefficients)

in LSM was significantly higher: 1.33 eV at temperatures over 700°C [79]. This discrepancy may arise from differences in pO₂ testing conditions if there is a different mechanism (100% O₂ vs. 2% in this study) or sample configuration (as mentioned in the introduction, a compact body may be less sensitive to surface reactions compared to a powder).

4.4.2 La_{0.6}Sr_{0.4}Co_{0.2}Fe_{0.8}O_{3-δ}

Figure 4-6 shows the extended isothermal exchange behavior for LSCF at 650°C and 10,000 ppm oxygen concentration. Although Figure 4-6 is data from a specific combination of temperature and oxygen partial pressure, the trends remain the same for most temperatures and oxygen concentrations tested. At 400°C exchange occurs but not at 200°C, which is consistent with the TPX results (Figure 3-4b). At 200°C, the TPX shows that the exchange is rather slow and would not react fast enough to be seen in the switching experiments.

The lag in production of ¹⁶O¹⁸O, which is assumed to occur only on the sample surface, shows that the labeled oxygen does not displace the original surface species right away, but must gradually accumulate. This is consistent with a slow dissociation step and fast incorporation.

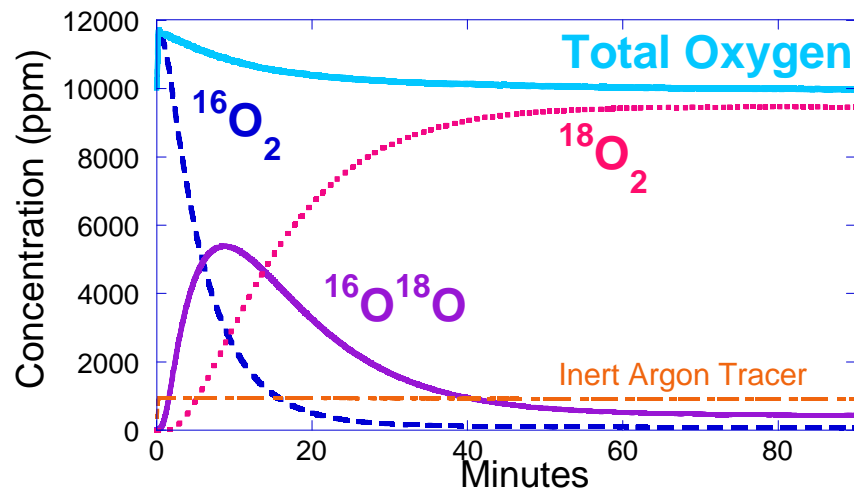


Figure 4-6. Isothermal exchange of LSCF at 650°C and 10,000 ppm O₂ [71]

Applying equation 4-10 to the series of LSCF isotopic exchange, the curve fit shows that the slope (Figure 4-7) is 0.97, indicating a nearly first order dependence on the isotopic oxygen partial pressure at 600°C. This result is consistent with the derived expression (equation 4-1) for dissociative adsorption limited kinetics. The slope at 800°C is 0.91; the small decrease in pO_2

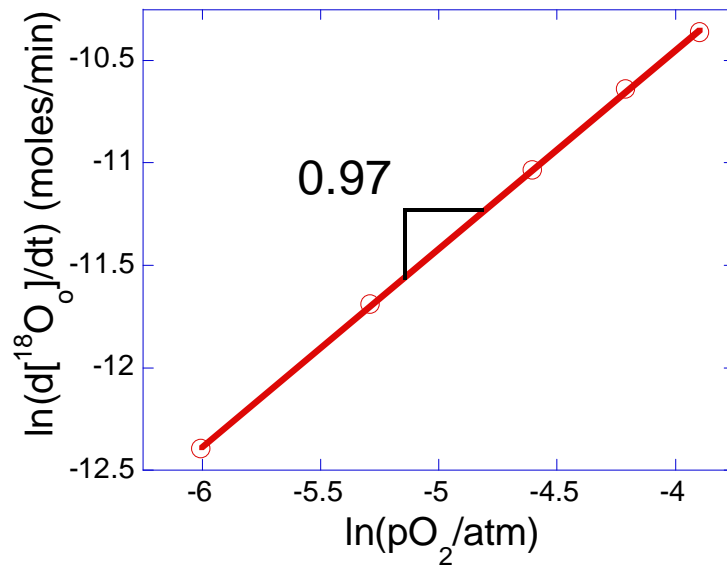


Figure 4-7. Initial rates of exchange vs. oxygen partial pressure for LSCF at 600°C [71] dependence indicates that the reaction is slightly less limited by dissociative adsorption relative to incorporation. The slope is an indication of the mechanism only. The onset temperature of oxygen isotope exchange and the amount of time it takes for a material to exchange a certain amount of oxygen are better indicators of a material's catalytic activity.

Figure 4-8 shows the activation energy for exchange on LSCF between 400 and 700°C. The activation energies for LSCF are much lower than those for LSM. Above 475°C, the activation energy is 0.10 eV, which is very low considering k_bT at 700°C is about 0.08 eV. Below 475°C, it increases to 0.29 eV. From the LSCF TPX (Figure 3-4), below 450°C, LSCF is unable to react with all the $^{18}O_2$ in the environment. The increase in activation energy below

475°C is consistent with the results from the TPX and is thought to occur due to a decrease in vacancy concentration (see trend in Figure 3-3).

An activation energy of 1.09 eV was found from IEDP data above 650°C [80]. Again, the IEDP value is much higher than the activation energy reported here, but both sets of data are consistent with LSM having the higher activation energy. It is unknown if the reason for the

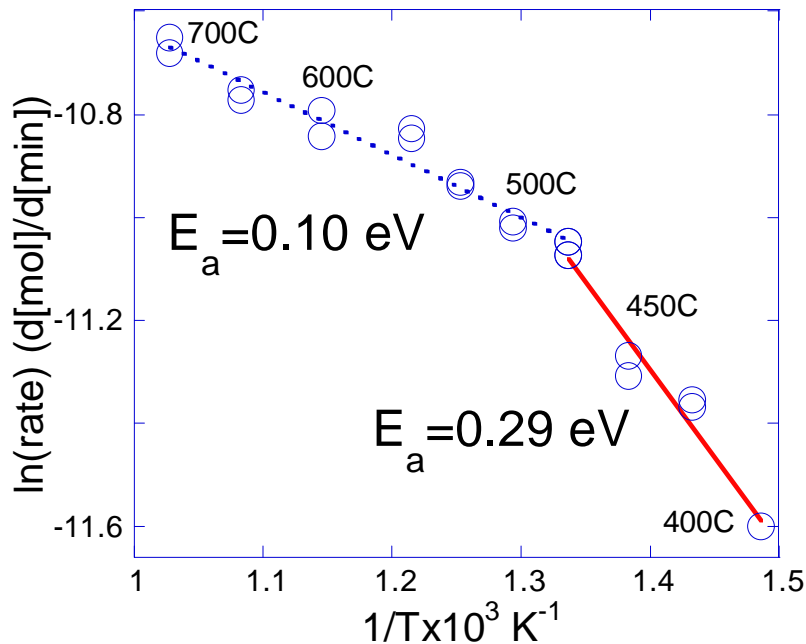


Figure 4-8. Arrhenius plot showing activation energy of oxygen exchange on LSCF under 20,000 ppm $^{18}\text{O}_2$ [71]

large discrepancy is due to trying to compare two fundamentally different rate constants (k_{se} vs. k_1, k_2 , etc) or to the different experimental parameters.

Original IEDP data independent from the work of Benson et al. [81] and Benson [82] could not be found to further compare the activation energy for this particular composition. k_{se} values from conductivity relaxation indicate the apparent activation energy is 1.88 eV [15], but this is quite close to the activation energy of 1.75 ± 0.16 eV for D found by the same method [83]. This, in addition to the observation of an empirical correlation between D and k_{se} [79], indicates

that there may be some difficulty in separating surface and bulk transport processes from each other with the recently mentioned techniques [84].

4.4.3 Trends in LSM and LSCF

Profiles from the switch at 800 °C in 20 sccm of 2% O₂ are shown in Figure 4-9 for LSM and LSCF. Compared to the time scale in the profile from the switch at room temperature

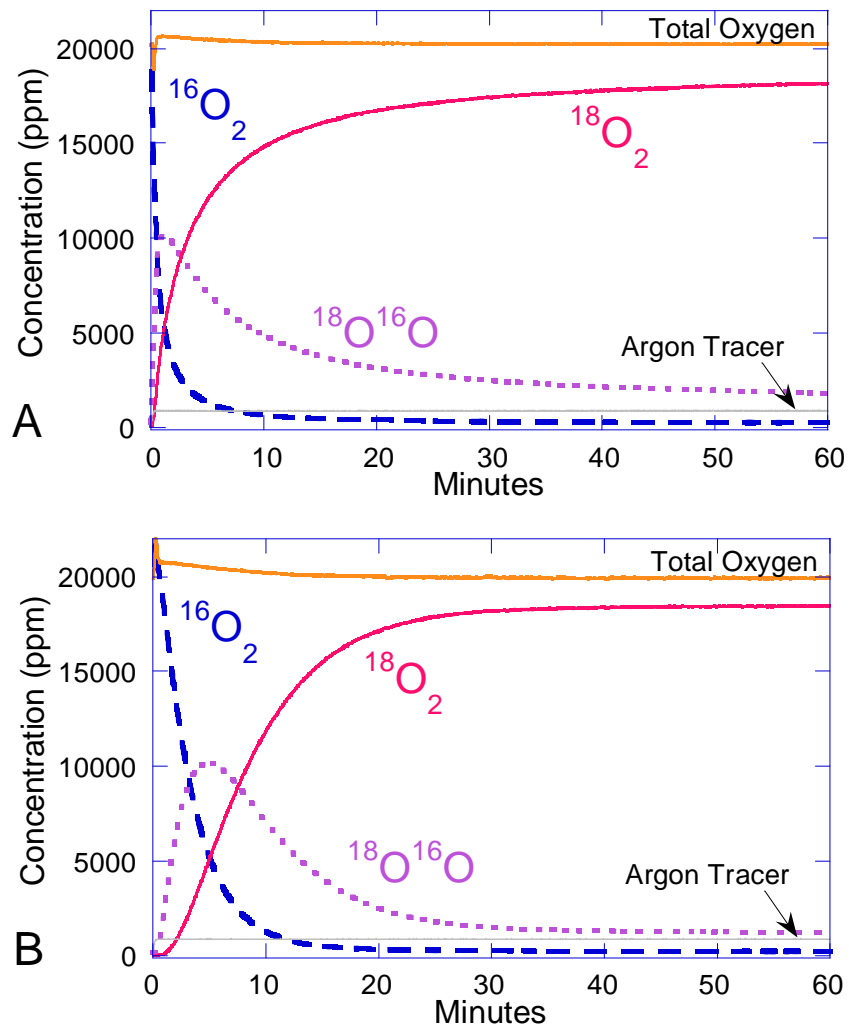


Figure 4-9. Isothermal isotopic switch profile at 800 °C in 20sccm 2% O₂ for A) LSM and B) LSCF

(shown in Figure 4-1), the decay in the $^{16}\text{O}_2$ signal cannot be due to the switch itself and is attributed to the heterogeneous exchange with the ^{16}O containing sample. These profiles show that the total oxygen concentration during the experiment is very stable, with the exception of the discontinuity near the switch (due to pressure imbalance between the two lines). The argon tracer in the effluent also maintains a constant concentration during the exchange. As discussed in the theory section, the time dependent concentration of the gaseous oxygen species ($^{18}\text{O}_2$, $^{16}\text{O}^{18}\text{O}$ and $^{16}\text{O}_2$) reflects changes in the oxygen isotope distribution at the surface. The analysis of these curves can be approached in a variety of ways. The main assumptions made are that any ^{16}O detected above the gas phase baseline from either $^{16}\text{O}_2$ or $^{16}\text{O}^{18}\text{O}$ species originates from the sample and that the total oxygen content of the solid is constant. By integrating the amount of ^{16}O exchanged, as shown in Figure 4-10, and comparing it with the amount expected in the stoichiometric sample, the percentage of the lattice ($1-f_{\text{bulk}}^{16}$) which has been exchanged versus time can be obtained, as shown in Figure 4-11. Under current testing conditions, LSM is

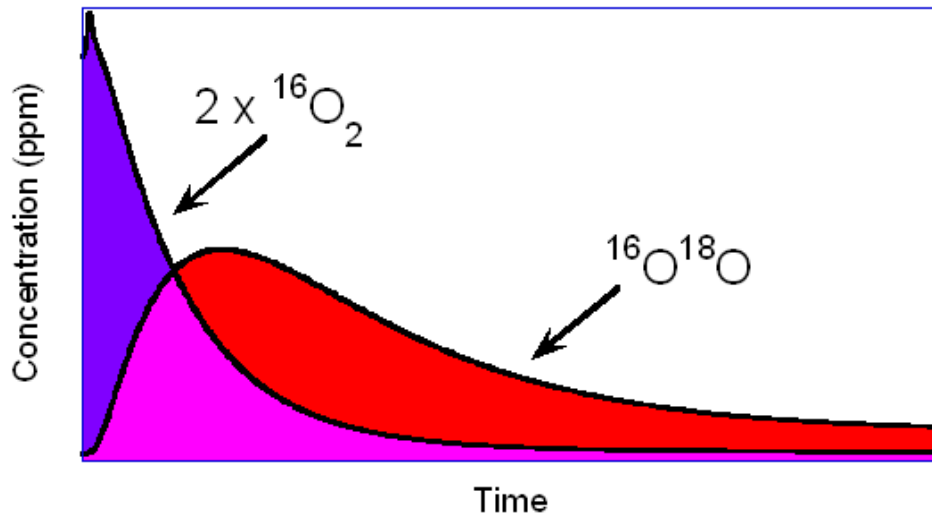


Figure 4-10. Integration of amount of ^{16}O from the gas stream involves counting the $^{16}\text{O}_2$ signal twice and the $^{16}\text{O}^{18}\text{O}$ signal once

insensitive to changes in p_{O_2} (Figure 4-11a) while LSCF is temperature insensitive (Figure 4-11d). Because the rate of exchange is independent of the oxygen partial pressure (a reactant in step 1) and strongly dependent on the temperature of the solid (Figure 4-11c), LSM must be limited by the incorporation step. With regard to LSCF, its behavior is strongly dependent on the oxygen partial pressure (Figure 4-11b), indicating that dissociative adsorption is the rate limiting step. Oxygen is a stable molecule and its dissociation is expected to be highly activated [25,29]. However, the observed temperature insensitive behavior (Figure 4-11d) is strong evidence that the rate limiting step is actually gas phase diffusion of reactants to the sample surface.

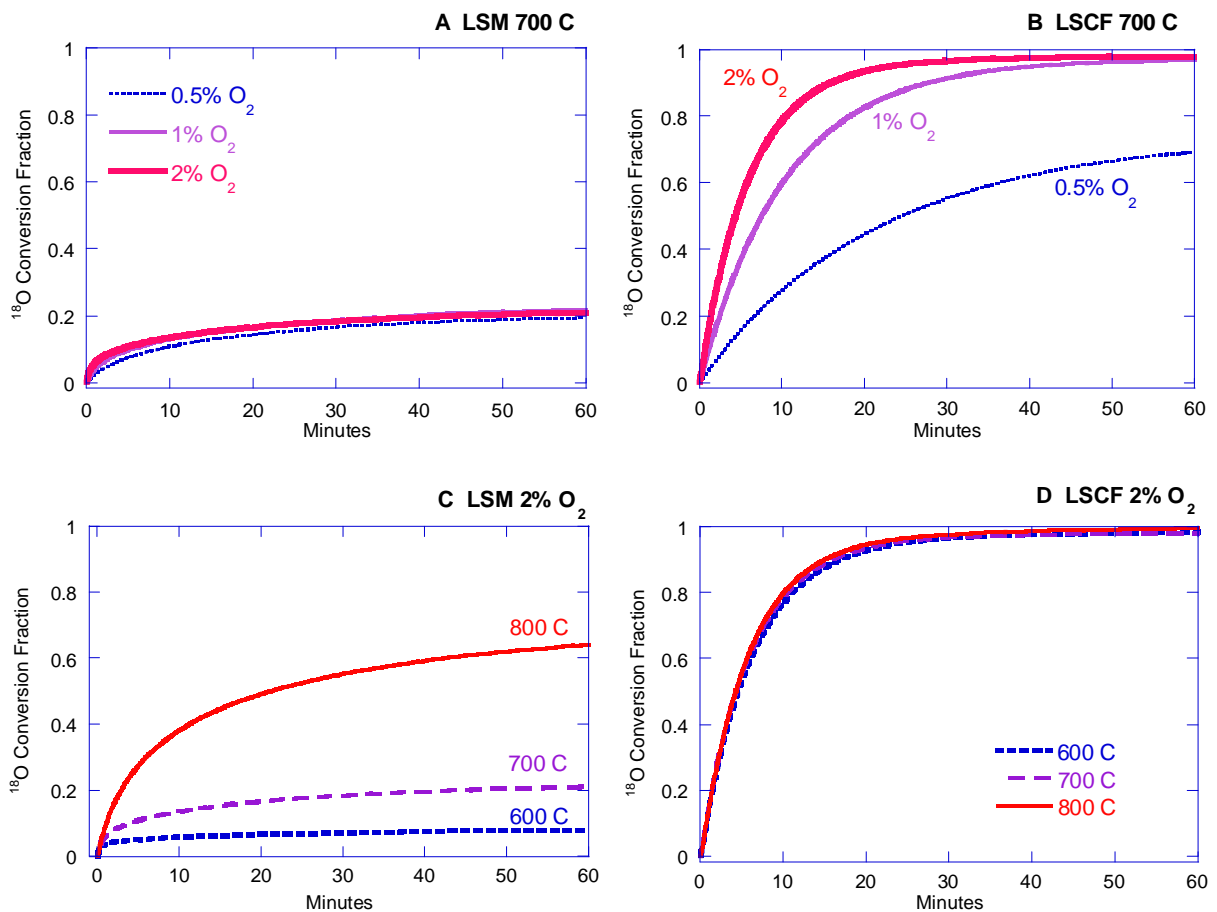


Figure 4-11. Fraction of oxygen in solid converted from ^{16}O to ^{18}O vs. time for A) LSM 700 °C B) LSCF 700 °C C) LSM in 2% O_2 D) LSCF in 2% O_2

Previously, it was noted that LSM has an initial pO_2 dependence of between 0.67 and 0.82, which can also be seen near $t = 0$ in Figure 4-11a. It needs to be emphasized that the overall pO_2 dependence is what is being discussed here, and it appears to be independent of changes in pO_2 . A first order dependence of the total reaction rate on pO_2 , for LSCF, was observed earlier and was initially interpreted as an indication of dissociative adsorption being the rate limiting step [71], but the strong dependence on oxygen concentration (Figure 4-11b) can also arise from gas diffusion limitations since that is also a first order process according to Fick's first law.

The concept of surface reaction and gas phase diffusion limitation is discussed by Fogler in his textbook [85], where the reaction rate is written to include both gas phase diffusion of reactants and the surface reaction. Using Frössling's correlation for mass transfer around a spherical particle, the reaction rate (r_A) is related to the free stream velocity (U) and particle size (d_p), and results in the relationship shown in Figure 4-12. When determining kinetic information

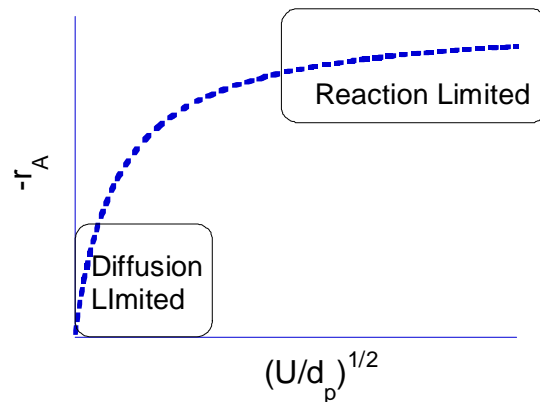


Figure 4-12. Reaction rate versus square root of free stream velocity divided by pellet size; illustrates diffusion limited and reaction limited operating regimes

about a surface reaction, the system should be operating in the reaction limited regime and not in the diffusion limited region. This can be achieved by reducing the particle size (not an option in this study), reducing the reaction rate by reducing temperature, or increasing space velocity. To move LSCF into the reaction limited region, the flow rate was doubled to 40 sccm and then the

isotopic switching experiments were performed again. The range of temperatures examined was extended down to 300 °C. Present equipment limitations prevent testing under conditions with higher flow rates and concentrations.

Figure 4-13a shows the normalized conversion of LSCF under 40 sccm of 1% O₂ and for 20 sccm at 1% O₂ and 700 °C. The sample size for the 40 sccm tests is believed to be slightly larger due to weighing errors and this is taken into account by adjusting the amount of oxygen to which the sample is normalized. The assumption for the 20 sccm set is that each sample contains approximately 2.17×10^{-4} moles of oxygen while the 40 sccm sample contains, and is normalized to, 2.20×10^{-4} moles of oxygen. This is calculated by integrating up to the point at which the number of moles converted reaches a plateau (see Figure 4-11d for example). Two

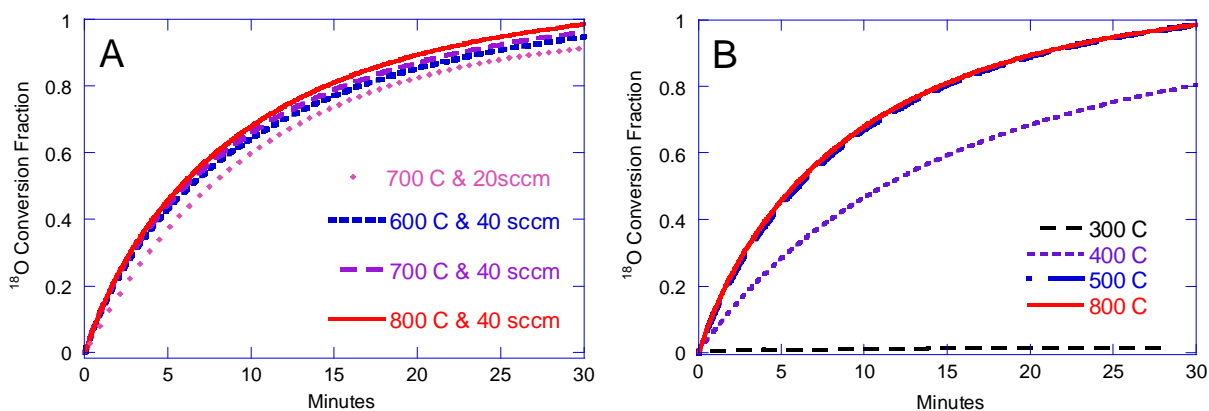


Figure 4-13. Conversion of LSCF in 1% O₂ A) at various temperatures and 2 flow rates and B) at 40 sccm flow rate and lower temperature range

observations indicate that the system is not yet operating completely in the surface reaction limited regime even under 40 sccm flow rate: (1) the rate of reaction is dependent upon the flow rate and (2) the weak dependence on temperature again indicates gas diffusion to be the limiting step. The isotope exchange was performed at lower temperatures to slow down the reaction rate (Figure 4-13b) and it becomes evident that the reaction rate begins to show a temperature dependence between 300 and 500 ° C.

Gas phase profiles from isotopic exchange (1% O₂, 40 sccm) at 300, 400 and 500 °C are shown in Figure 4-14. No reaction is detected at 300 °C; as was also observed at room temperature (Figure 4-1). This is contrary to the TPX profile (Figure 3-4) which does show some exchange occurring around that temperature. The explanation for this is that the sample size is larger and the pO₂ is smaller for more sensitivity in Figure 3-4. It is possible with the higher pO₂ during the isothermal isotopic switching, that the reaction rate is not detectable. The exchange at 500 °C is identical (within error) to that at 800 °C (not shown), and the absence of ¹⁸O₂ in the effluent at the beginning of the switch is evidence that all of the feed stream molecules are impinging upon the sample surface and reacting (100% conversion). The profile obtained at 400 °C possesses characteristics similar to that obtained at both 300 and 500 °C. The discontinuous jump at the beginning of the switch indicates that some of the feed gas does not react on the sample surface. Assuming that the number of active sites remains the same regardless of temperature, it can be inferred that the turnover frequency for each site is reduced by half since only 50% conversion is achieved. By subtracting the non-exchanged baseline from the ¹⁸O₂ signal and halving the scale of the y-axis, the resulting profile (Figure 4-14b inset) once again resembles the behavior observed at higher temperatures. ¹⁶O¹⁸O reaches a maximum when the fractions of ¹⁸O and ¹⁶O on the surface are equal (at ¹⁶f_{ads} = 50%).

The effect of varying the LSCF sample size while holding the temperature, pO₂, and flow rate constants are displayed in Figure 4-15. As expected, the conversion with time is more rapid for smaller samples since there is less oxygen for exchange. Residence time of the gas through the catalyst bed is estimated (from flow rate and LSCF density of 6.39 g/ml) to be at least 3.16 x 10⁻⁷, 6.10 x 10⁻⁷, and 1.11 x 10⁻⁶ seconds for corresponding masses of 4.8, 9.4 and 17.1 mg of LSCF. These masses were back calculated from the amount of oxygen exchanged; due to

weighing errors they are very close but not exactly at the intended sample sizes of 5, 10 and 15 mg.

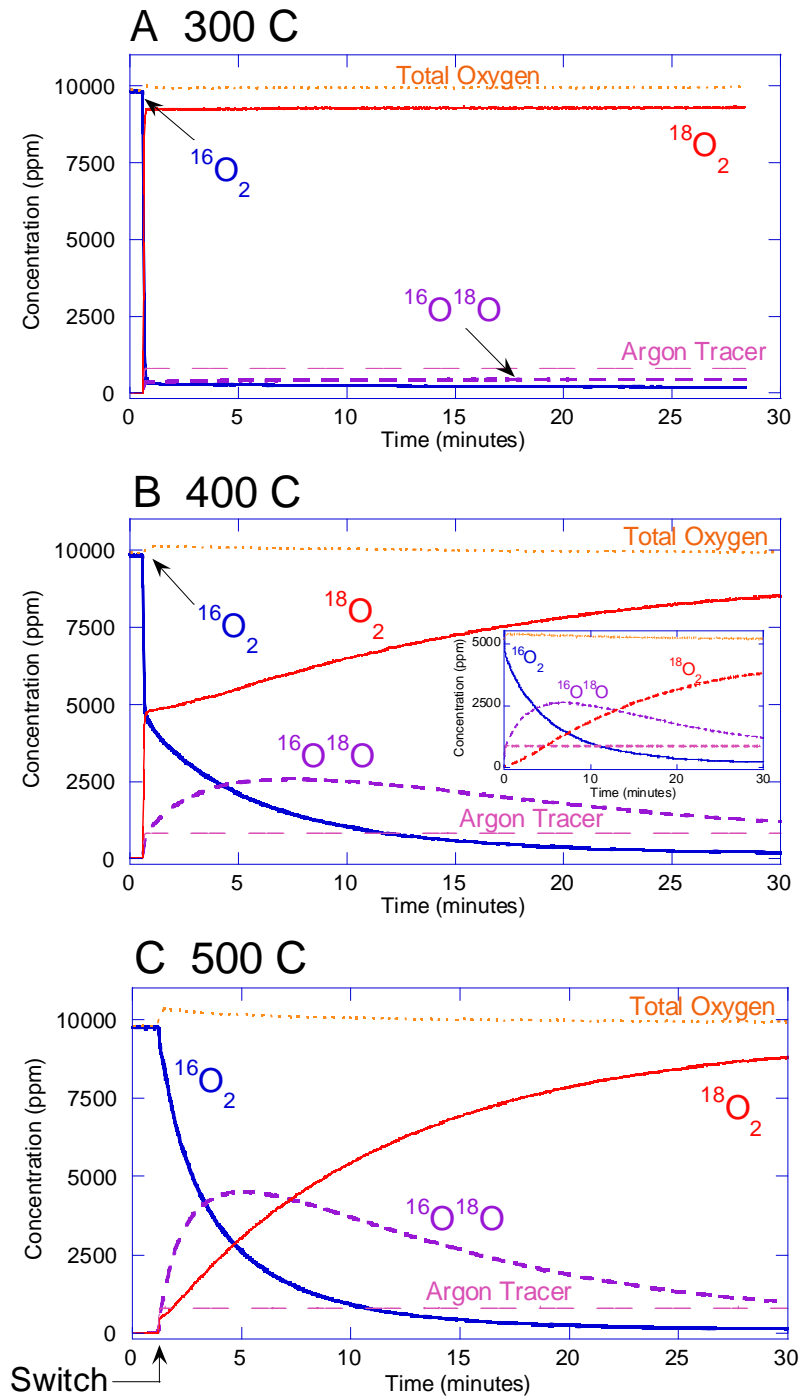


Figure 4-14. Switching profiles for LSCF in 1% O₂ & 40 sccm flow rate at A) 300 °C B) 400 °C [insert shows excess reactant (¹⁸O₂) removed] and C) 500 °C

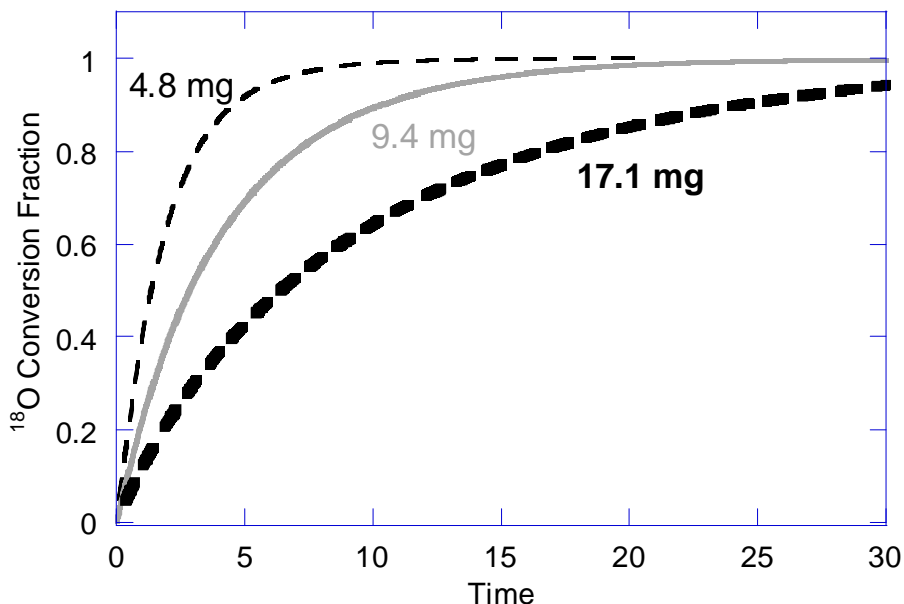


Figure 4-15. Conversion of LSCF vs. Time under 40 sccm of 1% O₂ at 500 °C as a function of sample size

4.4.3.1 Degradation of LSCF

While testing for repeatability, it was noticed that a sample of LSCF began displaying signs of degradation. This is shown for an exchange performed at 500 °C (Figure 4-16). The sample of LSCF which had been cycled many times (~20) showed a discontinuous jump in the initial ¹⁸O₂ and ¹⁶O₂ signal, much like that observed at 400 °C in Figure 4-14b, whereas this was not observed in the fresh sample. The maximum ¹⁶O¹⁸O was smaller in the degraded sample, also indicating that a significant number of oxygen molecules passed through the catalyst bed without participating in exchange. Because the surface is thought to be more active and more defective than the bulk [86], it is not surprising that the powder sample degraded relatively quickly. Also note that the degradation manifests as a reduction in apparent turnover frequency and not as a change in mechanism. This is a strong indication that there are reactive sites on the surface

which have yet to be identified and which become blocked as segregation and other degradation mechanisms start to occur. If a standard is established, then it would be possible to use isotopic exchange to determine if degradation had occurred in a batch of powder.

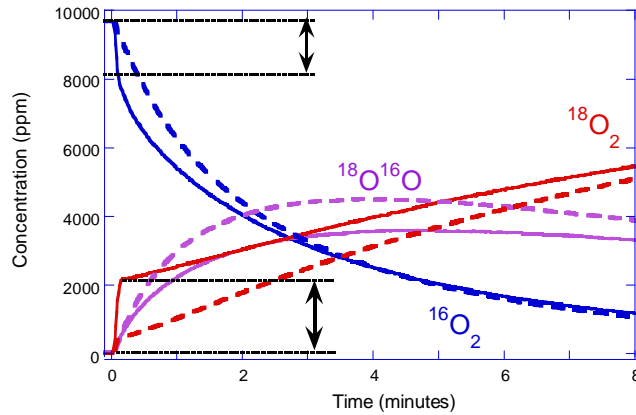


Figure 4-16. Exchange (1% O₂, 40 sccm flow rate, 500 °C) with fresh LSCF (dashed) and LSCF after many cycles (solid)

4.4.4 Gas Phase Behavior Simulation

The behavior predicted by the model for dissociative adsorption limited and incorporation limited scenarios is presented in Figure 4-17 for three values of the surface to bulk oxygen ratio “C”. As discussed in section 4.2, the effective rate constant characteristic of dissociative adsorption is “A”, for incorporation it is “B.” Therefore, by adjusting the relative values of A and B, the behavior of the two limiting cases can be explored. For simulating dissociative adsorption limited reactions (Figure 4-17a), “A” is set to be two orders of magnitude smaller than “B”. With incorporation limited reactions (Figure 4-17b), the opposite is true and “B” is much smaller than “A”. Open symbols represent the surface ¹⁶O fraction (equation 4-8) while solid symbols correspond to the bulk ¹⁶O fraction (equation 4-9). Figure 4-17a shows that the surface and bulk isotope compositions are very similar at any given time for dissociative adsorption limited reactions. This is expected because the first step (of equation 2-8) is rate limiting and the second

step, incorporation, is rapid enough to keep up with the first step. When the relative amount of adsorbed oxygen is small (meaning small “C”), the reaction proceeds very slowly. The larger the

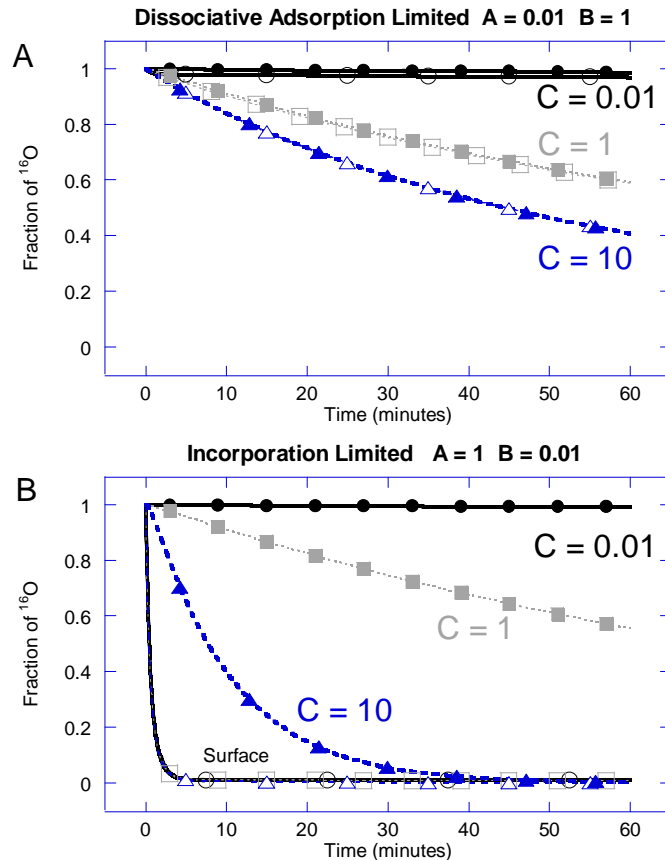


Figure 4-17. Numerical solution for A) Dissociative adsorption limited case with $A = 0.01$ and $B = 1$ while varying “C” B) Incorporation limited case with $A = 1$ and $B = 0.01$ while varying “C”. Open symbols represent surface behavior ($^{16}f_{\text{ads}}$) and solid symbols represent bulk behavior ($^{16}f_{\text{bulk}}$)

value of “C,” the more rapidly the reaction proceeds (toward zero in the case of exchanging ^{16}O for ^{18}O in the sample). In Figure 4-17b, this behavior is not observed; instead, there is a dramatic difference between the isotope composition of the surface and bulk. The surface appears to react in the same manner regardless of the value of “C.” The bulk rate of exchange, however, increases with “C.” From a fundamental perspective, the meaning of “C” is the relative amount of adsorbed oxygen to oxygen in the bulk. If there is very little oxygen on the surface to participate in the incorporation step, then the reaction rate ($=k_2[\text{O}_{\text{ads}}][\text{V}_\text{o}]$) will be very slow, all

other factors remaining equal. Overall, the incorporation limited reaction will appear, based on the surface isotope composition, to have obtained steady state more rapidly than the dissociative adsorption limited case. This incorporation limited surface behavior can be misleading, and requires comprehensive analysis since it is the behavior of the bulk which determines the real extent of reaction.

To model the behavior of LSM under 2% O₂ at 800 °C in 20 sccm flow rate (Figure 4-9a), a Matlab m-file (See Appendix B for code) was written to extract the parameters “A”, “B” and “C” from the time dependent behavior of ¹⁶f_{ads} obtained from the experimental data via equation 4-3. Only the first 30 minutes worth of data was fitted in order to reduce computation time. First, an initial guess for “A”, “B” and “C” is used to generate a numerical solution to equations 4-8 and 4-9 using ODE45, and then the program applies the Gauss-Newton algorithm for least squares fitting of the numerical solution to the ¹⁶f_{ads} data and recalculates the parameters. This process is iterated (150 times to within a tolerance of 5 x 10⁻⁵ %) to ensure the solution converges (Figure 4-18). A good initial guess for “A”, “B” and “C” is required for stability.

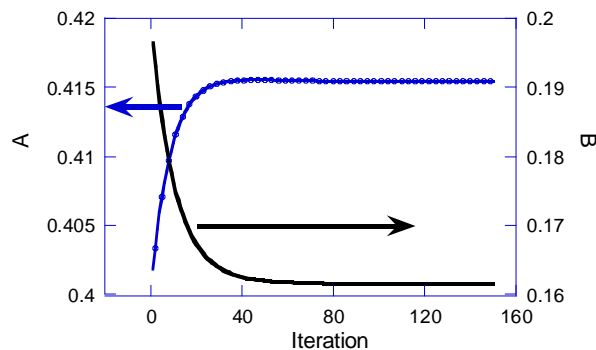


Figure 4-18. Value of parameters A and B as a function of iteration number for LSM at 800 °C under 2% O₂

The resulting profiles for ¹⁶f_{ads} and ¹⁶f_{bulk}, which describe the time varying isotopic composition of adsorbates and lattice oxygen in Figure 2-4, are shown in Figure 4-19 with final parameter values. It is consistent with the incorporation limited behavior in Figure 4-17b. The parameter

values also indicate the rate limiting step is step 2, incorporation. Although the fit for the surface oxygen composition has an R^2 value of 0.995, the bulk model indicates a much higher degree of exchange activity than actually calculated. Taking into consideration LSM's rather low oxygen diffusivity [37,40] it is possible that the assumption made earlier about the oxygen isotopes being well mixed in the solid is not valid. We envision a spherical particle of LSM where only the outermost shell of material initially participates in the exchange reaction and then diffusion of the normal oxygen isotope from the core to the surface constitutes an additional, rate limiting,

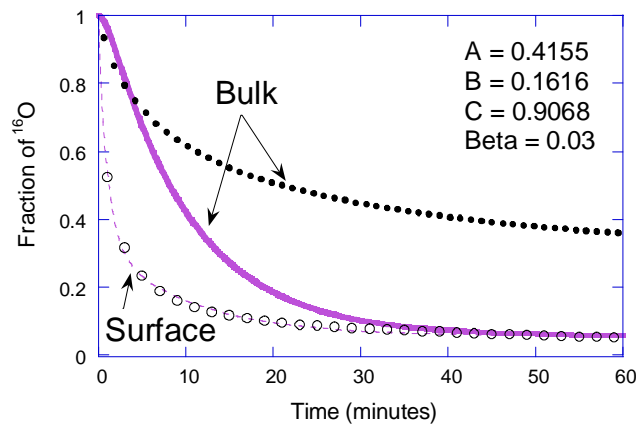


Figure 4-19. Profile of $^{16}f_{\text{ads}}$ (○) and $^{16}f_{\text{bulk}}$ (●) obtained from LSM exchange profile at 800 °C with model (solid lines) superimposed. Final $R^2 = 0.99548$ ($^{16}f_{\text{ads}}$ only).

process. This is consistent with other works which also concluded that bulk diffusion is the slowest step [37,87]. It is possible that the thin outermost shell is well represented by the model; however, we did not verify this. As for the gas phase behavior, Figure 4-20 shows the model superimposed on the normalized exchange data. The fit is very good for $^{18}\text{O}_2$ and $^{16}\text{O}_2$ but overestimates $^{16}\text{O}^{18}\text{O}$. Small changes in the $^{16}\text{O}_2$ data profile and feed gas purity ($2\beta+\gamma$) can result in large deviations in the predicted behavior.

Table 4-1 lists the different exchange parameters produced by the computer fitting program for LSM at 700 °C in 20 sccm flow rate at various oxygen concentrations. Although the model may not completely capture the bulk behavior of LSM, it is important to compare the

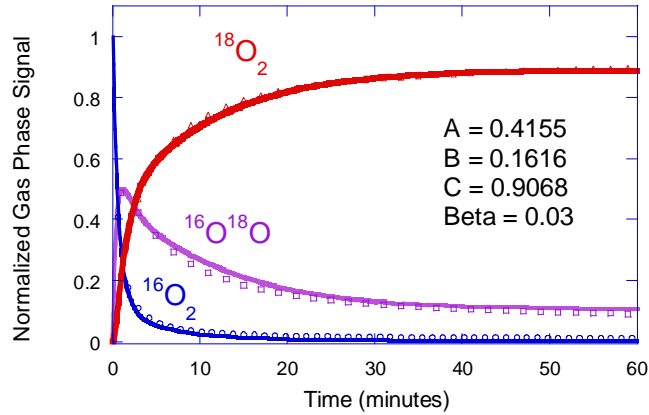


Figure 4-20. Normalized $^{16}\text{O}_2$, $^{18}\text{O}_2$ and $^{16}\text{O}^{18}\text{O}$ signals (open points) and predicted profile from the model (solid lines) for LSM at 800 °C

behavior obtained from the simulation with the isotopic exchange reactions observed earlier in the study. Regarding the concentration of adsorbed to bulk oxygen, “C,” there seems to be a general trend that the value increases with increasing $p\text{O}_2$ or decreasing temperature. This is an expected adsorption behavior. The parameter characteristic of the dissociative adsorption step, “A”, scales proportionally with the oxygen partial pressure. This is not the case for the parameter corresponding to the incorporation step, “B,” and it is also insensitive to the $p\text{O}_2$, as observed in Figure 11a. Since incorporation appears to be rate limiting, the effective rate constant, calculated with an assumed value of the oxygen vacancy concentration, is given in the last column and appears to be constant within the error of the measurement and assumption. Table 2 shows that the effective rate constant is dependent on temperature and corresponds to an activation energy of 6.48 kJ/mole calculated between 700 and 800 °C, and an activation energy of 76.8 kJ/mole from 600-700 °C. The change in activation energy at 700 °C was previously observed; however,

Table 4-1. Exchange parameters obtained from simulation for LSM at 700 °C, 20 sccm flow rate

$p\text{O}_2$	$A = k_{-1}[\text{O}_{\text{ads}}]$	$B = k_2[\text{V}_\text{o}]$	$C = [\text{O}_{\text{ads}}]/[\text{O}_{\text{bulk}}]$	Feed impurity	$[\text{V}_\text{o}] (1/\text{m}^3)\text{§}$	$k_2 (\frac{\text{m}^3}{\text{s}})$
2%	1.381	0.150	1.701	0.03	1.16×10^{22}	1.29×10^{-23}
1%	0.640	0.126	0.940	0.03	1.16×10^{22}	1.08×10^{-23}
0.5%	0.315	0.144	0.779	0.03	1.16×10^{22}	1.24×10^{-23}

§ Value from [37]

Table 4-2. Exchange parameters obtained from simulation for LSM at 2% O₂, 20 sccm flow rate

Temperature (°C)	A = k ₁ [O _{ads}]	B = k ₂ [V _o]	C = [O _{ads}]/[O _{bulk}]	Feed impurity	[V _o] (1/m ³)§	k ₂ ($\frac{m^3}{s}$)
600	2.157	0.050	7.174	0.03	1.16 x 10 ²²	4.35 x 10 ⁻²⁴
700	1.381	0.150	1.701	0.03	1.16 x 10 ²²	1.29 x 10 ⁻²³
800	0.416	0.162	0.907	0.03	1.16 x 10 ²²	1.39 x 10 ⁻²³

the activation energy decreases with increasing temperature and is opposite to what was previously calculated using a different analysis technique consisting of using the initial slope of the overall reaction rate [71]. Previously, the smaller activation energy below 700 °C was attributed to the possibility that the initial reaction rate calculation was only taking into account the more facile exchange of adsorbed species on the surface without exchange with the bulk oxygen [71]. Now, using the simulation and parameter fitting method in this study, we can better capture the real behavior of LSM, where exchange with the bulk is more highly activated at lower temperatures.

These calculated values are all lower than that reported by De Souza et al, who obtained an activation energy for the surface exchange coefficient (k_s^{*}) of 128±21 kJ/mole from the isotope exchange depth profile (IEDP) method performed in the temperature range of 700-1000 °C [40]. This could be due to exchange between the powder and gas being much more facile than exchange with a dense IEDP solid sample. It is not known if these values are directly comparable or if it is more like comparing apples to squares. One represents a mass transfer coefficient (k_s^{*}), while the values presented here are mechanistic rate constants with unique units as defined by equation 2-8.

When modeling LSCF, the program would often become unstable due to the value of B continuously growing unbounded. To stabilize the computation, the program was only permitted to fit the value of A and C over 150 iterations to a tolerance of 5 x 10⁻⁶ % (Figure 4-21). Figure 4-22 shows the data with superimposed model as a function of time. The experimental data

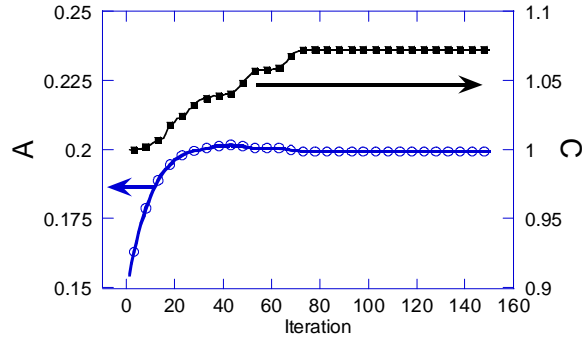


Figure 4-21. Value of parameters A and C as a function of iteration number for LSCF at 800 °C under 2% O₂.

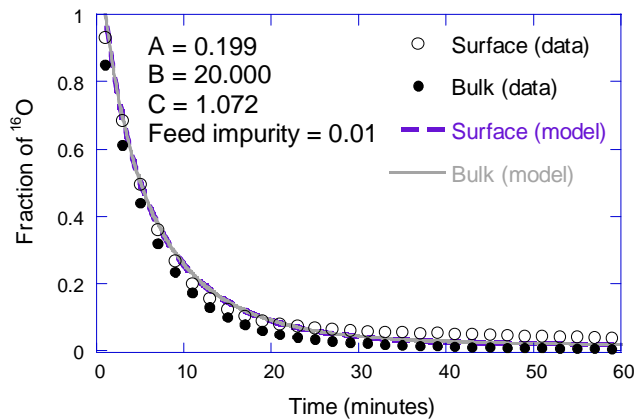


Figure 4-22. Profile of $^{16}f_{\text{ads}}$ (○) and $^{16}f_{\text{bulk}}$ (●) obtained from LSCF 2% O₂ exchange profile at 800 °C, with model (lines) superimposed. Final $R^2 = 0.995$ ($^{16}f_{\text{ads}}$ only).

indicates that the oxygen isotope composition at the surface and in the bulk mirror each other closely, which is consistent with a very fast incorporation step (large “B”). The bulk model follows the surface model, which has a correlation of $R^2 = 0.995$ with the surface data. $(2\beta+\gamma)$, the fraction of ^{16}O in the isotopically labeled stream, for LSCF is smaller than that for LSM because the source of isotopic oxygen was changed during the course of this study with one of a slightly higher purity. The gas phase profile (Figure 4-23) shows that the model can also predict the behavior of LSCF fairly well. To illustrate the system reciprocity referenced in section 4.2, the same exchange behavior was fitted using the $^{18}f_{\text{ads}}$ data rather than $^{16}f_{\text{ads}}$; results are presented in Figure 4-24. The gas feed impurity is no longer the ^{16}O in the feed stream but rather ^{18}O .

Notice that the values of A and C (B is again held constant), are similar to those obtained by fitting $^{16}\text{f}_{\text{ads}}$. The R^2 value is slightly lower at 0.988 versus 0.995 when $^{16}\text{f}_{\text{ads}}$ is used. Because of this, we have greater confidence using $^{16}\text{f}_{\text{ads}}$ to fit the data, although theoretically it should not matter. We acknowledge there could be errors in the calibration of the labeled oxygen signal and therefore prefer to use the directly calibrated oxygen signal for analysis.

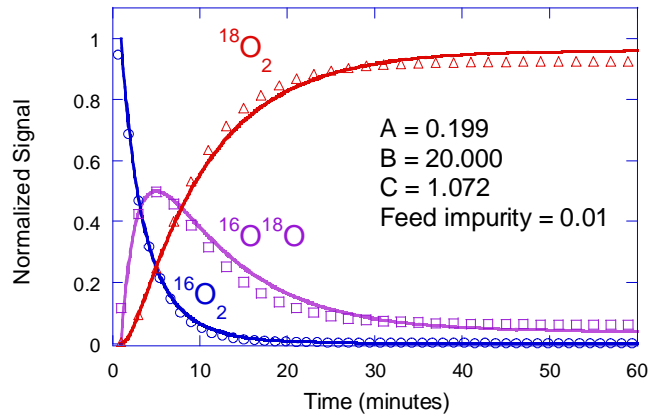


Figure 4-23. Normalized $^{16}\text{O}_2$, $^{18}\text{O}_2$ and $^{16}\text{O}^{18}\text{O}$ data (open points) and predicted profile from the model (solid lines) for LSCF 2% O_2 at 800 °C

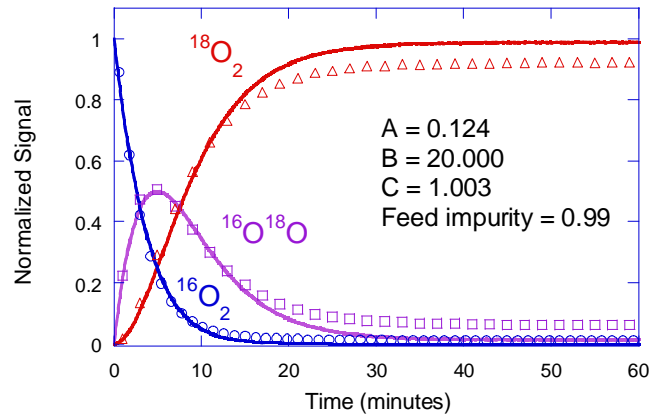


Figure 4-24. Normalized $^{16}\text{O}_2$, $^{18}\text{O}_2$ and $^{16}\text{O}^{18}\text{O}$ data (open points) and predicted profile from the model (solid lines) for LSCF 2% O_2 at 800 °C, calculated by fitting the $^{18}\text{f}_{\text{ads}}$ data instead of the $^{16}\text{f}_{\text{ads}}$ data. $R^2 = 0.988$

Alternatively, a simplification was made to require only one parameter, “A,” be estimated to solve for the time dependent behavior for LSCF and then, with various assumptions, the effective rate constant was calculated under different scenarios. The simplification is simply to set $^{16}f_{\text{bulk}} = ^{16}f_{\text{ads}}$ since the bulk follows the surface closely, and upon insertion into equation 4-8, the second term drops out. This leaves only “A”, and does not require any guessing of B and C values. Results are given in Table 4-3 and Table 4-4 for 15 mg sample size in all cases. Table 4-5 shows the variation with LSCF sample size at 500 °C. The surface coverage is estimated from the 400 °C profile (Figure 4-14b) by setting the maximum rate of production equal to the amount of oxygen exchanged at the “knee” of the figure, representing the oxygen which is actually exchanging and not that just due to the switch. This number is approximately 4734 ppm of O₂ exchanged initially when $^{16}f_{\text{ads}}=1$. From the concentration, sample size and flow rate, the moles

Table 4-3. Exchange parameters for LSCF at 700 °C, 20 sccm total flow rate at various pO₂

pO ₂	$A \left(\frac{\mu\text{mole O}_2}{\mu\text{mole O}} \frac{1}{s} \right) = k_{-1}[\text{O}_{\text{ads}}]$	Feed impurity	[O _{ads}] (μmole O/m ²)	$k_1 = A[\text{O}_{\text{ads}}]/p\text{O}_2$ $\left(\frac{\mu\text{mole O}_2 \cdot \text{atm}}{s \cdot \text{m}^2} \right)$
2%	0.217	0.01	11.3	123
1%	0.125	0.01	11.3	141
0.5%	0.059	0.01	11.3	133

Table 4-4. Exchange parameters for LSCF at 1% O₂ 40 sccm at 400-500 °C

Temperature (°C)	$A \left(\frac{\mu\text{mole O}_2}{\mu\text{mole O}} \frac{1}{s} \right) = k_{-1}[\text{O}_{\text{ads}}]$	Feed impurity	[O _{ads}] (μmole O/m ²)	$k_1 = A[\text{O}_{\text{ads}}]/p\text{O}_2$ $\left(\frac{\mu\text{mole O}_2 \cdot \text{atm}}{s \cdot \text{m}^2} \right)$
500 (100% Conversion)	0.247	0.01	11.3	278
400 (47% Conversion)	0.114	0.01	11.3	128

Table 4-5. Exchange parameters for varying sample sizes of LSCF (1% O₂, 40 sccm, 500 °C)

Sample Weight (mg)	$A \left(\frac{\mu\text{mole O}_2}{\mu\text{mole O}} \frac{1}{s} \right) = k_{-1}[\text{O}_{\text{ads}}]$	Total Surface Area (m ²)	Feed impurity	[O _{ads}] (μmole O/m ²)	$k_1 = A[\text{O}_{\text{ads}}]/p\text{O}_2$ $\left(\frac{\mu\text{mole O}_2 \cdot \text{atm}}{s \cdot \text{m}^2} \right)$	Total Rate SA x k ₁ x pO ₂ (μmole O ₂ /s)
4.8	0.566	0.03	0.01	11.3	639	0.19
9.4	0.329	0.06	0.01	11.3	371	0.22
17.1	0.240	0.11	0.01	11.3	270	0.30

of oxygen reacted per unit area can be estimated. Setting this equal to the expression in equation 4-3 and using the fitted parameter for “A,” the concentration of O_{ads} can be back-calculated. The value of $11.3 \mu\text{mole O/m}^2$ obtained is reasonable when compared to the value of $4 \mu\text{mole O}_2/\text{m}^2 \approx 8 \mu\text{mole O/m}^2$ used in earlier analysis by Teraoka [17] and $13.7 \mu\text{mole O}_2/\text{m}^2$ used by Joly [88]. Using the assumption that the overall oxygen exchange reaction is in equilibrium, the value of the rate constant k_1 is calculated from parameter “A” using equation A6 in the appendix (the concentration of surface sites is ignored due to lack of information).

Table 4-3 shows a direct relationship between the parameter “A” and the oxygen partial pressure. However, the resulting calculated rate constant k_1 is essentially unaffected by the partial pressure after dividing by the pO_2 . This is to be expected for a mechanistic rate constant, which should not be pO_2 dependent and is thus in contrast to surface exchange coefficients obtained by conductivity relaxation or IEDP methods [14,15,36,40,57]. The A value for LSCF under 20 sccm flow rate at $800 \text{ }^\circ\text{C}$ is calculated to be 0.199 (Figure 4-23) when computed with both B and C values. “A” is calculated to be 0.217 for LSCF at $700 \text{ }^\circ\text{C}$ when the approximation is made and only “A” is fitted (Table 4-3). As indicated previously in Figure 4-11d, the rate of oxygen exchange with LSCF is essentially temperature independent above $600 \text{ }^\circ\text{C}$ in the pO_2 range investigated, so there is no difference in the profiles at $700 \text{ }^\circ\text{C}$ and $800 \text{ }^\circ\text{C}$. The similarity of these results shows the validity of the approximation.

Table 4-4 shows that the value of “A” has a strong dependence on the temperature between $400\text{-}500 \text{ }^\circ\text{C}$, in agreement with behavior seen in Figure 4-13b and in Figure 4-14b. Note that the conversion in 5-14b is approximately 47%; the fact that $k_1 = 128$ at $400 \text{ }^\circ\text{C}$ is very close to $47\% \times (k_1 \text{ at } 500^\circ\text{C}) = 131$ (Table 4-4), seems more than coincidence. The calculated activation energy

of k_1 is 33.6 kJ/mole, again much lower than that reported for the surface exchange coefficient from IEDP in this temperature range of 105.1 kJ/mole [80].

Table 4-5 contains the dissociative adsorption parameter, “A”, for three different sample sizes of LSCF at 1%O₂ and 40 sccm, 500 °C. Without taking into account the sample size, the smaller sample will appear to react more rapidly (k_1) since there is less oxygen in the sample available for exchange. When the surface area is factored in to produce the total rate, the total rate is proportional to the sample surface area, as shown in the last column. As the surface area increases, the total amount of oxygen exchange increases, which supports previous findings that higher cathode surface area is beneficial for SOFC performance [89].

Our present equipment configuration prevents testing under higher flow rates and concentrations; however there is much potential to continue this work with other cathode materials. Isotopic exchange is sufficient for determining which of the two steps discussed is rate limiting, but the reality is that the oxygen reduction reaction is accompanied by charge transfer as well. The two steps can be further divided into steps containing a net transfer of two electrons for every oxygen which is reacted at the cathode. This presents the need to combine this method with additional electrical measurements to truly understand all the processes occurring on the surface.

4.5 Conclusion

Several oxygen surface exchange characteristics for LSM and LSCF were determined from the isothermal isotopic switching technique as interpreted by behavior predicted from a two step model consisting of dissociative adsorption of an oxygen molecule followed by incorporation into the solid.

From the initial reaction rate dependence on pO₂, the rate limiting step in LSCF, as given by the derivation, is dissociative adsorption between 600 and 800°C. In the case of LSM, both

steps are significant at 600 and 800°C. The activation energy for LSM (0.90 eV above 700°C) is significantly higher than that of LSCF (0.10 eV above 475°C) at all temperatures tested. An activation energy of 0.41 eV was measured for LSM below 650 °C. This lower value is interpreted as the activation energy for oxygen dissociation on the surface, step 1 of the reaction only, and suggests that there is a large barrier to oxygen diffusion through the LSM bulk. It is therefore advisable to operate SOFCs with LSM cathodes at temperatures no lower than 700°C so that some oxygen diffusion through the bulk can take place. For SOFCs with LSCF cathodes, the lower limit to the operating temperature should be 500°C since below that limit, the activation energy increases to 0.29 eV and incorporation becomes more difficult.

The time dependent conversion of the sample oxygen lattice from ^{16}O to ^{18}O , under testing conditions, is insensitive to $p\text{O}_2$ for LSM and strongly dependent on temperature indicating incorporation limitations. In contrast, LSCF is strongly dependent on $p\text{O}_2$ and insensitive to temperature. After doubling the flow rate and re-examining LSCF, it was concluded that LSCF was not exclusively limited by the surface reaction but also somewhat by gas phase diffusion.

Computer simulations of the dissociative adsorption limited and incorporation limited scenarios predicted that the time dependent isotopic distribution of the bulk and surface atomic oxygen would follow different behaviors. In the case that dissociative adsorption was limiting, the surface and bulk conversion from $^{16}\text{O}_{\text{ads}}$ to $^{18}\text{O}_{\text{ads}}$ would be nearly identical. When incorporation is rate limiting, the surface appears to reach steady state far more quickly than the bulk. The rate of conversion of the bulk does not appear to affect the surface behavior in the incorporation limited scenario.

Another program was used to extract kinetic parameters from the surface oxygen isotope composition profile and simulate gas phase profiles. The fit for LSM was good with regard to the

surface composition, but did not adequately model the overall bulk behavior. It is therefore likely that LSM is not limited by the surface reaction but rather by diffusion through the solid. There is no consideration for diffusion from the core to the surface in the model, which could explain why it did not fully describe the exchange kinetics of LSM.

The model considered in this study does a good job capturing the behavior of the LSCF exchange reaction. The isotopic composition of the surface and bulk mirror each other closely, in agreement with a relatively fast incorporation step. A rate constant for dissociative adsorption, the rate limiting step, was obtained from fitting the data to the model. After adjusting for sample mass, the overall reaction rate was found to be proportional to surface area.

This technique was also used to detect degradation in a sample of LSCF which had been subjected to multiple switching cycles. The reactivity of the cycled sample was significantly less than that of a fresh sample. By establishing a standard, isotopic methods can be used to easily and quickly detect degradation in powders.

Now that a comprehensive framework has been provided for interpreting the mechanism of oxygen surface exchange, the next step is to study how properties of the surface affect catalytic activity. This is the focus of the next chapter, where infiltrated samples of LSM and LSCF are produced and compared using isotopic exchange.

CHAPTER 5 IDENTIFYING TRENDS IN CATALYTIC ACTIVITY WITH SYSTEMATIC SURFACE MODIFICATION

5.1 Introduction

With the goal of developing better intermediate temperature solid oxide fuel cells (SOFC), the principal focus of SOFC research has been on improving the functionality of the cathode component. $(\text{La}_{0.8}\text{Sr}_{0.2})_{0.98}\text{MnO}_{3\pm\delta}$ (LSM) and $\text{La}_{0.6}\text{Sr}_{0.4}\text{Co}_{0.2}\text{Fe}_{0.8}\text{O}_{3-\delta}$ (LSCF) are two high performing and well studied SOFC cathode materials [10,47,90-94]. Both materials belong to the perovskite family and are commercially available, however there is one major difference between the two: LSM is primarily an electronic conductor whereas LSCF is a mixed ionic-electronic conductor (MIEC). In the previous chapters [71], isotopically labeled oxygen exchange was used to show that LSM is not as catalytically active as LSCF. Other studies have also shown that SOFCs with LSCF cathodes outperform those with LSM (and even LSM-YSZ composite cathodes) at intermediate temperatures [48,95]. However, LSM fares better in terms of long term stability [10,95,96], which is why it remains favored by industry.

In order to combine the best attributes of both materials into one cathode, this chapter focuses on the surface modification of a stable LSM base material. The idea of surface modification has been previously studied [5,97,98] for an actual cathode on a SOFC button cell; these studies focused on the apparent overall electrochemical performance. In contrast, this study focuses only on the catalytic properties of the cathode material to isolate the effect of surface modification. First the most catalytically active surface component of LSCF needs to be isolated by systematically studying how each constituent affects surface reactivity. Therefore, after depositing La, Sr, Co or Fe oxide onto the surface of LSM powder, temperature programmed isotope exchange (TPX) experiments [71] were performed to test for any changes in catalytic activity toward oxygen exchange. These experiments involve linearly heating the material in an

isotopically labeled oxygen stream while monitoring changes in signal from the different oxygen isotopologues $^{16}\text{O}_2$, $^{16}\text{O}^{18}\text{O}$ and $^{18}\text{O}_2$.

Because of the large regular oxygen background in the materials of interest, the use of isotopically labeled oxygen is required to distinguish between oxygen originating within the oxide lattice and that from the feed stream. Without using heavy oxygen, only the total oxidation or reduction behavior of these oxides can be observed [19,20,99]. The use of isotopically labeled oxygen in the gas phase adds an additional dimension to the reaction and makes the interaction between gas and solid much more transparent.

5.2 Experimental

5.2.1 Materials

Unmodified LSM (Nextech), LSCF (Praxair) and Co_3O_4 powder (Alfa Aesar) were used as reference materials. To make the infiltrated powders, five different metal nitrate solutions were first made by combining metal nitrate salts with deionized water. The metal nitrates used were lanthanum, strontium, cobalt, iron (Spectrum Chemicals) and manganese (Sigma Chemicals). Solution concentrations were verified using inductively coupled plasma spectroscopy. For each infiltrated sample, a few grams of LSM powder (or LSCF for manganese infiltration) was weighed out and combined with enough metal nitrate solution to produce 5 wt% metals loading. The mixture was ultrasonicated for a few minutes and then dried on a hot plate for several hours. The dried material was then calcined at 800°C for 2 hours in air and then hand ground to break up agglomerates. Additional infiltrated samples with 10 wt% and 20 wt% cobalt were created in the same manner.

5.2.2 Powder Characterization

Brunauer-Emmett-Teller (BET) surface area analysis was performed on the resulting powders using a Quantachrome NOVA 1200. X-ray diffraction (XRD, Philips APD 3720) and x-

ray photoelectron spectroscopy (XPS, Perkin-Elmer PHI 5100 ESCA, Photon Energy = 1253.6eV) were used to investigate phase purity and surface composition of the impregnated powders. XPS samples were made by mixing the powders in methanol and depositing the mixture onto 1 cm x 1.5 cm silicon pieces. Spectra were taken after drying and also after heating the samples at 300 °C in air for a couple hours to remove adsorbates. Each spectra was the result of 20 or more individual scans. Transmission electron microscopy (TEM) coupled with energy dispersive X-ray spectroscopy (EDS) and diffraction were employed to further characterize the particles on the LSM or LSCF base material. Particle morphology was captured with SEM.

5.2.3 Catalysis System Configuration

Additional information regarding the experimental setup can be found in Chapter 3 and elsewhere [71]. A schematic of the micro-reactor (Figure 3-2) within the custom built furnace shows the powder sample resting on quartz frit with the thermocouple touching the sample. The feed stream, containing a mix of oxygen and helium, flows over the powder and exits the reactor base to be sampled by the mass spectrometer.

5.2.4 Temperature Programmed Isotopic Exchange

Using surface areas obtained from BET, each temperature programmed exchange (TPX) sample was weighed to yield a total surface area of 0.2 m². The powder was placed in a quartz micro-reactor and then heated to 800°C under 4% ¹⁶O₂ (balance helium) and allowed to slowly cool to room temperature. Once cooled, a gas mixture of approximately 2,500 ppm ¹⁸O₂ (95%, Cambridge Isotope) balanced in helium was fed into the reactor at a flow rate of 20 cc/minute. Then the temperature was ramped at 30°C/minute as the mass spectrometer recorded the oxygen isotope composition of the effluent from 25°C to 800°C in real time. This was repeated twice for each powder. The calibration of the mass spectrometer signal is done through flowing gases of known composition past the inlet and is described in detail elsewhere (Chapter 3 and [71]).

5.3 Results and Discussion

Table 5-1 shows the results from 6 point BET analysis for each powder. The instrument (Quantachrome NOVA 1200) acquires 6 data points and obtains the surface area from curve fitting ($R^2=0.99$ or greater). It is believed that the resulting infiltrated powders consist of a LSM (or LSCF) base covered in metal oxide particles. While it was straightforward to detect the presence of Fe, Co on LSM and Mn on LSCF using TEM-EDS and XPS, quantifying the additional presence of La or Sr over the background signal presented a challenge. Results from TEM-EDS and TEM diffraction were inconclusive due to the beam spot size and drift from charging of the oxide materials.

Table 5-1. Specific surface areas of infiltrated powders [74]

Material	Specific Surface Area (m ² /gram)
LSCF	6.42
LSM	5.14
LSM + 5 wt% La	3.76
LSM + 5 wt% Sr	3.53
LSM + 5 wt% Co	4.73
LSM + 5 wt% Fe	7.23
LSCF + 5 wt% Mn	6.67
LSM + 10 wt% Co	4.57
LSM + 20 wt% Co	5.00

SEM images of the base LSM and two infiltrated LSM powders are shown in Figure 5-1. There appear to be more small particles on the infiltrated powders than on the plain LSM, but there is no way to tell from the phase contrast if the tiny particles are bits of LSM or the deposited metal oxides. The other infiltrated powders not shown in the figure had similar morphology.

Next, the powders were examined with XRD. The 5 wt% iron and manganese infiltrated powders only showed LSM or LSCF peaks, however strontium, cobalt and lanthanum 5 wt% infiltrated powders showed additional peaks from a second phase. These peaks were small and

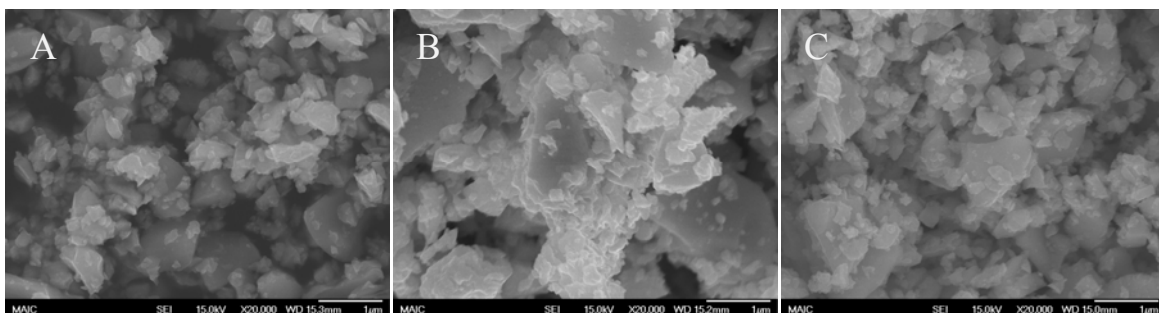


Figure 5-1. Powder morphology captured with SEM, taken at 20,000x A) LSM powder, and LSM infiltrated with B) 5wt% Sr C) 5wt% Co [74]

difficult to distinguish from the background, possibly due to fine dispersion of the deposited particles. In the case of the strontium infiltrated LSM, the presence of β - Sr_2MnO_4 peaks indicate a reaction occurred between the base material and strontium nitrate to create a layered perovskite [100,101] (K_2NiF_4 type) and possibly other secondary phases. As expected, lanthanum infiltrated LSM displayed La_2O_3 peaks from the decomposition of lanthanum nitrate [102]. The 5 and 20 wt% cobalt infiltrated sample showed Co_3O_4 peaks along with the LSM base peaks (Figure 5-2).

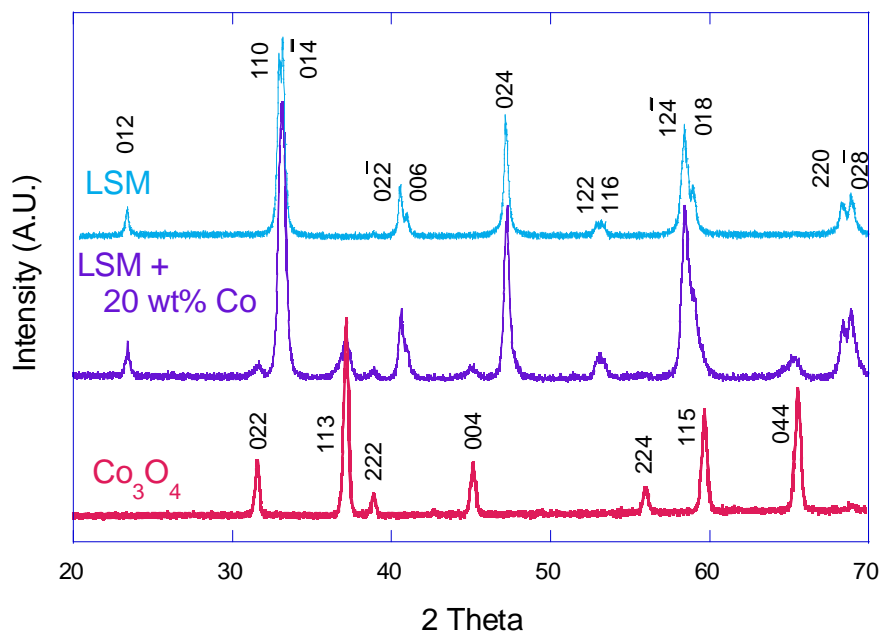


Figure 5-2. Diffraction patterns of LSM, LSM + 20 wt% Co, Co_3O_4 [74]

In order to improve secondary phase detection, 20 wt% iron infiltrated LSM was produced in the same manner as described above and studied using XRD. The 20 wt% iron infiltrated XRD displayed small peaks which looked much like $\alpha\text{-Fe}_2\text{O}_3$, the expected decomposition product from iron nitrate [103]. Twenty wt% manganese infiltrated LSCF was also produced and studied with XRD, but did not produce any detectable secondary peaks.

5.3.1 X-Ray Photoelectron Spectroscopy

The XPS survey for LSM and LSCF is shown in Figure 5-3 with the C 1s reference peak located at 284.8 eV. The expected elements are present in each sample. The profile for the O 1s peak of LSM before and after heating is shown in Figure 5-4. After heating in air at 300 °C, the

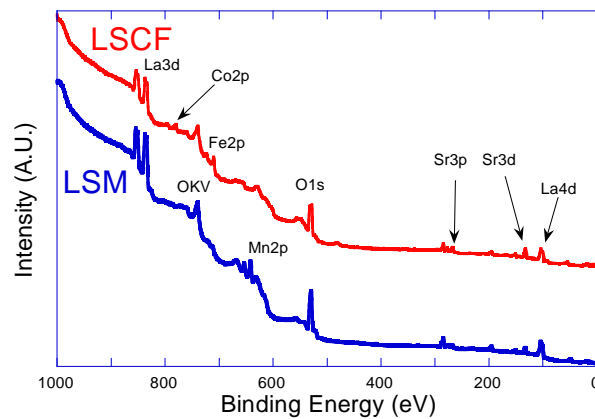


Figure 5-3. Survey spectra (XPS) for LSM and LSCF taken at 45° angle [74]

high energy shoulder at 532.9 eV is greatly reduced; therefore this peak is attributed to surface contamination (probably from water) [104-106]. The peak at 530.9 eV is assigned to either adsorbed surface oxygen species or to oxygen in the lattice with semicovalent character [107,108]. Finally, the low energy peak at 529.0 eV is assigned to oxygen in the lattice with very ionic character [73,106,107,109]. The peak at 530.9 eV is noticeably broader than the peak at 529.0 eV. Yamazoe et al also noticed similar results [73] in a comparable perovskite material ($\text{La}_{1-x}\text{Sr}_x\text{CoO}_3$) and attributed this broadness to the assortment of surface states that are available

to the adsorbed oxygen. Alternatively, in doped perovskites, the coordination of the oxygen ion between different cations can cause polarization in the oxygen's valence shell [107]. For LSM, the A site is statistically occupied by either a La or a Sr and this may be responsible for the broad peak at 530.9 eV. For consistency, XPS profiles after this point are from samples after heating (to remove surface water).

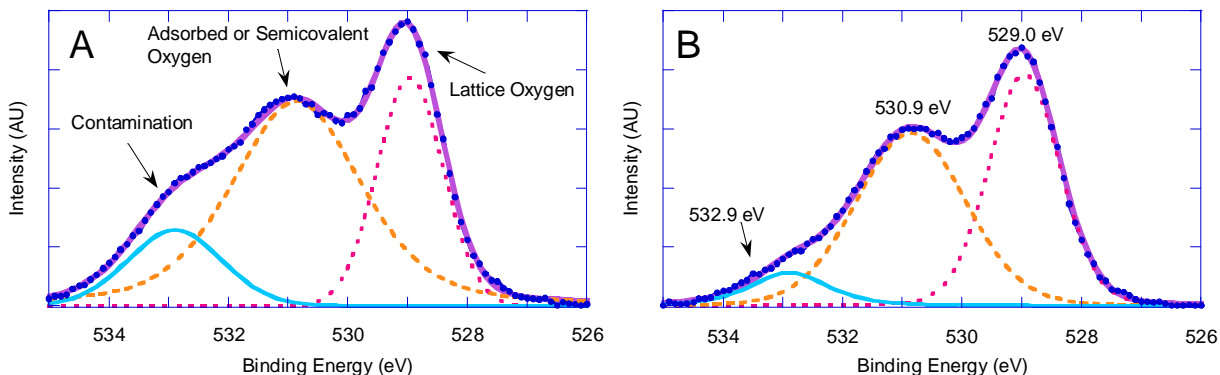


Figure 5-4. $(\text{La}_{0.8}\text{Sr}_{0.2})_{0.98}\text{MnO}_{3\pm\delta}$ O1s peaks A) before heating B) after heating. Data is displayed as points, individual peaks are dashed. The summation of the resolved peaks is displayed as a thin solid line [74]

Normalized spectra for infiltrated LSM samples against the base LSM O1s profile are shown in Figure 5-5. It is apparent that La and Sr infiltration did not change the oxygen surface bonding properties by much, especially for Sr. However, Co and Fe infiltration caused the O1s spectra originally at 529.0 eV to shift to higher binding energies (by approximately 0.37 eV), and

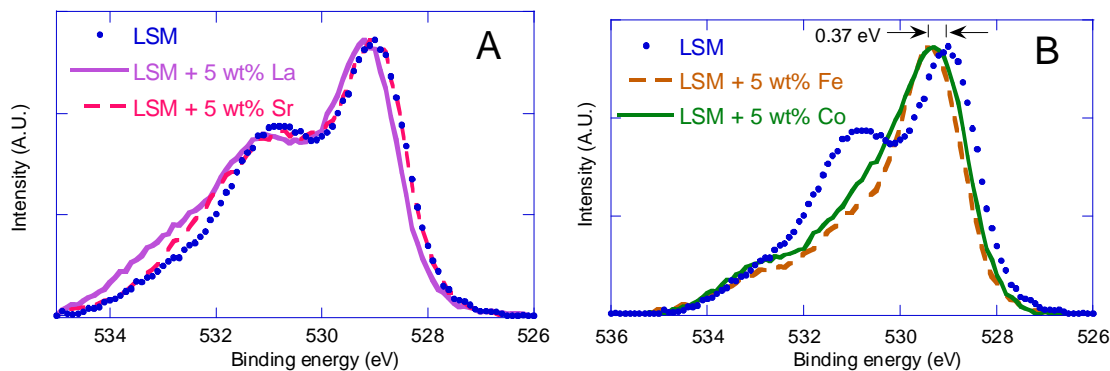


Figure 5-5. O1s spectra for LSM infiltrated with 5 wt% A) La, Sr B) Fe, Co [74]

also reduced the adsorbed oxygen component near 530.9 eV. If the oxygen adsorption sites are assumed to be metal sites, then the latter observation could indicate more open metal sites at the surface relative to the base LSM. A similar comparison is made (Figure 5-6) with the O1s spectra of LSCF and the LSCF + 5 wt% Mn sample. The O1s spectrum is different in that the manganese sample is missing the peak at 532.9 eV and the adsorbed oxygen peak at 531.1 eV is slightly smaller. The peaks at 528.6 eV overlap closely, which indicate that the surface lattice oxygen species are similar in these two samples.

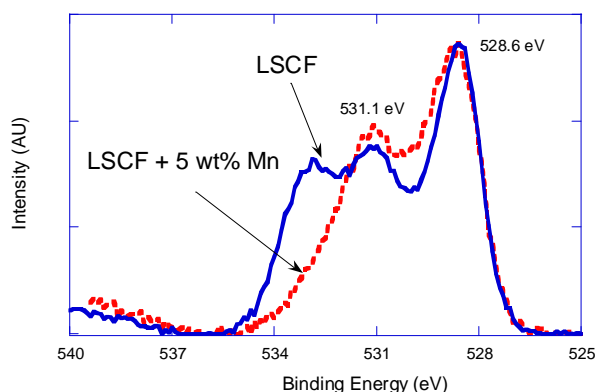


Figure 5-6. O1s spectra for LSCF and LSCF + 5 wt% Mn [74]

Figure 5-7 shows the La $3d_{5/2}$ peaks of the LSM + 5wt% La compared to the base LSM. The similarity in the relative peak intensities and positions indicates that the oxidation state of the La on the surface of the infiltrated material is probably the same as that on the surface of the base material. The 4 eV gap is characteristic of La_2O_3 [110] and is similar to reported spectra [109,111] for the La^{3+} oxidation state. The binding energy of the La $3d_{5/2}$ peaks agrees with values reported from Wu [109] for $\text{La}_{0.5}\text{Sr}_{0.5}\text{MnO}_3$ pellets with a main line at 834.1 eV.

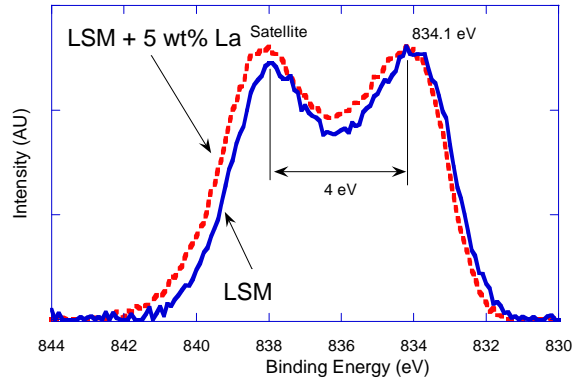


Figure 5-7. La 3d_{5/2} peaks for LSM and LSM + 5 wt% La [74]

Sr 3d peaks for LSM + 5 wt% Sr is shown with those from LSM in Figure 5-7. These two profiles are almost identical, which indicate Sr in the infiltrated sample is comparable in oxidation state to Sr in the base LSM. In this case, the Sr 3d peak separation matches those reported by Wu and Kumigashira [109,112], who studied LSM with differing compositions than the one chosen for this study. They attributed the signal to Sr²⁺ from comparison to similar compounds. A SrO-like peak is observed around 135.4 eV [113], and this is larger in the case of the strontium infiltrated LSM. Very little data on β -Sr₂MnO₄, including XPS work, could be found for comparison.

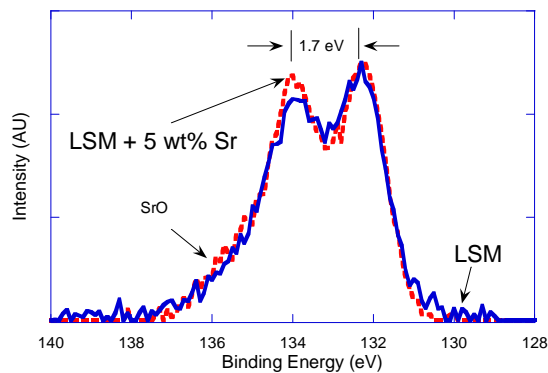


Figure 5-8. Sr 3d peaks for LSM and LSM + 5 wt% Sr [74]

Figure 5-9 shows the comparison between the LSM + 5wt% Co and LSCF XPS Co 2p_{3/2} spectrum. The C1s signals of the two compounds had the same binding energy, so no correction was needed. The binding energy is characteristic of cobalt oxides [114], but since the tabulated

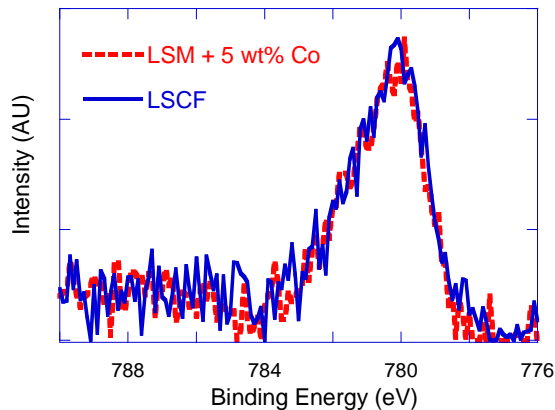


Figure 5-9. Co $2p_{3/2}$ profile of LSM + 5wt% Co and LSCF [74]

values are very close, it is difficult to say exactly which oxide contributed to this signal.

Fortunately, the XRD data have verified that Co_3O_4 is on the surface of the infiltrated LSM and it is deduce that the oxidation state of cobalt at the LSCF surface is mixed. The fact that the spectra overlap perfectly indicates the electronic state of cobalt on the surface of LSM is identical to that of the cobalt at the surface of the LSCF lattice.

Next, Figure 5-10 shows the difference between the Fe $2p_{3/2}$ spectrum of LSM + 5wt% Fe and LSCF. Fujii [115] reported binding energies of 710.7 and 710.9 eV for α and γ Fe_2O_3 , respectively, so it appears the iron infiltrated LSM has Fe^{3+} at the surface. Brundle [116] found that Fe^{3+} and Fe^{2+} could be distinguished using XPS and they had binding energies of approximately 711.2 and 709.7 eV, respectively. The LSCF Fe $2p_{3/2}$ binding energy is significantly different from the infiltrated LSM and fits better with the Fe^{2+} oxidation state.

The Mn $2p_{3/2}$ peak from manganese infiltrated LSCF showed a 0.3 eV shift to higher energy when compared to the $2p_{3/2}$ peak from LSM centered at 641.7 eV. It is difficult to determine the oxidation state from the Mn 2p spectra because the peaks for several manganese oxide compounds have very similar binding energies.

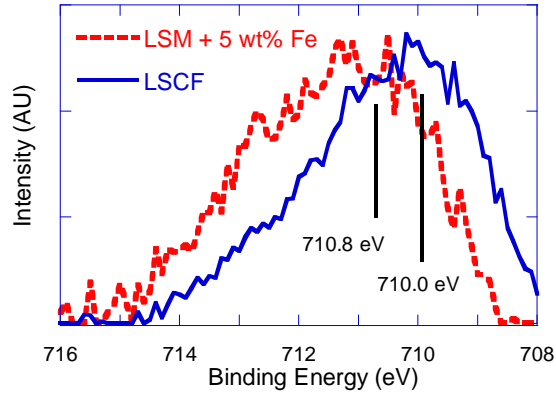
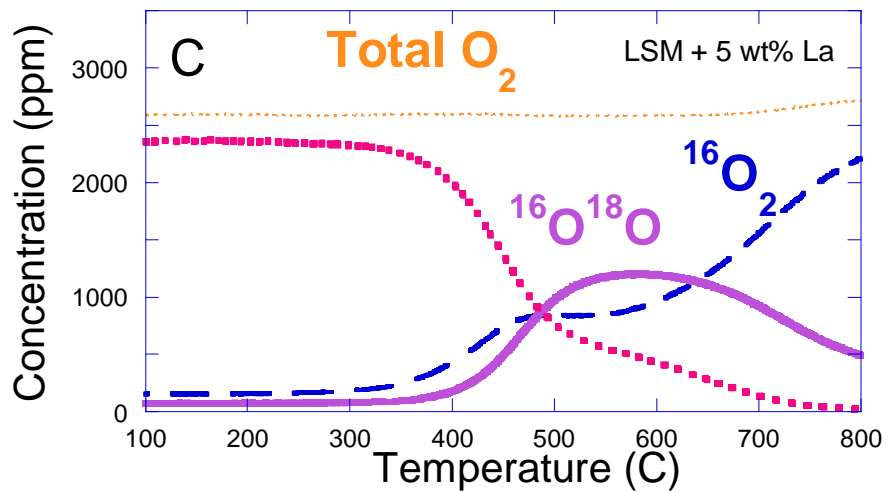
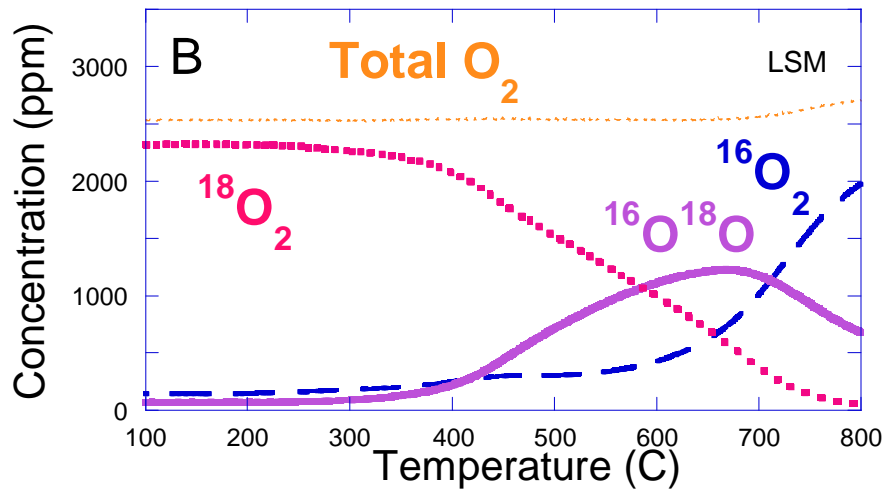
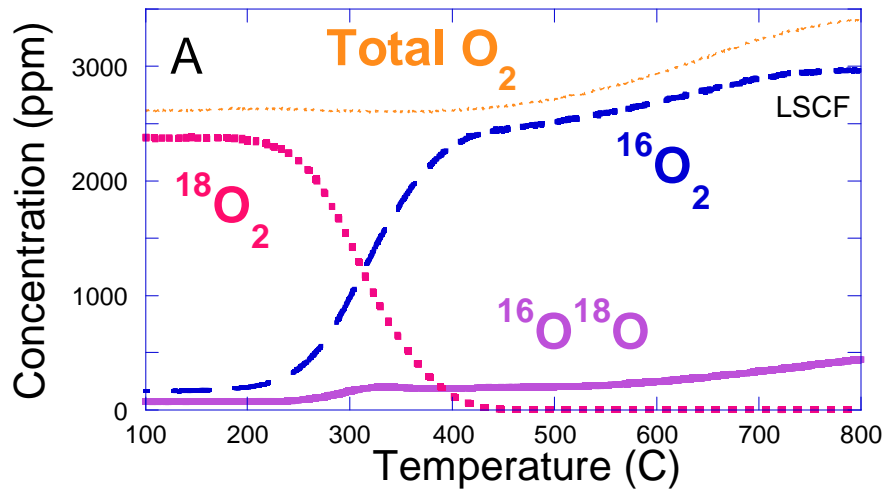


Figure 5-10. Fe 2p_{3/2} profile of LSM + 5wt% Fe and LSCF [74]

5.3.2 Temperature Programmed Isotopic Exchange

The use of ¹⁸O₂ to investigate catalytic activity was discussed previously [71]. Winter [64] and Boreksov [65] were some of the first researchers to use this technique to study oxide reactivity. The basic idea is to differentiate between oxygen from the gas phase and oxygen from the solid lattice. Without using isotopically enriched oxygen, it would not be possible to observe the exchange reaction occurring below the total oxygen curve in the profiles from Figure 5-11. If no reaction occurs, then the signal for each of the oxygen species would remain constant; this is not the case. A decrease in the ¹⁸O₂ line means that species are being taken out of the gas phase and either going into the lattice or recombining with a ¹⁶O at the powder surface to form the mixed product ¹⁶O¹⁸O. The increase in ¹⁶O₂ means that the oxygen originally from the lattice is now being released into the gas phase.



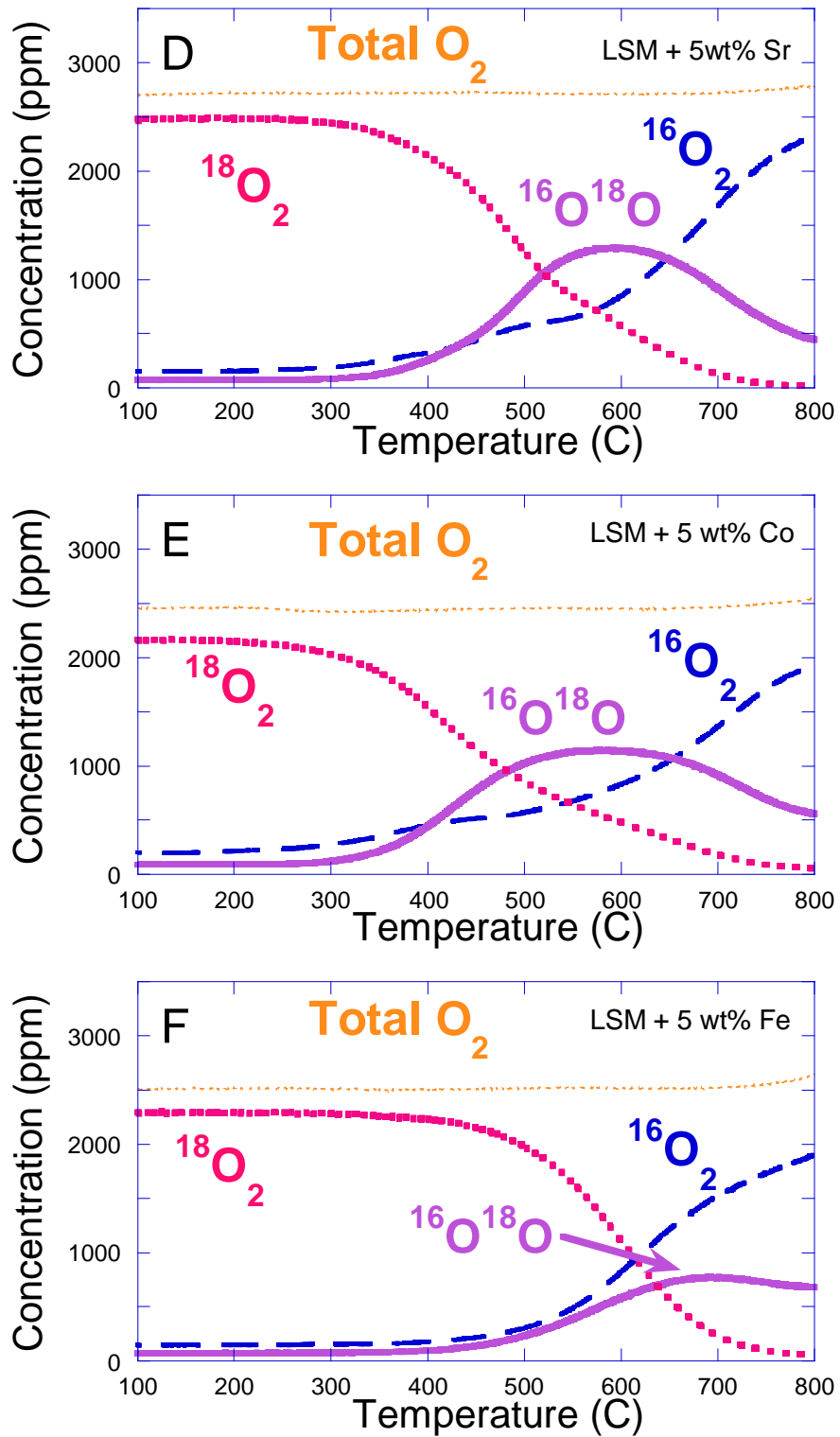
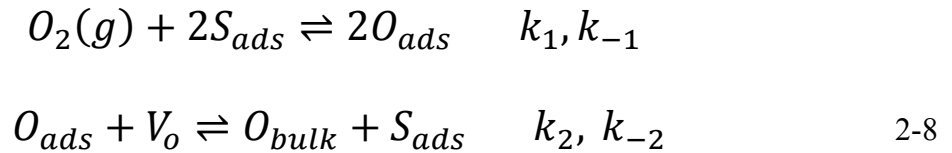


Figure 5-11. Temperature programmed exchange profile for A) LSCF B) LSM C) LSM + 5 wt% La D) LSM + 5 wt% Sr E) LSM + 5 wt% Co F) LSM + 5wt% Fe [74]

According to Boreskov [70], the gas-phase recombination reaction (equation 4-1) is insignificant below 1000°C. Since conditions in this study do not exceed 800°C, the formation of $^{16}\text{O}^{18}\text{O}$ above the baseline is assumed to occur only on the surface with the participation of adsorbed oxygen atoms according to the model. $^{16}\text{O}_2$ above the baseline is primarily due to the oxygen within the lattice going into the gas phase.



As discussed in Chapter 2, the 2 step model (reprinted here as equation 2-8) consists of the dissociative adsorption of a molecule of oxygen on the surface followed by the incorporation of the adsorbed oxygen atom into the solid.



The implication of step 1 is that the different oxygen species will eventually become statistically distributed during reaction according to the isotopic composition of the adsorbed oxygen. This is shown in Figure 5-12 for LSM + 5 wt% Co. The square root of the normalized $^{16}\text{O}_2$ signal (Figure 5-12a) is taken to find the corresponding fraction ($^{16}f_{ads}$) of $^{16}\text{O}_{ads}$ on the surface. Then the distribution of $^{18}\text{O}_2$ and $^{16}\text{O}^{18}\text{O}$ is reconstructed using $(1-^{16}f_{ads})^2$ and $2*(^{16}f_{ads})(1-^{16}f_{ads})$ respectively (Figure 5-12b); the 2 in front of the term $(^{16}f_{ads})(1-^{16}f_{ads})$ arises from the reaction multiplicity. Initially, due to kinetic limitations at low temperature, there is no correlation for $^{18}\text{O}_2$ and $^{18}\text{O}^{16}\text{O}$, but as the surface temperature and the reaction rate increase, the model falls on top of the data showing statistical equilibrium has been obtained for all species.

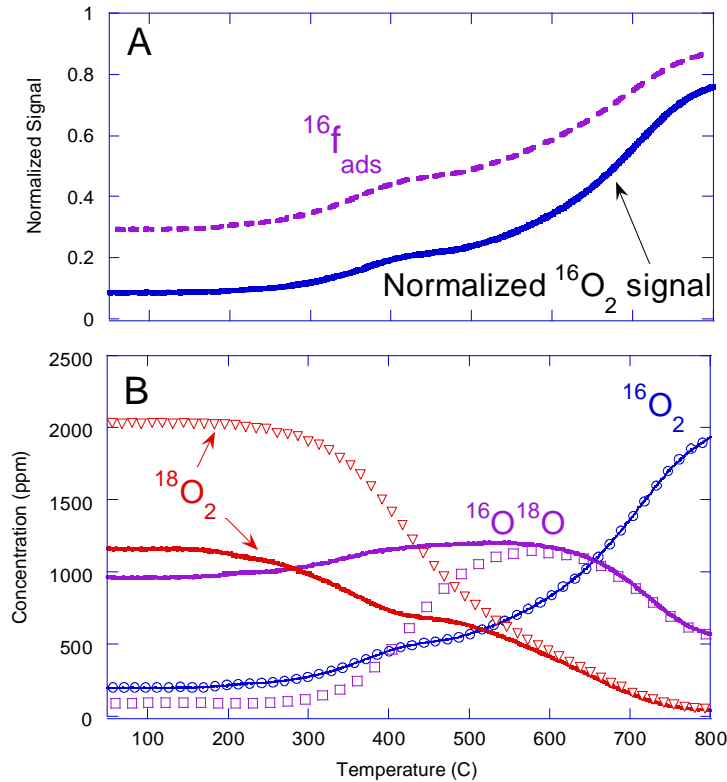


Figure 5-12. Temperature programmed exchange profile of LSM + 5 wt% Co A) $^{16}O_2$ signal normalized and raised to power of 0.5 to yield theoretical $^{16}O_{ads}$ fraction on surface and B) data (points) plotted with statistical equilibrium model (solid lines) [74]

Furthermore, it can be assumed that the sample is the source of ^{16}O throughout the experiment because conversion of the sample oxygen lattice (with changes in oxygen stoichiometry factored in) from ^{16}O to ^{18}O is calculated to be only 10% for LSCF (the most active material) and less for the others. This means that back reaction of the ^{18}O out of the solid is minimal, and it is assumed that the $^{18}O_2$ signal originates from the gas phase and not from saturation of the surface with ^{18}O . If saturation were to occur, then the signal would rise back up with increasing time/temperature, which is not observed.

Another feature present in all profiles from Figure 5-11 is the increase in total oxygen with increasing temperature. This net release of oxygen from the solid indicates the formation of oxygen vacancies, with LSCF showing a much larger non-stoichiometry change than LSM and

LSM based samples. The amount of oxygen released, as shown in Figure 5-13, is the same regardless of the isotopic labeling of the gas phase during the temperature programmed reaction.

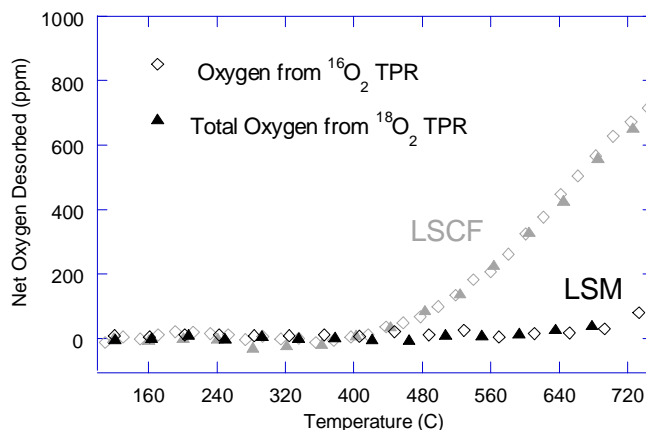


Figure 5-13. Net oxygen desorption from temperature programmed reaction (TPR) profile for LSM and LSCF. Performed in approximately 2,500 ppm O_2 using both normal and isotopically enriched oxygen gas [74]

The exchange profile for LSCF and LSM are shown in Figure 5-11 a-b. It was found that the rate determining step in LSM up to 700-750°C is incorporation (step 2) while the rate determining step in LSCF is dissociative adsorption (step 1) [71]. The onset of exchange occurs at a significantly lower temperature in LSCF (260°C) than in LSM (375°C). Previous studies have also shown that LSCF is more catalytically active toward oxygen than LSM [10,48,71]. LSM not only activates at a higher temperature, it also appears to have a different mechanism from LSCF up until 700°C. Most of the $^{18}\text{O}_2$ in LSCF becomes incorporated into the lattice upon adsorption, with relatively little remaining on the surface and desorbing as $^{16}\text{O}^{18}\text{O}$. However, the $^{16}\text{O}^{18}\text{O}$ peak in LSM is significantly larger, indicating that after an $^{18}\text{O}_2$ dissociates on the surface, there is a tendency for the $^{18}\text{O}_{\text{ads}}$ to recombine and desorb from the surface instead of becoming incorporated into the lattice. This is consistent with the fact that LSM has poor oxygen diffusivity [37,40]. Above 700°C, $^{16}\text{O}^{18}\text{O}$ decreases due to a change in mechanism [71], since the incorporation of ^{18}O into the lattice is no longer as highly activated.

The effects of infiltration in LSM can be seen in Figure 5-11 c-f. Iron infiltration appears to reduce the onset temperature of exchange. Although the cobalt infiltrated sample was an improvement over the base LSM, LSCF is still more catalytically active. Results from Yamahara's study on cobalt infiltrated LSM cathodes also showed improvement over an unmodified cathode [5]. The authors hypothesized that the enhancement was due to surface processes such as increased number of reaction sites and/or increased triple phase boundary length, which lead to a reduction in the charge transfer resistance region of the AC impedance response. However, their work relied on impedance spectroscopy for analysis. This technique gives overall polarization changes between measured electrodes but cannot by itself directly deconvolute whether the observed changes in polarization are due to microstructural or specific reaction rate contributions. In contrast, our approach directly measures the specific reaction rate, independent of cathode microstructure, and changes in catalytic mechanism upon addition/modification of reactive surface sites.

In perovskite materials with the general ABO_3 formula, researchers have found that it is usually the B site that is more strongly associated with the catalytic activity [17,117]. With this idea in mind, it is not surprising that the addition of La or Sr (A site elements) did not produce a large change in the catalytic activity. The addition of B site elements Fe and Co produced a more noticeable change. In their book, Bielański and Harber [72] discuss the correlation between the first row transition metal oxide-oxygen surface bond strength and isotopic exchange activities found by Boreskov [65,118] and Halpern [119]. Co_3O_4 had a higher specific activity for exchange than Fe_2O_3 and a correspondingly lower oxygen-surface bond strength. MnO_2 fell in between Co_3O_4 and Fe_2O_3 in terms of activity and surface bond strength. Previously, XPS work on LSM with a slightly different composition showed it was possible to engineer a LSM thin

film to terminate in a MnO_2 layer [112]. If the LSM in this study was also manganese oxide terminated, it could explain why cobalt infiltration improved LSM surface activity while iron impaired it. One observation that does not appear to fit this theory, at least initially, is that LSCF contains more iron than cobalt on the B site and is the most active. However, the iron 2p peaks (Figure 5-10) from LSCF and LSM + 5 wt% Fe do not match up, indicating that the states of the two surfaces are different. This is evidence that the activity is determined by more than just the surface composition; it is dependent on the specific active site.

The TPX profile for LSCF infiltrated with manganese is shown in Figure 5-14. Adding manganese to the surface of LSCF suppresses the exchange onset temperature from 230 °C to 310 °C, but does not prevent the labeled oxygen from going into the lattice above 310 °C, as evidenced by the relatively small concentration of $^{18}\text{O}_2$ and $^{16}\text{O}^{18}\text{O}$ in the gas stream at high temperatures. This is consistent with the reactivity trends previously mentioned indicating that manganese is not as active as cobalt for surface exchange. It is significant to note that the Mn infiltrated LSCF still performs better than even LSM + 5wt% Co. For LSCF, the dissociative adsorption step is thought to be limiting and therefore the surface modification produced a notable change in the onset temperature while not producing a change in the mechanism. It appears that improving the reactivity of LSCF can be accomplished through cobalt infiltration. Tentative results from a conductivity-relaxation study [120] on cobalt infiltrated bars of LSCF show it is possible to obtain faster surface kinetics with the modified bars over plain bars of LSCF.

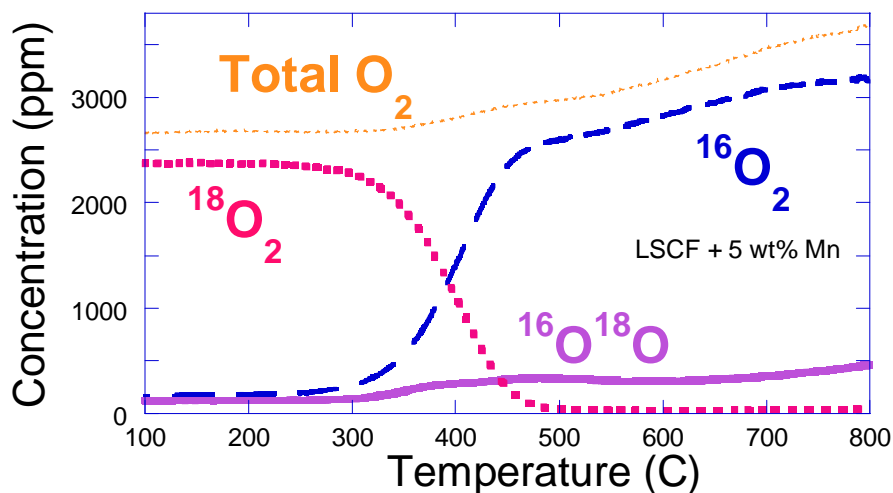


Figure 5-14. Temperature programmed exchange profile for LSCF + 5 wt% Mn [74]

Next, the relationship between activity and the amount of cobalt infiltrated into LSM was examined. 5, 10 and 20 wt% infiltrated LSM samples were tested and compared to each other. Little difference in catalytic activity was found between the powders. All temperature programmed exchange profiles showed exchange onset near 300 °C. It is unclear if this is due to the low oxygen concentration (2,500 ppm) of the TPX testing conditions. Also, the particle size of the Co_3O_4 may be changing such that the coverage remains about the same in each sample.

Since cobalt oxide infiltration improved LSM's catalytic activity for oxygen exchange, we decided to see if pure Co_3O_4 would be even better and the results are shown in Figure 5-15. It is interesting to see a transition region occur between 630-710 °C. The phase transition from Co_3O_4 to CoO at an oxygen partial pressure of 9.9×10^{-10} atm was 350 °C, as observed by Oku [121], and between 800-900 °C in air ($p_{\text{O}_2} = 2 \times 10^{-1}$ atm) [122,123]. Since the conditions for this study were under 2.5×10^{-3} atm O_2 , it is reasonable that the transition could occur at a temperature range somewhere in between, which may explain the equilibrium region in the plot. Above 710 °C, the oxide appears to be releasing a small amount of O_2 , as seen in the rise of the total oxygen line, which is consistent with the decomposition of Co_3O_4 into CoO .

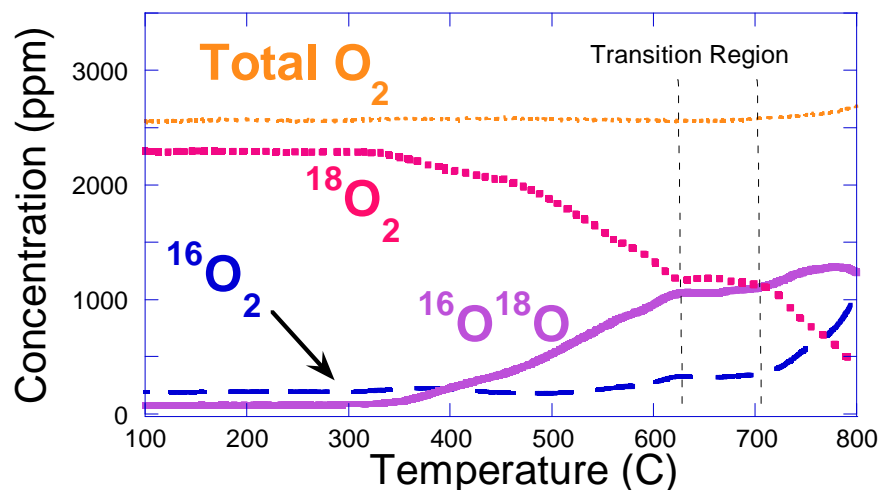


Figure 5-15. Temperature programmed exchange profile for 40 mg Co_3O_4 [74]

Comparing the catalytic activity of Co_3O_4 , LSM and LSM+ 5wt % Co samples to each other, it is apparent that the infiltrated sample is better than the LSM, which in turn is better than Co_3O_4 . LSCF is still best, and we can draw some conclusions as to what properties improve catalytic activity based on the different surfaces of this study. First, we believe LSM is more active than cobalt oxide due to the lack of oxygen vacancies in the cobalt oxide. Both materials do not have many vacancies to begin with, but Co_3O_4 has an excess of oxygen at lower temperatures such that the actual composition should be written as $\text{Co}_3\text{O}_{4+\delta}$ [72]. The material does not become stoichiometric until between 770 and 850 °C in air depending on the preparation method [122]. This point is probably lower in this study because the $p\text{O}_2$ is two orders of magnitude smaller and could occur right before the oxide enters the phase transition region around 600 °C. LSM on the other hand is nearly stoichiometric at 1000 °C under 2.5×10^{-3} atm O_2 [38,92]. The release of oxygen from Co_3O_4 is attributed to the decomposition reaction forming CoO while the oxygen desorption in LSM is attributed to vacancy formation.

Discrepancies in oxygen stoichiometry alone are not enough to explain the difference between the LSM and the cobalt infiltrated LSM. If only oxygen vacancies were responsible for

the activity, then the LSM would perform as well as, if not better than the LSM infiltrated with cobalt. The cobalt infiltration allows oxygen dissociation to occur at lower temperatures, which indicates that the cobalt oxide at the surface may act as an adsorption/active site on the infiltrated surface. Co_3O_4 itself is an important industrial catalyst because of its ability to easily transition between multiple valence states [124]. Cobalt oxide exists as a mixture of Co^{+3} and Co^{+2} states in order to preserve charge neutrality. Although the surface of cobalt oxide may change valence and stoichiometry with reducing/oxidizing conditions, in general, the presence of redox centers on the surface allows it to accept or donate extra electrons. Low oxidation state Co^{2+} functions as an electron donor center through the following reaction: $\text{Co}^{+2} \rightarrow \text{Co}^{+3} + e^-$. If this is the function of the cobalt oxide on LSM, then the dissociative adsorption step could become less activated due to reduced charge transfer resistance, assuming that oxygen dissociation is accompanied by reduction.

To effectively compare the activity for oxygen exchange, the conversion (1- normalized $^{18}\text{O}_2$ signal) versus temperature is displayed for all samples in Figure 5-16. The change in $^{18}\text{O}_2$ signal was used as a measure of reactivity since the other oxygen species are reaction by products. LSCF is more active than all other samples and is followed, in activity, by the LSCF infiltrated with Mn. The reactivity trends for LSM follow a definite pattern where the addition of A site elements La or Sr results in similar behavior and the B site elements follow the trend predicted by earlier isotopic exchange studies. Iron infiltration significantly increased the onset temperature of exchange. Royer et al also observed a connection between iron contamination and lower activities [26]. All other infiltration elements appeared to improve the catalytic activity of LSM, with the addition of cobalt the most beneficial (30% conversion vs. 13% for LSM at

400°C). However, pure Co_3O_4 had approximately the same activity as LSM infiltrated with iron; these two samples had the worst exchange properties of all the samples tested.

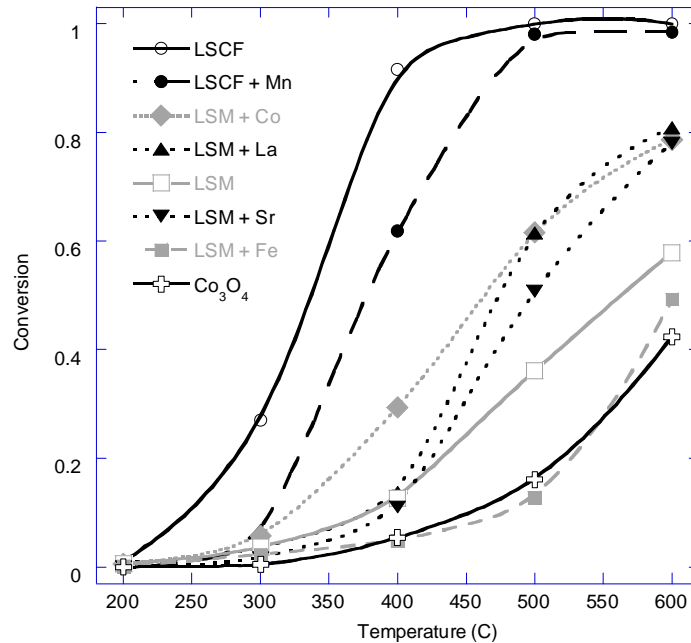


Figure 5-16. Conversion (1-normalized $^{18}\text{O}_2$) vs. temperature, points averaged over 2 runs [74]

All LSM based samples show significant formation of $^{16}\text{O}^{18}\text{O}$ compared to LSCF based samples (Figure 5-17), which is consistent with the incorporation limited mechanism of oxygen exchange in LSM. The addition of Co, Sr and La to LSM improves the surface recombination reaction, which means that the dissociative adsorption step is improved. The simultaneous appearance of $^{18}\text{O}^{16}\text{O}$ as the $^{18}\text{O}_2$ signal decreases suggests that dissociation of the oxygen at the surface (step 1) is more facile in the infiltrated sample, and the limited incorporation step results in desorption of surface scrambled $^{18}\text{O}^{16}\text{O}$ rather than $^{16}\text{O}_2$ from the bulk. Co_3O_4 is more active than LSM + Fe with regard to surface recombination, yet its overall activity as measured by the removal of $^{18}\text{O}_2$ (Figure 5-16) is the same. This is evidence that LSM + Fe is more facile with regard to incorporation than Co_3O_4 since some of the labeled oxygen is becoming incorporated into the bulk.

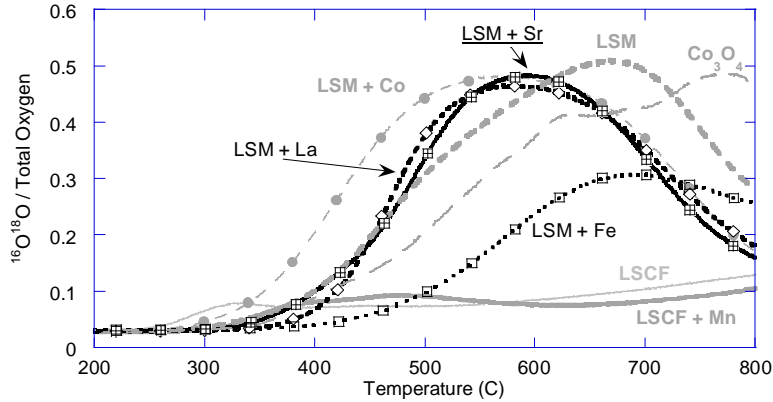


Figure 5-17. Formation of $^{16}\text{O}^{18}\text{O}$ (signal normalized by total oxygen) as a function of temperature [74]

As a final note, one of the more important concerns is the behavior of these cathode materials once integrated into an actual device. For example, LSM is typically mixed with an ionic conductor such as YSZ to produce a composite electrode; the addition of the oxygen ion conducting phase could drastically change the oxygen reduction behavior. Logically, the next application for this technique should be the extension to composite cathodes.

5.4 Conclusion

Temperature programmed isotopic exchange is a fast and simple method for surveying oxygen exchange properties of individual oxide materials. Not only does it identify the active temperature range, this technique can also cast light on the mechanism of oxygen exchange (adsorption or incorporation limited). This study used isotopic exchange to identify trends in reactivity.

Surface modification through infiltration of LSM and LSCF powders altered the material's catalytic activity toward isotopic surface exchange, but did not affect the overall mechanism of surface exchange. Infiltrated LSM powders were still observed to be limited by oxygen incorporation into the lattice just like the base LSM. Although the cobalt infiltrated LSM had

improved exchange properties compared to plain LSM, its overall activity was not as high as LSCF.

The addition of A site elements La and Sr onto the LSM surface did not produce a significant change in isotopic exchange. Cobalt infiltration improved the performance of LSM the most while iron reduced the apparent activity; this can be attributed to the properties of the oxides formed on the LSM surface, which determine how strongly oxygen binds to the surface and subsequently the reactivity. Overall, plain LSCF had the best reactivity. The addition of manganese to the surface of LSCF caused the exchange to occur at a higher temperature, and is in agreement with previously observed reactivity trends where cobalt oxide is more active than manganese oxide which is more active than iron oxide. Two attributes from this study which are associated with catalytic activity are ionic conductivity and active cobalt (or other surface) sites. The extent to which each of these properties affects catalytic activity is unclear and needs to be further studied. The issue of long term stability also needs to be addressed, and perhaps the improvement in the dissociation step achieved with cobalt infiltrated LSM can be translated into a solution with a low degradation rate.

CHAPTER 6 CONCLUSION

The development of high performance solid oxide fuel cells is dependent upon the fundamental understanding of the oxygen reduction process at the cathode surface. Isotopic exchange is a powerful heterogeneous catalysis tool for comparing catalytic activity and mechanism amongst different oxides. Properties, such as oxygen non-stoichiometry, obtained from this method were comparable to results from the literature. During temperature programmed desorption and reaction, the same total oxygen vs. temperature behavior was obtained using oxygen isotope 16 and isotope 18 enriched feed streams.

Temperature programmed oxygen isotopic exchange is a rapid and sensitive method for evaluating catalytic activity and is used to identify trends in catalytic activity. It was demonstrated that LSM is not as active as LSCF and that the mechanism of exchange was different for these materials based upon the relative amounts of each oxygen isotopologues produced. As the temperature increased, the composition of the gas phase would become statistically distributed as predicted by the relative amount of each isotope on the materials surface. This statistical equilibrium between the surface and gas phases is required for further mechanistic analysis of steady state isotopic exchange.

Under testing conditions for isothermal isotopic switching, it was determined that the LSCF surface reaction was occurring so rapidly that the limiting step was influenced by gas phase diffusion. This was not observed in LSM due to its slower reaction rate, which is insensitive to changes in pO_2 . A two step mechanism consisting of dissociative adsorption followed by incorporation of the atomic oxygen into the lattice, was used to model not only the gas phase evolution with time, but also the conversion of the adsorbed oxygen and lattice oxygen from one isotopic labeling to another during the switch. The model predicted greater bulk

oxygen exchange conversion in LSM than back calculated from the profile. This indicates that the LSM could in fact be limited by bulk diffusion and not by the surface reaction as described by the model. In the case of LSCF, inputting a relatively large value for the parameter characteristic of the second step of the model predicted the gas phase isotopologue distribution and bulk conversion very well, indicating that between the two steps of the model, the dissociative adsorption step is rate limiting. Additionally, the curve fitting produced effective rate constants for both LSM and LSCF. The values reported in this dissertation represent one of the first attempts to obtain this information using the two step model. However, the calculated rate constants rely on certain assumed values (i.e. oxygen coverage) and could be improved through actual measurement of those quantities.

A systematic approach to understanding how the surface composition affects catalytic activity was done through depositing various metal oxides onto the surface of LSM and LSCF. The study found that cobalt infiltrated LSM was more active than plain LSM and that iron infiltrated LSM decreased the activity, implying that the active site is the surface B site atom and not oxygen vacancies. Although the composition of LSCF examined contains more iron than cobalt, it was found to be the most active material of the study. XPS indicated that the oxidation state of the iron at the LSCF surface was different from that on the infiltrated LSM surface. This is evidence that the catalytic activity is not just a straightforward function of composition, but the electronic surface properties must also be considered when developing cathode materials. Therefore, the use of surface and electronic sensitive tools, such as a Kelvin Probe, should be the next step in cathode development.

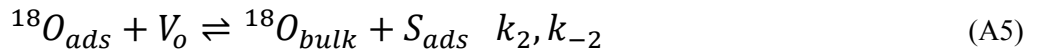
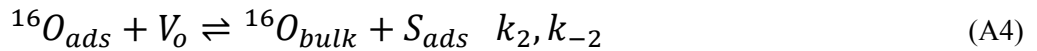
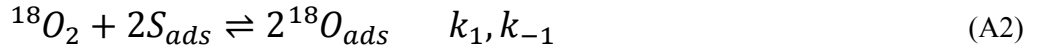
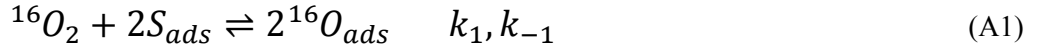
Increasing the cobalt content did not produce further improvements in the catalytic activity. Pure Co_3O_4 , the oxide deposited on the cobalt infiltrated LSM, performed worse than

plain LSM and was about as active as the LSM infiltrated with iron. Infiltrating LSCF with manganese, the B site atom for LSM, was detrimental to the onset temperature of exchange, but it was more active than the LSM infiltrated with cobalt. The apparent mechanism did not change with infiltration for either LSM or LSCF. Given these observations, it is possible that LSCF's activity is based off an optimization of the oxygen non-stoichiometry, cobalt or active redox sites and other unidentified factors.

The ability to test cathode materials independently from the complete SOFC system is a strength and weakness of the isotopic exchange techniques described in this body of work. Great care must be taken when applying the results since the cathode behavior may vary with the electrolyte material and could change under an electrochemical gradient during SOFC operation. Effects from the electrode microstructure, an important feature which affects performance, also cannot be easily examined. One way to bridge this gap is to extend the application of isotopic exchange to composite cathodes, such as LSM/YSZ or LSCF/GDC powders, since the important function of the cathode is to assist with the transfer of oxygen from the gas phase to the electrolyte lattice.

APPENDIX A
DERIVATION OF MODEL

Starting with Equation 2-8, the introduction of a second isotopic label into the system produces five distinct reactions, three for the first step and two for the second.



The intermediate in this 2 step model is the adsorbed oxygen $^{16}O_{ads}$ or $^{18}O_{ads}$; it determines the production of the different isotopic species $^{16}O_2$, $^{18}O_2$, and $^{16}O^{18}O$ in the gas phase as well as the incorporation as bulk oxygen. Therefore, the evolution of the adsorbed oxygen concentration belonging to a particular isotopic labeling is of interest and is derived by balancing the rate of production and consumption. Picking $^{16}O_{ads}$ for the example, it is seen that this species is produced by the forward step of A1 and consumed by the backward step. It is also produced and consumed in equations A3 and A4, respectively. Another assumption is that both steps in equation 2-8 are in equilibrium with respect to the total oxygen in the system, and the forward and backward rates are equal.

$$k_1 P_{O_2} [S]^2 = k_{-1} [O_{ads}]^2 \quad (A6)$$

$$k_2 [V_o] [O_{ads}] = k_{-2} [O_{bulk}] [S] \quad (A7)$$

Equations A6-A7 show that it is possible to write an expression for $^{16}\text{O}_{\text{ads}}$ with either k_1 or k_{-1} , k_2 or k_{-2} . The end result is equation 4-8, which has been normalized. Then the process is repeated for $^{16}\text{O}_{\text{bulk}}$ which yields equation 4-9.

APPENDIX B
PARAMETER FITTING SCRIPT

Main M-File: exchange.m

```

% Extracts parameters A, B and C from fitting differential equations to data
% 1. Use initial guesses for A, B and C, then generate numerical solution with ODE45
% 2. Compare the guessed solution to data and use Gauss Newton method to optimize the fit
% 3. After some iterations, spit out the optimized solution with data, parameters and error
% Cynthia Kan 2009, with Gauss Newton help from Sean Bishop
clear, clc
tic          % Computation time
load LSM.dat;          % Load data and process into lists
oldlist=LSM;
rows=size(oldlist,1);
n=1;
for k=1:2:rows      %% data reduction to reduce computation time
    newlist(n,:)=oldlist(k,:);
    n=n+1;
end

t=newlist(:,1);      % time in minutes          DATA
ydata=newlist(:,2); % y values                  DATA
A=1; B=.1; C=1;     %starting guesses
beta=.015;          % Gas impurity

dA=0.0001; dB=0.0001; dC=0.0001; %guesses for change in A B and C, B can get extremely
large without bound for LSCF
Y0=[1 1];          %initial conditions, 100% oxygen 16 on surface and bulk

for j=1:150; %number of program iterations
    [time,soln] = ode45('rxn',t,Y0,[ ],A,B,C,beta); % calculates the soln to rxn equations, soln is
two column vector, column 1=y1, column2=y2
    ymod=soln(:,1); %takes solution to 16fads and saves as the current model solution
    [time,soln] = ode45('rxn',t,Y0,[ ],A+dA,B,C,beta);
    Z(:,1)=(soln(:,1)-ymod)/dA; %computes derivative of function for each change in A B or C
    [time,soln] = ode45('rxn',t,Y0,[ ],A,B+dB,C,beta);
    Z(:,2)=(soln(:,1)-ymod)/dB;
    [time,soln] = ode45('rxn',t,Y0,[ ],A,B,C+dC,beta);
    Z(:,3)=(soln(:,1)-ymod)/dC;
    ZTZ=(Z'*Z);
    ZTZinv=inv(ZTZ);
    Diff=ydata-ymod;
    ZTD=Z'*Diff;
    d=ZTZinv*ZTD;
    dA=d(1)*.1; %computed change in A B and C
    dB=d(2)*.1;

```

```

dC=d(3)*.1;
A=A+dA; %computed A B and C coefficientnets
B=B+dB;
C=C+dC;
abc(:,j)=[A, B, C]'; j;
dlog(:,j)=d; %data log of A B and C changes to see where program died.
%%% computes the regression  $R^2 = 1-SSerr/SStot$ 
ydataave=mean(ydata); %average y data values
[time,soln] = ode45('rxn',t,Y0,[ ],A,B,C,beta); %Final computation of model values
ymod=soln(:,1); %final y values for modeling (f16ads)
SStotads=sum((ydata-ydataave).^2); % computes the sum of squares
SSerrads=sum((ydata-ymod).^2); % computes the summation (ydata-ymodel)^2
Rsquared(j)=1-SSerrads/SStotads; %R^2 value for fit
end
figure(1)
plot(t,ydata,'o', time,ymod,'--')
figure(2)
plot(1:j,abc(1,:))
toc % End of Computation time
tf=linspace(0,120,2000);
[time,soln] = ode45('rxn',tf,Y0,[ ],A,B,C,beta); %Final computation of model values
ymod=soln(:,1); %final y values for modeling (f16ads)
ymod2=soln(:,2); % final f16bulk
m34=ymod.*(1-ymod)*2;
m32=ymod.^2;
m36=(1-ymod).^2;

%%% DATA OUTPUT %%% mydata has 4 columns, first column is time
mydata(:,1)=time;
mydata(:,2)=m34; mydata(:,3)=m32; mydata(:,4)=m36;
mydata(:,5)=ymod; mydata(:,6)=ymod2;
mydata2(:,1)=[1:j]'; mydata2(:,2)=abc(1,:)' ; mydata2(:,3)=abc(2,:)' ;
save my_data.out mydata -ASCII -tabs
save my_data2.out mydata2 -ASCII -tabs

```

ODE45 Function File: rxn.m

```

function dydt = rxn(t,y,flag,A,B,C,beta)
% solve the system of equations for 16Fads
dydt=zeros(size(y)); Y1=y(1); Y2=y(2);
% RHS expression
dydt(1)=-A*Y1^2-(A+B)*Y1+B*Y2+A*2*beta;
dydt(2)=B*C*(Y1-Y2);
% dydt=[ dydt(1) dydt(2)]

```

LIST OF REFERENCES

- [1] A. D. Pasternak, "Global Energy Futures and Human Development: A Framework for Analysis," Study done in partnership with US Department of Energy and Lawrence Livermore National Laboratory, University of California, 2000
- [2] "World Consumption of Primary Energy by Energy Type and Selected Country Groups, 1980-2004." Energy Information Administration, U.S. Department of Energy, 2006.
- [3] "Worldwide Trends in Energy Use and Efficiency - Key Insights from IEA." International Energy Agency, 2008.
- [4] M. C. Williams, J. P. Strakey, W. A. Surdoval, *J. Power Sources* 143 (2005) 191-196.
- [5] K. Yamahara, C. P. Jacobson, S. J. Visco, X.-F. Zhang, L. C. De Jonghe, *Solid State Ionics* 176 (2005) 275-279.
- [6] E. Ivers-Tiffée, A. Weber, D. Herbstritt, *J. Eur. Ceram. Soc.* 21 (2001) 1805-1811.
- [7] M. Dokiya, *Solid State Ionics* 152-153 (2002) 383-392.
- [8] S. B. Adler, J. A. Lane, B. C. H. Steele, *J. Electrochem. Soc.* 143 (1996) 3554-3564.
- [9] S. B. Adler, X. Y. Chen, J. R. Wilson, *J. Catal.* 245 (2007) 91-109.
- [10] S. P. Jiang, *Solid State Ionics* 146 (2002) 1-22.
- [11] J. W. Erning, T. Hauber, U. Stimming, K. Wippermann, *J. Power Sources* 61 (1996) 205-211.
- [12] L. M. van der Haar, M. W. den Otter, M. Morskate, H. J. M. Bouwmeester, H. Verweij, *J. Electrochem. Soc.* 149 (2002) J41-J46.
- [13] X. Chen, S. Wang, Y. L. Yang, L. Smith, N. J. Wu, B. I. Kim, S. S. Perry, A. J. Jacobson, A. Ignatiev, *Solid State Ionics* 146 (2002) 405-413.
- [14] J. A. Lane, J. A. Kilner, *Solid State Ionics* 136-137 (2000) 997-1001.
- [15] H. J. M. Bouwmeester, M. W. Den Otter, B. A. Boukamp, *J. Solid State Electrochem.* 8 (2004) 599-605.
- [16] R. Ganeshanathan, A. V. Virkar, *J. Electrochem. Soc.* 152 (2005) A1620-A1628.
- [17] Y. Teraoka, H. M. Zhang, N. Yamazoe, *Chem. Lett.* 14 (1985) 1367-1370.
- [18] D. Martin, D. Duprez, *J. Phys. Chem.* 100 (1996) 9429-9438.

- [19] A. Mai, F. Tietz, D. Stöver, *Solid State Ionics* 173 (2004) 35-40.
- [20] R. J. Bell, G. J. Millar, J. Drennan, *Solid State Ionics* 131 (2000) 211-220.
- [21] R. A. De Souza, J. Zehnpfenning, M. Martin, J. Maier, *Solid State Ionics* 176 (2005) 1465-1471.
- [22] S. Carter, A. Selcuk, R. J. Chater, J. Kajda, J. A. Kilner, B. C. H. Steele, *Solid State Ionics* 53-56 (1992) 597-605.
- [23] F. S. Baumann, J. Fleig, H.-U. Habermeier, J. Maier, *Solid State Ionics* 177 (2006) 1071-1081.
- [24] J. R. Wilson, D. T. Schwartz, S. B. Adler, *Electrochim. Acta* 51 (2006) 1389-1402.
- [25] R. A. De Souza, *Phys. Chem. Chem. Phys.* 8 (2006) 890-897.
- [26] S. Royer, D. Duprez, S. Kaliaguine, *J. Catal.* 234 (2005) 364-375.
- [27] K. Klier, J. Novakova, P. Jiru, *J. Catal.* 2 (1963) 479-484.
- [28] R. J. Gorte, J. M. Vohs, *J. Catal.* 216 (2003) 477-486.
- [29] S. B. Adler, *Chem. Rev.* 104 (2004) 4791-4844.
- [30] F. S. Baumann, 2006. Oxygen reduction kinetics on mixed conducting SOFC model cathodes, Ph.D. thesis, University of Stuttgart, Germany
- [31] A. C. Co, V. I. Birss, *The Journal of Physical Chemistry B* 110 (2006) 11299-11309.
- [32] S. P. Jiang, *J. Power Sources* 124 (2003) 390-402.
- [33] D. W. Oxtoby, H. P. Gillis, N. H. Nachtrieb, "Principles of Modern Chemistry," 4th ed. Saunders College Publishing. (1999).
- [34] A. Weber, E. Ivers-Tiffée, *J. Power Sources* 127 (2004) 273-283.
- [35] S. C. Singhal, *Solid State Ionics* 135 (2000) 305-313.
- [36] J. A. Lane, S. J. Benson, D. Waller, J. A. Kilner, *Solid State Ionics* 121 (1999) 201-208.
- [37] I. Yasuda, K. Ogasawara, M. Hishinuma, T. Kawada, M. Dokiya, *Solid State Ionics* 86-88 (1996) 1197-1201.
- [38] J. H. Kuo, H. U. Anderson, D. M. Sparlin, *J. Solid State Chem.* 83 (1989) 52-60.

- [39] L. W. Tai, M. M. Nasrallah, H. U. Anderson, D. M. Sparlin, S. R. Sehlin, *Solid State Ionics* 76 (1995) 273-283.
- [40] R. A. De Souza, J. A. Kilner, J. F. Walker, *Mater. Lett.* 43 (2000) 43-52.
- [41] J. H. Kuo, H. U. Anderson, D. M. Sparlin, *J. Solid State Chem.* 87 (1990) 55-63.
- [42] K. Katayama, T. Ishihara, H. Ohta, T. S-J, Y. Esaki, E. Inukai, *J. Ceram. Soc. Jpn.* 97 (1989) 1327-1333.
- [43] R. M. Ormerod, *Chem. Soc. Rev.* 32 (2003) 17-28.
- [44] R. A. De Souza, J. A. Kilner, *Solid State Ionics* 106 (1998) 175-187.
- [45] S. Wang, T. Kato, S. Nagata, T. Honda, T. Kaneko, N. Iwashita, M. Dokiya, *Solid State Ionics* 146 (2002) 203-210.
- [46] A. Esquirol, N. P. Brandon, J. A. Kilner, M. Mogensen, *J. Electrochem. Soc.* 151 (2004) A1847-A1855.
- [47] J. W. Stevenson, T. R. Armstrong, R. D. Carneim, L. R. Pederson, W. J. Weber, *J. Electrochem. Soc.* 143 (1996) 2722-2729.
- [48] E. Perry Murray, M. J. Sever, S. A. Barnett, *Solid State Ionics* 148 (2002) 27-34.
- [49] F. M. Figueiredo, J. A. Labrincha, J. R. Frade, F. M. B. Marques, *Solid State Ionics* 101-103 (1997) 343-349.
- [50] A. Petric, P. Huang, F. Tietz, *Solid State Ionics* 135 (2000) 719-725.
- [51] W. Zajac, K. Swierczek, J. Molenda, *J. Power Sources* 173 (2007) 675-680.
- [52] H. Inaba, H. Tagawa, *Solid State Ionics* 83 (1996) 1-16.
- [53] D. Mantzavinos, A. Hartley, I. S. Metcalfe, M. Sahibzada, *Solid State Ionics* 134 (2000) 103-109.
- [54] A. Hartley, M. Sahibzada, M. Weston, I. S. Metcalfe, D. Mantzavinos, *Catal. Today* 55 (2000) 197-204.
- [55] J. A. Kilner, R. A. De Souza, I. C. Fullarton, *Solid State Ionics* 86-88 (1996) 703-709.
- [56] A. Esquirol, J. Kilner, N. Brandon, *Solid State Ionics* 175 (2004) 63-67.
- [57] J. E. t. Elshof, M. H. R. Lankhorst, H. J. M. Bouwmeester, *J. Electrochem. Soc.* 144 (1997) 1060-1067.

- [58] J. Maier, *Solid State Ionics* 112 (1998) 197-228.
- [59] T. Ishihara, J. A. Kilner, M. Honda, N. Sakai, H. Yokokawa, Y. Takita, *Solid State Ionics* 113-115 (1998) 593-600.
- [60] R. E. van Doorn, I. C. Fullarton, R. A. de Souza, J. A. Kilner, H. J. M. Bouwmeester, A. J. Burggraaf, *Solid State Ionics* 96 (1997) 1-7.
- [61] S. Fearn, J. Rossiny, J. Kilner, *Solid State Ionics* 179 (2008) 811-815.
- [62] B. C. H. Steele, *Solid State Ionics* 75 (1995) 157-165.
- [63] N. Morita, T. Titani, *Bull. Chem. Soc. Jpn.* 13 (1938) 601-607.
- [64] E. Winter, *Adv. in Catal.* 10 (1958) 196.
- [65] G. Borekov, *Adv. in Catal.* 15 (1964) 285.
- [66] V. S. Muzykantov, G. I. Panov, *Kinet. Katal.* 13 (1972) 350-357.
- [67] E. R. S. Winter, *Journal of the Chemical Society (Resumed)* 1950 (1950) 1170-1175.
- [68] B. A. Boukamp, H. J. M. Bouwmeester, A. J. Burggraaf, *Proceedings of the Second Int. Symp. on Ionic and Mixed Conducting Ceramics San Francisco, CA, 1994*, pp. 141
- [69] S. L. Shannon, J. G. Goodwin, *Chem. Rev.* 95 (1995) 677-695.
- [70] G. Borekov, "Heterogeneous Catalysis." Hauppauge, New York Nova Science Publishers, Inc. (2003).
- [71] C. C. Kan, H. H. Kan, F. M. Van Assche IV, E. N. Armstrong, E. D. Wachsman, *J. Electrochem. Soc.* 155 (2008) B985-B993.
- [72] A. Bielański, J. Haber, "Oxygen in Catalysis." New York, New York Marcel Dekker, Inc. (1991).
- [73] N. Yamazoe, Y. Teraoka, T. Seiyama, *Chem. Lett.* 10 (1981) 1767.
- [74] C. Kan, E. D. Wachsman, *J. Electrochem. Soc.* Submitted (2009).
- [75] B. A. Boukamp, H. J. M. Bouwmeester, H. Verweij, A. J. Burggraaf, *Mater. Res. Soc. Symp. Proc.* 293 (1993) 361-366.
- [76] Y. Teraoka, M. Yoshimatsu, N. Yamazoe, T. Seiyama, *Chem. Lett.* 13 (1984) 893-896.

- [77] D. Efremov, L. Pinaeva, V. Sadykov, C. Mirodatos, *Solid State Ionics* 179 (2008) 847-850.
- [78] S. Ootoshi, H. Sasaki, H. Ohnishi, M. Hase, K. Ishimaru, M. Ippommatsu, T. Higuchi, M. Miyayama, H. Yanagida, *J. Electrochem. Soc.* 138 (1991) 1519-1523.
- [79] R. A. De Souza, J. A. Kilner, *Solid State Ionics* 126 (1999) 153-161.
- [80] B. C. H. Steele, J.-M. Bae, *Solid State Ionics* 106 (1998) 255-261.
- [81] S. J. Benson, R. J. Chater, J. A. Kilner, *Proceedings of the Third International Symposium on Ionic and Mixed Conducting Ceramics, 1997*, pp. 596
- [82] S. J. Benson, 1999. Ph.D. thesis, Imperial College, London
- [83] S. Wang, P. A. W. van der Heide, C. Chavez, A. J. Jacobson, S. B. Adler, *Solid State Ionics* 156 (2003) 201-208.
- [84] B. T. Dalslet, M. Soegaard, P. V. Hendriksen, *J. Electrochem. Soc.* 154 (2007) B1276-B1287.
- [85] H. S. Fogler, S. H. Fogler, "Elements of chemical reaction engineering," Prentice-Hall Englewood Cliffs, NJ. (1992).
- [86] S. R. Bishop, E. D. Wachsman, Unpublished (2009).
- [87] A. Endo, H. Fukunaga, C. Wen, K. Yamada, *Solid State Ionics* 135 (2000) 353-358.
- [88] J. P. Joly, D. Klavana, J. Kirchnerova, *React. Kinet. Catal. Lett.* 68 (1999) 249-255.
- [89] D. Gostovic, J. R. Smith, D. P. Kundinger, K. S. Jones, E. D. Wachsman, *Electrochem. Solid-State Lett.* 10 (2007) B214-B217.
- [90] N. Q. Minh, *J. Am. Ceram. Soc.* 76 (1993) 563-588.
- [91] J. A. M. van Roosmalen, P. van Vlaanderen, E. H. P. Cordfunke, W. L. Ijdo, D. J. W. Ijdo, *J. Solid State Chem.* 114 (1995) 516-523.
- [92] F. W. Poulsen, *Solid State Ionics* 129 (2000) 145-162.
- [93] V. A. Cherepanov, L. Y. Barkhatova, V. I. Voronin, *J. Solid State Chem.* 134 (1997) 38-44.
- [94] L. W. Tai, M. M. Nasrallah, H. U. Anderson, D. M. Sparlin, S. R. Sehlin, *Solid State Ionics* 76 (1995) 259-271.

- [95] A. Mai, V. A. C. Haanappel, S. Uhlenbruck, F. Tietz, D. Stover, *Solid State Ionics* 176 (2005) 1341-1350.
- [96] F. Tietz, V. A. C. Haanappel, A. Mai, J. Mertens, D. Stover, *J. Power Sources* 156 (2006) 20-22.
- [97] H. Uchida, M. Yoshida, M. Watanabe, *J. Electrochem. Soc.* 146 (1999) 1-7.
- [98] V. A. C. Haanappel, D. Rutenbeck, A. Mai, S. Uhlenbruck, D. Sebold, H. Wesemeyer, B. Röwekamp, C. Tropartz, F. Tietz, *J. Power Sources* 130 (2004) 119-128.
- [99] N. Caillol, M. Pijolat, E. Siebert, *Appl. Surf. Sci.* 253 (2007) 4641-4648.
- [100] A. N. Grundy, B. Hallstedt, L. J. Gauckler, *J. Phase Equilib. Diffus.* 25 (2004) 311-319.
- [101] K. Tezuka, M. Inamura, Y. Hinatsu, Y. Shimojo, Y. Morii, *J. Solid State Chem.* 145 (1999) 705-710.
- [102] A.-E. Gobichon, J.-P. Auffredic, D. Louer, *Solid State Ionics* 93 (1996) 51-64.
- [103] G. Ketteler, Weiss, W., Ranke, W., Schlögl, R., *Phys. Chem. Chem. Phys* 3 (2001) 1114 - 1122.
- [104] J. T. Kloprogge, L. V. Duong, B. J. Wood, R. L. Frost, *J. Colloid Interface Sci.* 296 (2006) 572-576.
- [105] P. A. W. v. d. Heide, *Surf. Interface Anal.* 33 (2002) 414-425.
- [106] N. A. Merino, B. P. Barbero, P. Eloy, L. E. Cadus, *Appl. Surf. Sci.* 253 (2006) 1489-1493.
- [107] T. L. Barr, "Modern ESCA: The principles and practice of X-ray photoelectron spectroscopy," CRC press. (1994).
- [108] D. A. Pawlak, M. Ito, M. Oku, K. Shimamura, T. Fukuda, *J. Phys. Chem. B* 106 (2002) 504-507.
- [109] Q.-H. Wu, M. Liu, W. Jaegermann, *Mater. Lett.* 59 (2005) 1980-1983.
- [110] W. M. R. C.D.Wagner, L.E.Davis, J.F.Moulder, and G.E.Mullenberg, "Handbook of X-ray Photoelectron Spectroscopy." Eden Prairie, MN, USA Perkin-Elmer Corp. (1979).
- [111] Y. Uwamino, T. Ishizuka, H. Yamatera, *J. Electron. Spectrosc. Relat. Phenom.* 34 (1984) 67-78.

- [112] H. Kumigashira, K. Horiba, H. Ohguchi, K. Ono, M. Oshima, N. Nakagawa, M. Lippmaa, M. Kawasaki, H. Koinuma, *Appl. Phys. Lett.* 82 (2003) 3430-3432.
- [113] H. Van Doveren, J. A. T. H. Verhoeven, *J. Electron. Spectrosc. Relat. Phenom.* 21 (1980) 265-273.
- [114] S. C. Petitto, E. M. Marsh, G. A. Carson, M. A. Langell, *J. Mol. Catal. A: Chem.* 281 (2008) 49-58.
- [115] T. Fujii, F. M. F. de Groot, G. A. Sawatzky, F. C. Voogt, T. Hibma, K. Okada, *Phys. Rev. B: Condens. Matter Mater. Phys.* 59 (1999) 3195.
- [116] C. R. Brundle, T. J. Chuang, K. Wandelt, *Surf. Sci.* 68 (1977) 459-468.
- [117] T. Seiyama, *Cat. Rev. - Sci. Eng.* 34 (1992) 281.
- [118] G. K. Boreskov, V. V. Popvskii, V. A. Sazonov, *Proceedings of the Fourth International Congress on Catalysis 1* (1968).
- [119] B. Halpern, J. Germain, *J. Catal.* 37 (1975) 44-56.
- [120] D. J. Oh, "Conductivity relaxation of La_{0.6}Sr_{0.4}Co_{0.2}Fe_{0.8}O_{3-d}." 2008.
- [121] M. Oku, Y. Sato, *Appl. Surf. Sci.* 55 (1992) 37-41.
- [122] R. Garavaglia, C. M. Mari, S. Trasatti, C. de Asmundis, *Surf. Technol.* 19 (1983) 197-215.
- [123] K. Koumoto, H. Yanagida, *Jpn. J. Appl. Phys.* 20 (1981) 445-446.
- [124] N. Bahlawane, E. Fischer Rivera, K. Kohse-Höinghaus, A. Brechling, U. Kleineberg, *Applied Catalysis B, Environmental* 53 (2004) 245-255.

BIOGRAPHICAL SKETCH

Cynthia Kan was born in Philadelphia, the same year that her father received his PhD from the University of Pennsylvania. The family moved to Jacksonville Florida a year later and then relocated to the San Francisco Bay Area when she was in the third grade. She graduated from Mission San Jose High School and went on to attend the University of California. There, she met her husband and accompanied him to the University of Florida for graduate school. She graduated with a master's degree and went on to attain a PhD.

During her time at UF, she served as a graduate senator in Student Government and was promoted to Chair of the Senate ad hoc Sustainability Committee. She has written numerous bills and resolutions, the most significant being the allocation of reserves toward an energy efficient lighting project which would save up to \$44,000 a year on energy costs. Working with the committee and the Student Government Environmental Affairs Secretary, she ended the term by consolidating the ad hoc sustainability committee and secretary positions into a permanent agency, enabling Student Government's commitment to sustainability on campus.

Cynthia's experiences serving the student body has translated in a desire to pursue a career in public service. She hopes to work on clean energy and become an influential policy maker.